

REVIEWS OF TOPICAL PROBLEMS

PACS numbers: 95.55.Vj, 98.70.Sa

Radio emission from extensive air showers

A D Filonenko

DOI: 10.3367/UFNe.0185.201507a.0673

Contents

__Abstract.__ **We review research on the currently topical high-energy physics problem of using the radio emission from extensive air showers to detect ultra-high-energy cosmic particles. We present experimental results on the shower radio emission and consider laboratory experiments on modeling radio emission from electron beams and high-energy gamma quanta. Also reviewed are current views on radio emission mechanisms from showers caused by high-energy particles in the meter and centimeter wavelength ranges. The use of the radar method to study air showers is discussed. The theoretical concepts of the emission of coherent and noncoherent radiation in the superhigh frequency range are briefly reviewed, and the possibility of reconstructing shower parameters from radio emission data is considered.**

Keywords: extensive air shower, radio emission, radio detection, particle

1. Introduction

Presently, the most reliable information about ultra-high-energy cosmic particles is obtained from studies of air showers initiated by these particles in Earth's atmosphere, which is constantly bombarded by high-energy charged particles coming from the interstellar medium, so-called cosmic rays (CRs). The term 'ray' or 'radiation' here does not mean that CRs have a purely electromagnetic nature (like solar radiation, radio waves, or X-ray emission). This term was introduced immediately after the phenomenon was discovered, but its nature was unknown. Although it soon became clear that CRs mainly consist of protons accelerated in space, the term has been preserved. Studies of the new phenomenon have immediately given results at the forefront of science.

Measurements in the ultra-high-energy range $W > 10^{20}$ eV are very unreliable due to a very low flux of particles with such energies, which is roughly one event every 100 years per km^2. To detect such rare events, a network of detectors (ground-based Cherenkov and fluorescent) has to be constructed in an area of several hundred and even a thousand square kilometers. Sites for such big complex detectors are chosen in regions with low economic activity but capable of sustaining the performance of a huge number of detectors. Such detectors were first installed on areas of several dozen square kilometers (Yakutsk, Havera Park, Akeno), then spanned an area of several hundred square kilometers [AGASA (Akeno Giant Shower Array), Fly's Eye, HiRes (High Resolution Fly's Eye cosmic ray detector)], and, finally, modern installations placed in an area of several thousand square kilometers were constructed (Pierre Auger Observatory in Argentina, Telescope Array in Utah, USA).

Further studies of ultra-high-energy cosmic rays (UHECRs) with energies above 10^{20} eV are possible only with detectors with an effective area at least two orders of magnitude as high as that of the Pierre Auger Observatory.

A D Filonenko Volodymyr Dahl East Ukrainian National University, prosp. Radýanskii 59a, 93400 Severodonetsk, Luhansk region, Ukraine
E-mail: uy5lo@mail.ru

Received 10 July 2014, revised 15 April 2015
Uspekhi Fizicheskikh Nauk **185** (7) 673 – 716 (2015)
DOI: 10.3367/UFNr.0185.201507a.0673
Translated by K A Postnov; edited by A M Semikhatov

This means that the detectors must be located over an area of $\approx 10^5$ km^2. Clearly, the traditional installations, i.e., ground-based detectors and Fly's Eye detectors used at the Pierre Auger Observatory, can hardly be constructed on such huge areas in the nearest future, and for CRs with higher energies, they are virtually unrealizable. This stimulates the search for new methods of UHECR detection. Among nontraditional methods (i.e., those that do not use Geiger counters, ionization calorimeters, fluorescent detectors, etc.), the so-called radio method seems to be the most promising. The method is based on determining the primary particle characteristics from measurements of the radio pulse generated by a cascade shower in a dense or rarefied medium.

This idea was first proposed in the early 1960s by Askar'yan [1, 2], who showed that an extensive air shower (EAS) contains an excess of negative charges and should coherently radiate in Earth's atmosphere. In theoretical paper [3], another mechanism tied to the geomagnetic field was considered. It was concluded that the geomagnetic mechanism should be much more effective than the Cherenkov mechanism. Experimental paper [4] supported the conclusion in [3] about the dominance of electron emission in Earth's magnetic field.

Subsequently (until the 1980–1990s), several hundred papers were published and several dozen international conferences were organized devoted to the radiation mechanisms of air showers and the possibility of using the radio emission from EASs to detect primary cosmic particles. These studies are reviewed in detail in [5, 6]. Generally, this stage of research did not lead to the expected results. The amplitude of the radio signal turned out to be too small to be detected against the radio interferences.

However, the radiophysical method of CR studies seemed to be so effective that already at the end of that period, the idea of implementing the radio astronomical method, mentioned already in the original papers [1, 2], became popular. This method uses the Moon as a target for UHECRs. It seemed that the cascade developed in the lunar regolith should be accompanied by high-frequency radio emission, which could be detected by ground-based radio telescopes. The Moon as a target for UHECRs is attractive not only due to its high visible surface area. Its upper surface layer, the lunar regolith, does not contain water vapor and therefore does not (according to some sources) significantly absorb radio waves with frequencies up to the gigahertz range, even at a depth of $\sim 10-20$ m.

More detailed theoretical studies were conducted in [7], and the first experiment was carried out at the Australian Parkes Radio Observatory with a 64 m radio dish [8]. However, neither this experiment nor the subsequent observations have given compelling evidence that the registered signal was of lunar origin. The analysis showed that there are several reasons for the negative results. To use the Moon as a target for UHECRs, another approach is required. This stage of research was reviewed in [9].

In Section 2, we discuss in detail the technical characteristics of several modern air shower detectors, as well as the criteria of the event selection and data processing. A detailed discussion of the experimental method not only is interesting from the practical standpoint but also is needed to show the progress over the last 10–15 years in the understanding of the nature of air shower radio emission and its radio detection. In Sections 3 and 4, we present and briefly discuss theoretical concepts of the radio emission from air showers.

2. Experimental research

2.1 Study of a radio detector prototype in the CASA/MIA experiment

As mentioned in Section 1, in the 1990s the construction was started of the Pierre Auger superdetector, with an effective area of 3×10^3 km^2, which included both ground-based and fluorescent detectors. The combination of different detection methods enables the correct reconstruction of the shower geometry when a CR event is detected simultaneously by one ground-based and one fluorescent detector at least. According to some authors, additional radio detections at the Pierre Auger observatory could provide more reliable reconstruction of the shower geometrical parameters. In addition, the fluorescent detectors can operate only during moonless and cloudless nights, which occur only 10% of the total time. A radio detector has none of these shortcomings and could be an effective addition to the existing detectors. For this, as early as the mid-1990s, preparatory work was started to perform joint observations at the Pierre Auger Observatory.

Before the construction of the radio detector at the Pierre Auger Observatory, it was necessary to carry out preliminary studies and model tests. A radio detector prototype in the CASA/MIA [Chicago Air Shower Array (CASA) and Michigan Muon Array (MIA)] experiment in Dugway, Utah, USA (100 km southwest of Salt Lake City, which is near the northern part of the Pierre Auger Observatory) was discussed in [10, 11]. It was proposed there to check experimental results obtained in the 1960s–1970s in the frequency range of 50–100 MHz. The authors rightfully note insufficiently reliable reproduction of the results obtained in some papers in those years. In addition, a careful monitoring of radio interference caused by local electronic equipment in the radio dishes had to be performed.

The CASA experiment, designed to detect CR air showers, was a square network of 33×33 stations spaced 15 m apart and located in an unpopulated area. Each station was equipped with four plastic scintillators 61 cm$\times$61 cm$\times$1.27 cm in size optically connected to photomultipliers. When a signal appeared in three or four photomultipliers, the station sent a 5 μs pulse to the operation center that triggered checking whether other stations had detected this event.

The University of Michigan designed and constructed a muon detector array (MIA) operated jointly with CASA. The MIA consisted of 16 parts, each containing 64 muon counters placed 3 m under the ground in different sites of the CASA experimental area. Each counter was 1.9 m $\times$ 1.3 m in size. Four of these sites were located within 45 m from the center of the CASA array, the next four were located 110 m from the center, and the last eight were placed at the corners of a rectangle with coordinates $x = \pm 180$ m and $y = \pm 185$ m in the eastern and northern directions.

To monitor radio noises outside the particle detector, a broadband logoperiodic dish operating in the frequency range 26–170 MHz was installed 30 m away from the CASA detector at a height of 10 m. The dish monitored 5000 detector runs with different regimes of filtering and amplification of the signal and noise suppression. Preliminary results obtained in September–December 1996 showed that approximately one of 10 detector runs was accompanied by a radio pulse from air showers.

To correctly understand the triggering rate of the detector by a cosmic particle, the following points should be made.

The threshold energy of the CASA detector is several hundred TeV, which corresponds to a count rate of 10–20 Hz (i.e., 10–20 events per second). The expected event rate from showers with energies of 10^{15}, 10^{16}, 10^{17}, and 10^{18} eV are respectively 1 per s, 1 every 2 min, 1 every 4 hr, and 2 per month. These rates correspond to a total area of the array of 0.25 km^2 for the presumed CR spectrum at these energies. If the energy of a vertical shower is about 10^{17} eV and its axis lies within 100 m of the antenna, the expected radio signal would be above the galactic noise level (1–2 μV m^{-1} MHz^{-1}) [12]. Because a shower with such energy is expected to occur once every several hours and its axis can be more than 100 m away from the dish, registration of a spurious radio noise pulse during that long period of time is very probable, which significantly decreases the detector efficiency.

2.2 LOPES radio detector

The LOPES (LOFAR PrototypE Station) is the prototype of the LOFAR (LOw Frequency ARray) radio telescope currently under construction in the Netherlands and designed for radio astronomical observations. The LOFAR project is a new attempt to revitalize astronomical research in the 10–200 MHz range using modern informational technologies. The main idea of LOFAR is to construct a big detector consisting of 100 stations with wide-beam dipole antennas. Signals from the antennas are to be digitized and transferred to a central supercomputer. Besides their main purpose, the antennas can be used as a radio telescope to detect air showers in a wide energy range ($2 \times 10^{14} - 10^{20}$ eV).

Initially, the LOFAR included 10 dipole inverted vee antennas called LOPES-10. Subsequently, the number of dishes increased to 30 (LOPES-30). Each dish is mounted as a module on a metal screen, which also influences the formation of antenna's beam.

The detector module includes three main units. The first block is an amplifier with negative feedback that provides a uniform amplification in the entire frequency range 40–80 MHz. The signal from the amplifier is directed to a bandpass filter with attenuation outside the frequency band 43–76 MHz by 60 dB. The filter is aimed at suppressing low-frequency components in a discrete signal spectrum at frequencies below the Nyquist frequency. In the second block, an analog signal is transformed into a digital one. In the third block, the electric signals are converted into optical ones and directed via an optical fiber line into the memory block of the central station. For the self-consistent addition of signals from each dish, the central station is equipped with a time counter that provides time signals for the analog-to-digital converter and memory block.

The antenna modules are placed near the KASCADE (KArlsruhe Shower Core and Array DEtector) [13], which in turn is a part of a larger array, KASCADE-Grande [14], of the Karlsruhe Research Center (Germany). KASCADE and KASCADE-Grande are multi-detector arrays that are able to measure high-energy air showers in the energy range from 10^{14} to 10^{18} eV [15]. These data are used to provide the energy calibration of air showers.

The aim of the LOPES project is to detect air showers with very large zenith angles ($> 70°$) using the antenna array and modern computer technologies. When a cosmic particle with ultra-high energy ($> 10^{19}$ eV) passes close to the vertical direction, the shower maximum occurs at a height of several hundred meters above Earth's surface or even under the ground, and then most of the radio emission from the cascade is virtually undetectable. This is due to the incoherence of detection. It is well known that the refractive index of the normal atmosphere is about 1.0003, and consequently the Cherenkov emission cone is directed almost along the shower axis. Therefore, even if the observer is located close to the shower axis, the coherence condition is satisfied only for a small part of the shower. This problem is absent for highly tilted showers, but in that case the distance to the shower maximum becomes about ten kilometers or more. Among other tasks, the LOPES project should clarify whether a radio detector can be used to analyze the shower from such energetic particles.

KASCADE-Grande, of course, registered all showers available, but only showers with a large tilt were analyzed. The data analysis allowed determining the shower inclination to an accuracy of about 1°. In addition, the number of electrons and muons in the shower at the ground level and the total cascade energy were determined.

For seven months in 2004, KASCADE was triggered 2017 times by particles with zenith angles $> 50°$ and the primary particle energy $10^{16} - 10^{17}$ eV [16]; 1931 events were due to particles with zenith angles in the range $50° - 70°$, and only one event in 35 was accompanied by a radio pulse. Upon increasing the zenith angle, the number of triggers decreased. Only 85 showers had zenith angles higher than 70°; only four of them were associated with radio signals on the LOPES-10 detector.

This detection rate is significantly higher than the mean value for LOPES-10. On average, for every 1000 triggers of KASCADE, approximately one event was associated with a radio signal from the array. The reason for such a distribution of the detection efficiency is that there were no low-energy showers among all tilted showers detected by KASCADE, because a tilted path is much longer than the vertical one. Consequently, the radio power from tilted showers is also higher than that from vertical ones. Moreover, even if a vertical shower has a higher energy, for the reason pointed out above (the violation of the detection coherence), the detected radio power would be low. It is also necessary to take into account that the radio pulse from a distant shower covers a higher ground surface area.

To decrease the energy threshold of showers triggering KASCADE, only showers with a high muon density were selected. This condition reduced the sample to 51 events detected by LOPES-10 in March 2004, with a zenith angle of 53° and an azimuthal angle of 54° (the zero azimuth corresponds to the north) and a nearly equal number, 1.5×10^6, of electrons and muons. This corresponds to a primary particle energy of 10^{17} eV.

Figure 1a shows the electric field strength near each of the LOPES-10 dishes corrected for geometrical and instrumental delays relative to the shower axis. The field is coherent near the time instant 1.825 μs determined by the time delay of the shower arrival. The incoherent noise is due to radio emission from the photomultipliers. In this event, this background is comparatively low due to the small number of electrons reaching the ground (this determines the current in the photomultiplier).

Figure 1b shows the electric field strength of the radio pulse as a function of time after power-beam processing (the thin line) and cross-correlation (cc) processing (the thick line). For a given shower direction, the power-beam processing improves the time delay of the signal at each dish and the corresponding antenna amplification coefficient. The signal

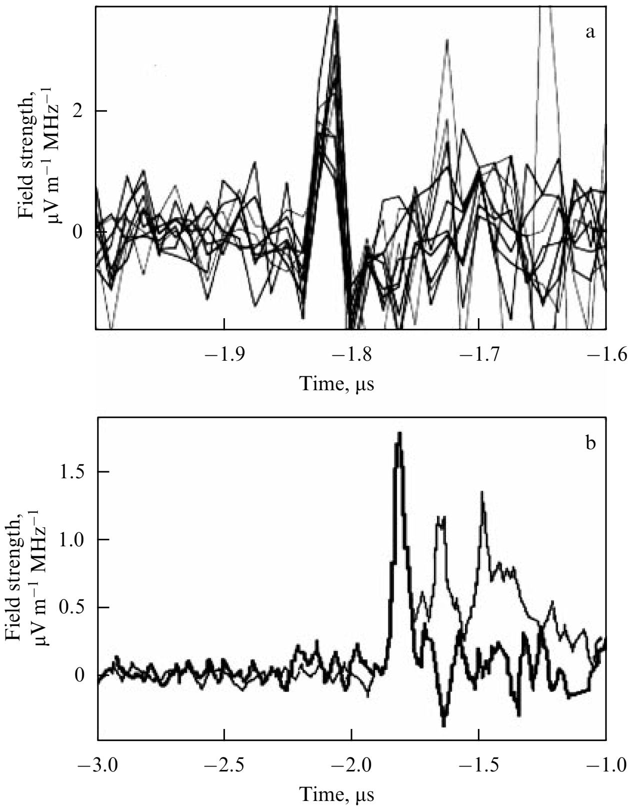

Figure 1. LOPES-10 event detected in March 2004 with the zenith angle 53°, the azimuthal angle 54°, and the primary energy 10^{17} eV: (a) electric field strength as a function of time near each of the LOPES-10 antennas; (b) electric field strength as a function of time after cc beam processing (thick solid line) and power-beam processing (thin solid line).

power is calculated as follows. The electric field strength in each antenna is squared, the results are added, the sum is divided by the number of dishes, and the square root of the obtained value is taken. During the cross-correlation processing, all possible products of the field strength at each antenna pair are composed. For example, let the electric fields be measured by $n = 5$ antennas. The number of all possible pairwise products is $n(n-1) = 20$, with half of them being the same. The results are then added, taken with their signs, the sum is divided by the number of antennas, and the square root of the resulting value is taken. This data analysis is sensitive to coherence effects. Therefore, the photomultiplier noise in Fig. 1b, being incoherent, is much smaller than the signal.

Based on the obtained results, the authors of [16] came to the following conclusions. Tilted air showers with a large geomagnetic angle and/or a large number of muons generate high-amplitude radio pulses that can easily be distinguished against the photomultiplier noise background. In addition, it is found that in contrast to the existing belief, the radio pulse amplitude normalized to the muon number increases as the geomagnetic angle increases for showers with high zenith angles [17]. This suggests that geomagnetic processes in highly tilted showers play a dominant role in the radio emission mechanism.

KASCADE's sensitivity rapidly decreases with the zenith angle. Nevertheless, this does not affect radio emission detection. The obtained results suggest that radio detectors can be used to discover highly tilted ultra-high-energy EASs. It is also shown that the small LOPES-10 array can discover events with zenith angles up to about 80°. This, in turn, means that such installations, but with a larger area, can be used in the future as possible detectors of neutrinos, for which showers with a larger tilt are more probable.

In 2005, the LOPES-10 detector was upgraded in order to study the transverse distribution of radio emission [18]. This was made possible due to the precise calibration of each individual antenna and rapid availability of information about each shower from KASCADE-Grande. Of special interest is the value of the parameter describing the signal decrease with the distance from the shower axis, and the dependence of this parameter on the primary particle characteristics. In addition, the information on the cross-beam distribution of radio emission can help understand the radio emission mechanism in detail (see the description of one of the models in [19]). The form of the cross-beam distribution can also be related to the primary particle energy or mass.

The configuration of LOPES-10 was upgraded so as to allow investigating different characteristics of radio emission. For this, the number of antennas with the east–west (E – W) orientation was increased to 30 (LOPES-30), the antenna base was increased, and low-noise amplifiers were installed. The LOPES antennas with the working frequency range 40–80 MHz were placed inside or near the KASCADE array and were E – W oriented in order to be sensitive to emission with the E – W polarization. Such a configuration was chosen to enable the study of the transverse field in the radio pulse, because the base length, which was about 260 m, allowed such measurements. The 0.8 ms time window for each antenna output signal was formed in KASCADE, with the number of samples in one cycle being 2^{16} at a discretization frequency of 80 MHz.

The LOPES trigger condition and data readout were determined by a high particle flux density in KASCADE. The trigger threshold corresponded to an energy $\approx 10^{16}$ eV and a count rate of about two events per minute. Each LOPES dish was calibrated individually with account for the KASCADE location and according to manufacturer's recommendations. The amplitude of the calibration signal was compared to that recorded by LOPES. The calibration procedure revealed a frequency dependence of the amplification coefficient on the antenna, cables, and the antenna surroundings (the conductivity of the ground, the presence of conducting objects, etc.).

The data obtained in the period 16.11.2005–08.12.2006 were analyzed for all the 30 E – W LOPES antennas. The data taking was stopped on 27 July 2006, due to damage caused by a strong thunderstorm, and renewed in September 2006. Over the KASKADE operation time, 996,000 triggers were directed to the LOPES array. About 10% of them were not processed due to a long 'death time' (1.5 s, the time that is required to restore the system to the working state) for the data readout from the memory block. A general reconstruction of events was performed for 860,000 records. Only a small part of these data showed the presence of radio pulses with an amplitude above the KASCADE-Grande noise level.

The cross-distribution of radio emission was studied from showers with a very high energy, which were accompanied by a powerful radio signal. To select such events, certain conditions had to be fulfilled. First, the shower axis had to pass through the KASKADE-Grande area not far away from the antennas. Consequently, the useful area was about

0.3 km^2. Second, the shower parameters could be reliably established from the KASKADE-Grande data only if the air shower energy was above $(3-5) \times 10^{16}$ eV. The number of such events was 296. In 12 of these events, the zenith angle was above 44°, and these events were rejected due to a large uncertainty of results derived from the KASKADE-Grande data analysis. The spatial distribution of radio emission could be studied only for bright radio signals in a time window of 90 ns. For this, the cc beam data processing was applied, and the signals from the southern direction were excluded. As a result, only 110 events were selected. In Sections 2.2.1–2.2.6, the main results obtained by the LOPES-30 detector are discussed [20, 21].

2.2.1 Correlation with the primary energy. The radio pulse amplitudes measured by the 30 antennas of LOPES-30 from events with the E–W polarization can be represented as a function of the geomagnetic field angle, the zenith angle, the distance from the antenna to the shower axis, or the primary particle energy as inferred from the KASKADE-Grande data analysis [15, 22]. The established relation among the geomagnetic angle, the distance to the shower axis, and the primary energy with the pulse amplitude is

$$E_{\mathrm{est}} = (11 \pm 1)\big((1.16 \pm 0.025) - \cos\alpha\big)\cos\theta \times \exp\left(-\frac{R_{\mathrm{SA}}}{(236 \pm 81)\ \mathrm{m}}\right)\left(\frac{W_{\mathrm{p}}}{10^{17}\ \mathrm{eV}}\right)^{(0.95 \pm 0.04)}\left[\frac{\mu\mathrm{m}}{\mathrm{m\ MHz}}\right],$$

where α is the geomagnetic angle, θ is the zenith angle, W_{p} is the primary energy, and R_{SA} is the mean distance from the antenna to the shower axis.

The authors of [15, 22] believe that the expression given above can be inverted to be used to estimate the primary particle energy from the LOPES-30 data. The statistical deviation of the LOPES-30 energy estimates from those of KASCADE-Grande is 27% for high-energy events. The KASKADE-Grande detector yields similar errors.

2.2.2 Accuracy of the direction determination. To investigate the possibility of radio measurements for determining a cosmic particle incidence direction, a four-dimensional radio image with a nanosecond time scale is constructed by digital data processing [23]. An attempt was made to find a multi-dimensional space parameter that could determine the maximum coherence of radio pulses from air showers. The result was compared with the direction inferred from the KASCADE-Grande data analysis. Each image point was defined by three spatial measurements as a function of time, obtained as the point of intersection of lines directed along the curvature radii of wave fronts through the antenna location. It was found that the emission direction can change with the curvature radius optimization. This dependence dominates over the statistical uncertainty in the direction determination from the LOPES-30 data. In addition, the curvature radius was found to increase with the zenith angle, i.e., when the shower comes from a longer distance. The distribution of direction misalignment obtained from LOPES and KASCADE data is presented in [23]. These data suggest that the misalignment decreases for large field strengths.

2.2.3 Frequency spectrum. The LOPES data on air showers with energies close to 10^{17} eV can be used to study the spectrum of the associated radio emission. Twenty-three high-amplitude events with the $\mathrm{E-W}$ polarization in the 40 MHz frequency band were analyzed. The data were power-beam processed (see above). The intensity was found to decrease with frequency for all showers. The spectral slope depends on the pulse duration: the longer the pulse is, the higher the spectral slope. Nevertheless, no significant dependence of the azimuthal angle, the zenith angle, the curvature radius, and the mean distance from the antenna to the shower axis on the electric field strength was found. The average electric field strength can be approximated by an exponential,

$$E(\nu) = K \exp\left(\frac{\nu}{\mathrm{MHz}}\,\frac{1}{\beta}\right),$$

where $\beta = -0.017 \pm 0.04$ and K is a dimensional coefficient, or by a power law $E(\nu) = K\nu^{\alpha}$, where $\alpha = -1.0 \pm 0.3$.

2.2.4 Cross-beam emission distribution. To analyze the cross-beam distribution, 110 air showers with a high signal-to-noise ratio were selected. The cross-beam radio power was approximated as $E = E_0 \exp(-R/R_0)$. Two free parameters, R_0 and E_0, describe the cross-beam profile and the electric field on the beam axis at the ground level. The data analysis showed that the intensity decreases exponentially with the transverse distance. However, 10% of the events showed a flat cross-beam distribution. According to [20, 21], this enigmatic feature of some air showers is not a hardware effect and should be investigated further.

Relatively recent papers [24–26] claim that this effect is due to cosmic particles heavier than hydrogen. For example, an iron nucleus interacts more strongly with the atmosphere than a proton does. Therefore, the depth of the maximum of an air shower, $X_{\max}$, triggered by an iron nucleus is to be observed at longer distances than that triggered by a proton. This suggests that the cross-beam radio power distribution $E = E_0 \exp(-R/R_0)$ from iron-induced showers can be flatter than that from proton-induced showers. According to Ref. [24], this fact is very important when assessing the radio method efficiency. The results of modeling with the new REAS3 code, which takes radio emission from the excessive charge into account [1, 2], showed good agreement with the LOPES data. In this connection, it is argued in Ref. [24] that the earlier version of the code for radio shower modeling, REAS2, should be revised.

2.2.5 Polarization measurements. After conducting measurements for one year by all 30 antennas with the E–W orientation, the LOPES-30 array was upgraded to allow simultaneous measurements by antennas with a north–south $(\mathrm{N-S})$ orientation. A simultaneous measurement by antennas with both polarizations could be used to check the expected effects from the geosynchrotron mechanism of radio emission in air showers. The first measurements revealed the dependence of the radio signal amplitudes with $\mathrm{N-S}$ and $\mathrm{E-W}$ polarizations on the azimuthal angle of the incident particle. The $\mathrm{N-S}$ antennas detected radio signals with a minimal amplitude, which, according to [21], may point to the geomagnetic origin of the shower radio emission.

2.2.6 LOPES-3D, an upgrade of LOPES-30. To extract maximum information from a radio signal induced by a high-energy air shower, the radio detection method was improved. For this, the LOPES array was upgraded to LOPES-3D [27, 28], which is able to measure all three components of radio signals from air showers. The additional measurement of the vertical field component, according to [27, 28], must increase the accuracy of restoring the primary particle parameters, including the incidence direction and energy, as well as the sensitivity to tilted air showers. To directly measure all three electric field components, nonstandard dishes were installed consisting of three mutually perpendicular dipoles. This change required the use of new low-noise amplifiers, as well as new calibration of the entire array. By the end of 2010, the commissioning and testing of the new LOPES-3D array by Karlsruhe Institute of Technology was successfully completed.

2.3 CODALEMA radio detector

The initial CODALEMA (Cosmic ray Detection Array with Logarithmic Electromagnetic Antennas) detector [29], located at the Nancy radio observatory (France), consisted of six broadband (1–100 MHz) antennas. The main part of this array included four dishes of the radio observatory itself, placed at the corners of an 83×87 m rectangle, and one narrow-band antenna (33–65 MHz) that was used to trigger the detector. One additional antenna, 1000 m away from the detector, was connected to it by an optical fiber line. The data was taken by digital oscillographs that recorded the signal amplitude at each of the antennas.

One of the first tasks was to identify different radio noise sources, including radio and TV broadcasting stations. The antenna outputs were connected to 24–82 MHz bandpass filters to suppress AM and FM stations that did not fall within the detector frequency range. The anthropogenic radio interferences were also filtered out. With these restrictions, the triggering rate of the detector was 12 events per minute. The trigger threshold at the antenna was 40 μV. Eighty-five percent of all triggers were rejected as noise pulses.

It is impossible to study the EAS characteristics without traditional detectors (i.e., air shower installations). Therefore, the CODALEMA detector was improved by installing a particle detector at the Nancy observatory, consisting of 13 stations put into stainless containers for weather protection. Each container contained a plastic scintillator and two photomultipliers. Additional antennas were installed to register radio pulses.

Figure 2 shows the position of 13 scintillators and 16 antennas. The particle incidence direction was determined by the time delay at each station. The number of particles in a shower was inferred from particle density measurements at the ground level. To study radio pulses accompanying the shower, only internal events, i.e., those for which the shower axis lies within the detector area, were selected.

As mentioned above, the first attempts to register radio pulses were performed using conical logarithmic antennas of a radio observatory. However, the huge sizes (6 m in height and 5 m in width) of these antennas prevented them from being used as a reliable and cheap element in the general construction of the detector. Therefore, by the end of 2006, the antennas in the Nancy observatory were replaced by dipoles, both of whose arms were made of aluminum rods 0.6 m in length and 0.1 m in width. Such a dipole was attached to the end of a dielectric mast 1 m in height [30]. The dipole was connected to a low-noise amplifier (with the amplification coefficient 34 dB) with an amplification nonuniformity of 3 dB in the frequency range 0.1–220 MHz. The effective

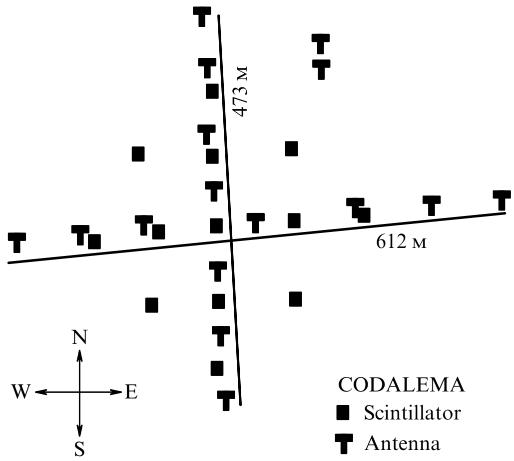

Figure 2. Location of antennas and scintillators in the modified CODALEMA detector area.

antenna length at low frequencies was almost constant, and the amplification coefficient did not depend on the radio wave direction. For a given length and thickness of the aluminum rods and the capacity connection to other elements of the construction, the antenna resonance frequency turned out to be close to 115 MHz and had a low quality. Therefore, the amplification coefficient in the wide frequency range from 1 to 100 MHz varied very insignificantly.

The designed antenna characteristics were tested by two means: by observing celestial point-like radio sources and by direct measurement of galactic radio noise. Because anthropogenic noise has a maximum intensity at frequencies below 20 MHz and the FM broadcasting noise is concentrated within the 88–110 MHz band, the bandpass filter (25–85 MHz) attached to the antenna output provided normal conditions for the amplifier operation. In the advanced CODALEMA detector, the digital oscillographs were replaced by high-speed electronic devices [31]. After several tests, the authors of Ref. [31] concluded that further improvement of the detector was needed.

At the 31st International Cosmic Ray Conference (2009, Lodz), the additional modification of the CODALEMA detector and first results of polarization effects connected to the geomagnetic field were reported [32]. The modified detector consisted of 17 units and 24 antennas, including 21 E – W and three N – S dishes. The position of the antennas is shown in Fig. 2.

After passing through bandpass filters (23–85 MHz), radio pulses were reconstructed and compared with the data from the ground particle detector. The first observations revealed a linear relation between the electric field strength and the cross product $\mathbf{v} \times \mathbf{B}$, where $\mathbf{B}$ is the geomagnetic field induction and $\mathbf{v}$ is the cascade disk velocity.

Subsequent analysis was based on data taken in 453 days of observations under stable weather conditions, i.e., in the absence of atmospheric electric events. To determine the air shower direction, events recorded by at least three antennas were considered. A radio pulse was associated with a shower if its characteristics were comparable to the particle detector data. This meant that the direction misalignment was less than 20° and the time difference less than 0.2 μs [33]. Distribution of the 'radio shower' directions (i.e., showers that were registered together with the radio pulse) proved to be strongly anisotropic.

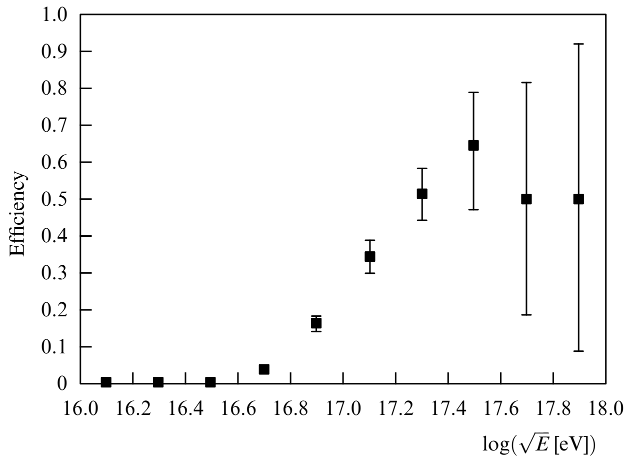

Figure 3. Dependence of the CODALEMA detector efficiency on the primary particle energy.

2.3.1 Efficiency of the radio detector. Two units made two independent measurements of the shower axis, direction, and time of arrival. These can be used to uniquely identify the air shower accompanied by the radio pulse. As previously, a radio pulse was associated with a shower if its characteristics matched those derived from the particle detector. From 26 November 2006 until 20 March 2008 (355 days in total), data about air showers were obtained under good weather conditions. The main characteristics of these events are listed in Table 1. The energy threshold of the radio detector and particle detector was about 10^{17} eV and 10^{15} eV, respectively. The efficiency of the radio detector was determined as the ratio of the number of showers with radio pulses to the number of events registered by the scintillation detector in the chosen energy range in the same time interval. The dependence of the efficiency on particle energy is presented in Fig. 3.

Table 1. Air showers observed by the CODALEMA detector from 27 November 2006 until 20 March 2008.

Events	Scintillators	Antennas	Coincidences
Reconstructed	61,517	750	619
Internal	28,128	195	157
$E > 10^{16}$ eV	7889	169	154
$E > 5 \times 10^{16}$ eV	692	134	129

2.3.2 Asymmetry of events caused by the radio detector. The data obtained by the particle detector and radio detector allow determining the cosmic particle incidence direction over the entire area of the detector (internal events). The projection of the cascade axis directions onto the sky is shown in Fig. 4. The dominance of northern events over southern events is clearly seen. The ratio of the south direction events N_S (i.e., with the azimuth $90° < \phi < 270°$) to the total event number N_{tot} is $N_S/N_{tot} = 0.17 \pm 0.02$. This asymmetry cannot be explained by geometrical features of the particle detector location, because the event distribution from the particle detector without taking the radio detector data into account is isotropic. The difference between the asymmetric distribution and the isotropic one is 16 standard deviations. A check revealed that the asymmetry level does not depend on the data sequence. Seven independent measurements yielded the same result (i.e., about 0.17). For high-energy events only, the ratio N_S/N_{tot} increased to 0.5, which, in fact, implies the isotropization of axis directions. From this fact, it was concluded in [33] that the observed effects are, in particular, due to the radio detector energy threshold.

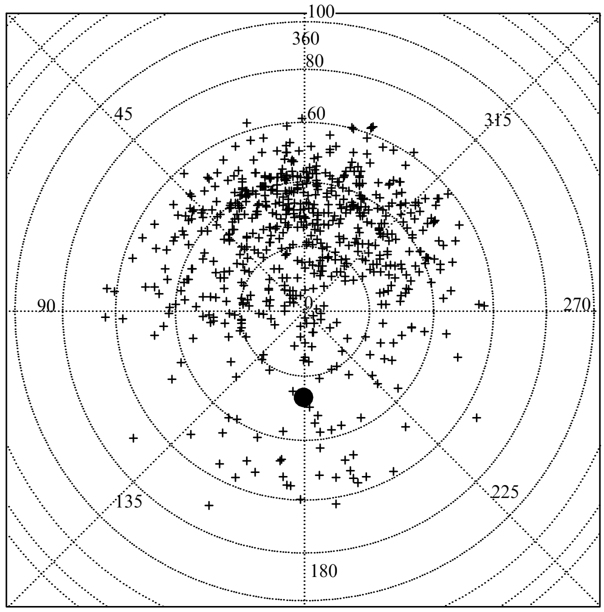

Figure 4. Projection of air shower axes onto the sky. The zenith is at point 0. The azimuthal angle is measured from the direction to the north (W — 90°, S — 180°, E — 270°). The projection of the geomagnetic field at the CODALEMA detector location is shown by the black dot.

The discovered asymmetry becomes clear when taking the geomagnetic field effect on the cascade shower into account. In the geomagnetic field, electrons and positrons of the cascade disk have a centripetal acceleration resulting in electromagnetic emission. Charged particles with opposite signs have oppositely directed accelerations. They produce an electromagnetic field, which is observed as a short radio pulse due to relativistic effects. The electric field vector is parallel to the line connecting oppositely charged particles. In other words, the radiation field predominantly has the E–W polarization. A simple model of this mechanism is described in [3]; this is frequently referred to as the geosynchrotron mechanism.

It is clear that the field strength in this case is proportional to the cross product $\mathbf{v} \times \mathbf{B}$. The CODALEMA detector is located in the northern hemisphere; therefore, the geomagnetic field induction vector $\mathbf{B}$ is tilted to the north. The maximal value of $\mathbf{v} \times \mathbf{B}$ corresponds to showers with the N–S axis sky projection. Thus, even weak air showers coming from the north can induce a higher radio signal than stronger showers coming from the south. This is the reason for the asymmetry (see Fig. 4) when dipoles with E–W oriented arms are used in the detector.

2.3.3 Further upgrade of CODALEMA. The main purpose of the CODALEMA detector upgrade is to construct a new-generation detector that can operate autonomously. For this, at the end of 2011, the antenna array was increased to 60 stations covering an area of 1.5 km^2 [34]. The energy range of the detector was extended to 10^{18} eV, and the relative

Table 2. Parameters of the 'radio event' candidates obtained in June 2011 by the separate upgraded autonomous station of the CODALEMA* detector.

Date	Number of simultaneously running stations	θ_{sc}	ϕ_{sc}	$\Delta\Omega$	ψ_{pred}	ψ_{meas}
2011.06.17	1	32.2°	−55.6°	—	58°	58°
2011.06.23	3	29.6°	−6.0°	2.9°	87°	86°, 87°, 84°
2011.06.26	1	42.0°	20.0°	—	77°	75°
2011.06.27	1	27.1°	104.7°	—	36°	36°

* θ_{sc} and ϕ_{sc} are the respective zenith and azimuthal angles obtained from the particle detector data, $\Delta\Omega$ is the angle between the EAS axes found from data from both detectors, and $\psi = \arctan(E_{EW}/E_{NS})$ (ψ_{pred} is the value predicted from θ_{sc} and ϕ_{sc}, and ψ_{meas} is the measured value).

efficiency reached 100%. The modified array is aimed at tackling several problems related to reliable detection of extensive air showers from UHECRs.

The radio detector stations were mostly upgraded. The autonomous station designed by the CODALEMA collaboration was constructed with the use of the experience of operating the first prototype, in which a successful solution providing triggering of the radio detector by a cascade shower was found. The autonomous station triggered the detector by itself, digitized and processed the radio signal, performed the signal timing, and maintained the relation with other elements of the radio detector. The new antenna installed in this station provides both E−W and N−S polarization measurements. Several such radio detectors were successfully tested in the CODALEMA array at the Pierre Auger Observatory in 2010.

The autonomous antenna, which collected the data in June 2011, discovered four events with all the signatures of radio pulses from air showers. The four selected events coincided in time within 5 μs with the particle detector data. The data on these showers are listed in Table 2.

It was assumed in [34] that the new array can provide high-precision measurements and will increase the amount of statistics on high-energy showers. The above facts, as the authors of Ref. [34] believe, are already a great achievement on the way to creating an autonomous detector. In addition, from the physical standpoint, there are no fundamental objections to determining the type of a cosmic ray particle using an antenna array, which is another important argument supporting the radio detection of air showers.

2.3.4 Reconstruction of the curvature radius using the CODALEMA detector. Because theoretical studies indicated that the shape of a radio signal depends on the longitudinal air shower development, the shape of the wave front was expected to bear information on the primary particle nature. At the first stage of analysis of the CODALEMA experimental data [35], the wave front was assumed to be a plane determined by the shower time of arrival and the antenna locations.

A more detailed analysis showed (Fig. 5a) that in most cases, the wave front form is somewhat different from the plane, and such a curved geometry, according to some authors, suggests the existence of an effective region of radio emission during the air shower development. One of the simplest hypotheses to explain these experimental features assumes that the radio pulse maximum is related to the radio signal source center on the shower axis. This allows determining the curvature radius R_c. Some models presume that R_c can correspond to the shower maximum X_{max}, which is directly related to the cosmic particle type. This possibility is investigated using the existing data.

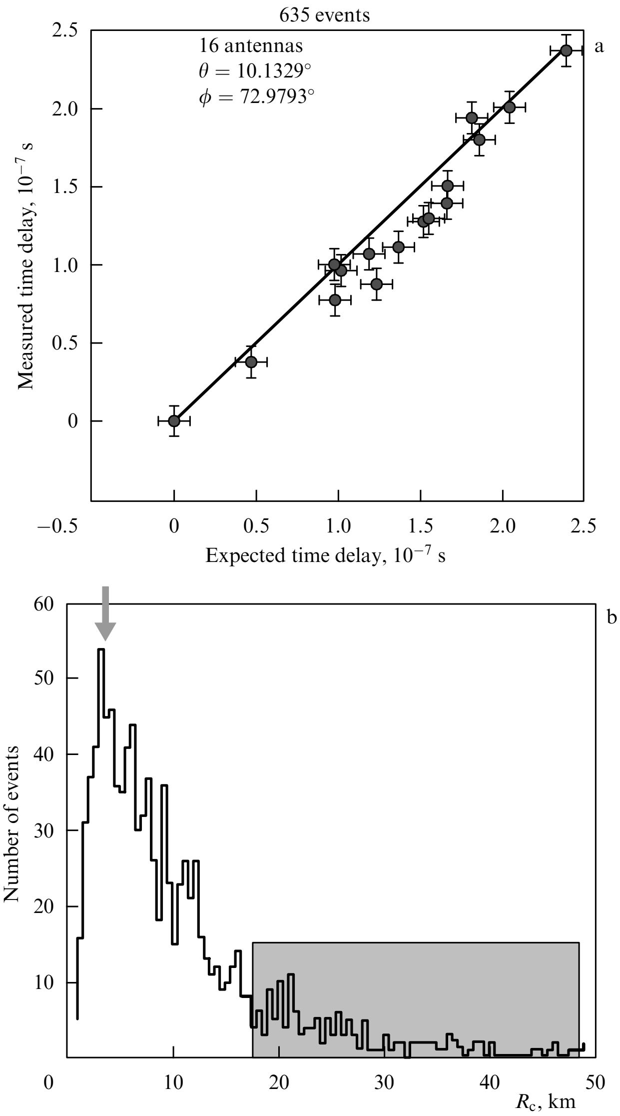

Figure 5. (a) Expected time delays. The straight thick line corresponds to a plane wave front. Points outside the line indicate deviations from the plane wave front. (b) Distribution of the curvature radius R_c for 1010 selected events. The distribution maximum (shown by the arrow) corresponds to the curvature radius of 4 km.

The chosen method [35] uses the difference between the real wave front, as determined by the times of arrival distribution, and a plane front. To calculate this difference, the wave front is approximated by a parabola. The results of calculations are presented in Fig. 5b. The distribution of R_c shows a maximum at a distance of 4 km, in general agreement with the characteristic emission maximum expected, but extends up to distances of 20 km. The authors of [35] note that the physical interpretation of this fact is unclear. For example, it may be due to the scarcity of time arrival data or errors in the time measurements; the time of arrival uncertainty was assumed to be 10 ns.

2.4 Detection of horizontal neutrinos behind a rock massif

The method of detection of horizontal neutrinos behind a rock massif is based on the theoretical possibility of detecting strongly tilted air showers due to a τ-lepton decay in Earth's atmosphere.

It is known that neutrinos of different flavors (ν_e, ν_μ, and ν_τ) interact differently with target matter (ground, water, ice, etc.) Charge current (CC) reactions produce leptons of different flavors and hadrons:

$$\nu_\ell(\bar{\nu}_\ell) + \mathrm{N} \to \ell^{\pm}(\ell^{\mp}) + X\,,$$

while neutral current (NC) reactions yield neutrinos of different flavors and hadrons as well:

$$\nu_\ell(\bar{\nu}_\ell) + \mathrm{N} \to \nu_\ell(\bar{\nu}_\ell) + X\,,$$

where $\ell = \mathrm{e}, \mu, \tau$, and X denotes all possible hadrons produced in these reactions. The ratio of CC to NC reactions is determined by the cross section of the interaction with matter [36, 37]:

$$\sigma_{\nu\mathrm{N}}^{\mathrm{CC}} : \sigma_{\nu\mathrm{N}}^{\mathrm{NC}} \approx 7:3\,.$$

In the NC interactions $\nu_e\mathrm{N}-\mathrm{CC}$, the reaction products, electrons and hadrons, initiate cascade showers near the interaction points. At very high energies, the electron-induced cascade in a dense medium is strongly elongated due to the Landau–Pomeranchuk–Migdal (LPM) effect, and is therefore virtually undetectable by radio antennas. In a hadron cascade, π^0 mesons lose energy due to relativistic effects to $10^{13}-10^{14}$ eV before decaying, and the cascade turns out to be too short to be detectable by an electromagnetic pulse in a dense medium. This fact is crucial for the radio method justification. Nearly the same also holds for the $\nu_\mu\mathrm{N}-\mathrm{CC}$ reactions, in which the muon produced does not decay but spends most of the energy for medium ionization, bremsstrahlung radiation, e^+e^- pair production, and photonuclear reactions. At high energies ($W_\mu > 10^{12}$ eV), the e^+e^- reactions dominate, which results in cascade showers subjected to the LPM effect in a dense medium ($W_{\mathrm{LPM}} > 10^{14}$ eV).

In $\nu_\tau\mathrm{N}-\mathrm{CC}$ reactions, the τ lepton loses energy mainly in the photonuclear reactions if its energy is $W_\tau > 10^{15}$ eV. The τ lepton, which has a mass of 1777 MeV, is the only lepton capable of decaying into hadrons, because other leptons are too light. The decay channels of the τ lepton, $\tau^- \to \mu^- + \bar{\nu}_\mu + \nu_\tau$ and $\tau^- \to e^- + \bar{\nu}_e + \nu_\tau$, have a probability of about 35%, and the probability of decay into hadrons is more than 50%. The mean lifetime of the τ lepton is 2.9×10^{-13} s. For example, in the vacuum, owing to relativistic effects, a τ lepton with the energy $W_\tau = 10^{15}$ eV would travel about 49 m before decay (Lorentz factor $\gamma \approx 5.6 \times 10^5$).

A τ lepton can decay via many channels, but all of them contain a τ neutrino in the end. This explains why at high energies ($W > 40$ TeV), Earth, which is opaque for ν_e and ν_μ, is always transparent for τ neutrinos, because the ν_τ-neutrino flux regeneration occurs. From each primary ν_τ with an energy W_0, the CC reaction of the τ lepton decay generates another τ neutrino, but with the energy $W_1 = W_0/3$. The regeneration of τ neutrinos continues until they come out of Earth.

If the ν_τ flux incident at a small angle to the horizon meets an extended rock massif, then a τ lepton has a probability of coming out into the atmosphere after the $\nu_\tau\mathrm{N}-\mathrm{CC}$ interaction, if the interaction vertex is located near the surface of a mountain. The radio pulse produced by the cascade shower during the hadron decay of a τ lepton in Earth's atmosphere can be registered by antennas placed near a rock massif.

One such project was presented at the 38th International Cosmic Ray Conference in Moscow [38]. The authors of [38] estimated the sensitivity of a detector equipped with highly directed antennas to register the air shower induced by a τ-lepton decay. As noted above, this is possible near mountains where the τ lepton can be produced due to the τ-neutrino interaction with matter. In particular, the authors of [38] found that an antenna with an amplification factor of 16 dBi (isotropic decibels) in the 20–80 MHz frequency range provides a high signal-to-noise ratio at a distance of 20 km from the shower with an energy of 10^{16} eV. The estimates presented in [38] suggest good prospects for this method of neutrino detection.

Tian-Shan experiment with a large antenna array. In 2007, in the Tian-Shan mountains at an altitude of 2650 m, the Chinese Academy of Sciences constructed a radio interferometer to observe interstellar hydrogen at the reionization epoch. The large distance to such hydrogen corresponds to a redshift such that the frequency of interstellar hydrogen emission ($\nu \approx 1420$ MHz) is shifted into the 50–200 MHz frequency range (depending on the distance to a particular source). The radio interferometer was called the Primeval Structure Telescope (PaST) or the 21 Centimeter Array (21CMA). According to [39], the location of the 21CMA is well suited to detect air showers produced by atmospheric τ-lepton decays. Owing to the remoteness of the radio interferometer from industrial and densely populated areas in China, the 30–80 MHz frequency range, which is necessary to conduct the experiment, is extremely clean, i.e., almost free from anthropogenic electromagnetic noise exceeding galactic radio noise.

The 21CMA consists of 10,160 logoperiodic antennas grouped into 80 clusters with 127 antennas each. The interferometer consists of two mutually perpendicular shoulders directed along the N–S and E–W axes. The shoulders are placed at the bottom of two high mountain valleys and are 4.0 and 2.8 km long. The information from each cluster is passed to the central station via a fiber cable, which significantly decreases electromagnetic noise.

The basic concept of TREND (Tian-Shan Radio Experiment for Neutrino Detection) is that the 21CMA can be used as an autonomous (self-triggering) detector of air showers after a minor upgrade of the existing setup.

The authors of [39] assume that the measurement of cosmic neutrino flux can be best performed using the detection of strongly tilted air showers from τ leptons produced in the $\nu_\tau\mathrm{N}$ reaction. Several arguments are used to justify this assumption:

• the 21CMA interferometer is surrounded by very high mountains (with the altitude up to 5000 m), which is optimal for τ-neutrino detection, because the mountains play the role of a huge target for neutrino interaction, which significantly increases the air shower occurrence rate in comparison with that in plain surroundings [40, 41];

• in the final configuration, 80 antennas of TREND will be placed over a length of several kilometers along two of the interferometer shoulders, which will allow the spatial development of air showers along the interferometer shoulders and precise timing;

• the main goal of the TREND experiment is to provide an autonomous operation of the detector owing to an extremely good interferometer location and minimal level of the anthropogenic noise background.

The authors of [40, 41] believe that TREND will be a very sensitive instrument to detect neutrinos with energies about 10^{17} eV.

To test the autonomous operation of radio antennas, a TREND prototype consisting of six antennas was deployed and tested for several months in January 2009 at the 21CMA location. The signal in each antenna was amplified to 64 dB and after passing through a bandpass filter (50–100 MHz) was supplied to an optical transducer located in the center of the cluster. To test the setup, radio noise was recorded every 5 min for 5 months. The TREND prototype clearly detected a periodic increase in the noise level when the galactic plane (seen as the Milky Way) crossed the antenna beam [42], while this effect was very weak in the CODALEMA experiment. The very low radio noise level enables the calibration of the installation using bright sky radio sources. However, this calibration method was not used, and the radio pulse amplitudes were normalized to the instantaneous RMS noise level, which was also measured at the end of data taking.

The first step of the autonomous data analysis consists in searching for coincident triggers from several antennas. This is done by arranging the arrival times of signals at each antenna and subsequently selecting coincident signals from the possible source [39]. The triggering of antennas is assumed to be causally related if the condition

$$|t_i - t_j| \leqslant \frac{d_{ij}}{c}\, T$$

is satisfied for the ith and jth antennas, where d_{ij} is the distance between the antennas, c is the speed of light, and $T \approx 1.1$ is the correction factor due to time determination errors. If at least four consecutive triggers from four different antennas satisfy this condition, the event is selected for further analysis (see [40] for more details).

In 2009, data were collected over 584.7 hours from six antennas of the TREND prototype [40, 43]. However, 31% of this time can be related to enhanced galactic noise. In the remaining 69% of the time, 2275 events were recorded. The radial and angular coordinates respectively correspond to zenith and azimuth angles. Events recorded simultaneously by four, five, and six antennas are mainly located near the horizon and in most cases are related to radio noise. Some of them lie in the northern direction. This cannot be due to the presence of a noise source in the northern direction, while there are such sources in other directions; for example, there is a railway to the south, a railway station to the east, and a digital data processing center and electrical transformers to the west.

Thus, of 2275 events, only 37 radio pulses were selected. Another 12 events were excluded from the further analysis. The remaining 25 events are clearly separated in time and space and are therefore considered to be the best air shower candidates. We note that 15 of the reconstructed directions lie in the north sky, where there are no radio noise sources, as noted above. The authors of [39] believe that because several important factors were ignored in the analysis (in particular, the antenna lobes), it is premature to explain the observed north–south anisotropy by the geomagnetic origin of the radio signal, as was the case in the CODALEMA experiment (see, e.g., [44]).

Because these 25 events were registered in the course of 17 days, their mean occurrence rate (1.5 events per day) with account for the total area of 2×10^4 m^2 corresponds to a shower energy exceeding 10^{17} eV, which is a very realistic energy threshold for this installation.

In January 2010, the TREND prototype detector was upgraded to 15 antennas placed near the crossing point of the baselines of the 21CMA detector in a total area of $350\,\text{m} \times 800\,\text{m} \approx 0.2$ km^2. Several events were selected for further reconstruction. In addition, three particle detectors separated by 200 m were installed at the same place. These detectors consisted of plastic scintillator and photoelectric multipliers. The two systems ran simultaneously for several days. Three air shower candidates were selected from the radio antenna data. These events were carefully studied to determine whether they could be produced randomly due to thermal fluctuations or galactic noise. The probability of spuriously triggering all detectors in a 2 μs time interval was estimated to be 0.1 events per year. Therefore, the authors of [39] concluded that these three events do correspond to air showers. Independent reconstructions of the assumed air shower directions in both detectors are in good agreement. Thus, it was concluded that the TREND radio array is suitable for autonomous operation.

2.5 Joint observations of air showers by a radio array and a particle detector at the Pierre Auger Observatory

The main goal of the Pierre Auger collaboration is to detect UHECRs with energies close to the Greisen–Zatsepin–Kuzmin (GZK) cutoff at $\sim 5 \times 10^{19}$ eV to study their origin. Such high-energy particles are presently inaccessible with modern accelerators. It is necessary to determine the particle energy, incidence direction, and type (whether it is a proton, a nucleus, or a neutrino). Basically, the Pierre Auger Observatory includes 1600 ground (scintillator and photomultiplier) detectors and four telescopes consisting of six fluorescent detectors. The working area of the observatory is about 3×10^3 km^2.

Air shower radio detection started in the 1960s. Now it is widely accepted that the radio pulse is mainly generated by the geomagnetic or geosynchrotron mechanism, i.e., emission from relativistic electrons and positrons from a shower in Earth's magnetic field. Because the thickness of the cascade disk is less than a few meters, the coherent emission region must be within $0 < \nu < 100$ MHz.

The radio detection method has the following advantages over traditional detection methods. The radio signal is not absorbed and scattered: its amplitude is proportional to the primary energy of the shower, which allows a detailed study of the shower front. In addition, radio detection is possible during the whole day, whereas fluorescent detectors can operate only during cloudless nights. The shower detection method employed by the Pierre Auger Observatory requires simultaneous detection of an event by the surface and fluorescent detectors, and the radio method can provide additional information about the shower.

The radio method estimates the primary particle energy and its incidence direction, which can be an additional means to solve some problems of high-energy astrophysics. As the authors of [45] note, for this method to be fully implemented at the Pierre Auger Observatory, several problems related not only to physics but also to technology, investment, and operating costs need to be solved. Here, the experience from the LOPES and CODALEMA experiments is of great value.

The first studies, started in 2006, were related to the location of antennas and radio electronics in the south part of the Pierre Auger Observatory. It was planned to complete the construction in four years (starting in 2008) and run the installation with an area of 20 km^2, which would be a prototype of a 1000-kilometer radio antenna array.

The immediate goal was to optimize the equipment and software needed for the 20 km^2 array to be deployed in the southern part of the Pierre Auger Observatory. The array had to be able to be autonomously triggered by an air shower, and have an internal data readout system to become independent in this way from the Pierre Auger Observatory. The necessary correlation between the radio array and the main detector is provided by the Global Positioning System (GPS) timing. Data readout optimization has various components, including the antenna design, preliminary amplification at the antenna stations, filters (analog and/or digital), the amplification coefficient, the receiver, and the digital transformation and analyzer of signals.

The general design depends on both the low noise level requirement in all units and the possibility of suppressing external radio interference. The latter includes Galactic radio noise, atmospheric discharges, continuous broadcasting signals, TV transmitters, and radio pulses from various electric devices. The anthropogenic radio noise level is known to highly depend on location and to strongly increase toward low frequencies. In nonindustrial low-populated areas, Galactic noise dominates over the anthropogenic ones.

Different types of dipole antennas can be used [45]. In one project, a double active thickened dipole 1.2 m in length and 1 m in height that has a sufficiently uniform amplification in a wide frequency band is used for two polarization measurements. In another project, a comparatively large logoperiodic antenna is employed. In this project, two antennas (one for each polarization) are attached to a 4 m mast at each station. The amplification of these antennas quite rapidly decreases at frequencies below 35 MHz but stays almost constant in the 35–90 MHz range. In addition, a double inverted vee dipole (a wire dipole raised on a mast with shoulders lowered to the ground) was tested on a 5 m mast. The amplification of this antenna smoothly changes with frequency and has a maximum at around 60 MHz.

The results of observations with the prototype in the south part of the Pierre Auger Observatory are briefly reported in [46]. These small prototypes must solve many technological problems before the big radio array is deployed.

The promising results obtained by the radio array prototype encouraged the Pierre Auger collaboration to deploy the large-scale AERA (Auger Engineering Radio Array), which in the complete form will cover an area of 20 km^2 with 150 stations to register about 5000 events a year. AERA will be deployed in the north–west part of the observatory, where the HEAT (High Elevation Auger Telescope) detector [47] and AMIGA (Auger Muons and Infill for the Ground Array) detector [48] (both to be upgraded) are located. Jointly with the HEAT fluorescent detector and the AMIGA muon detector, the AERA radio detector will provide additional information for hybrid data analysis in the corresponding energy range.

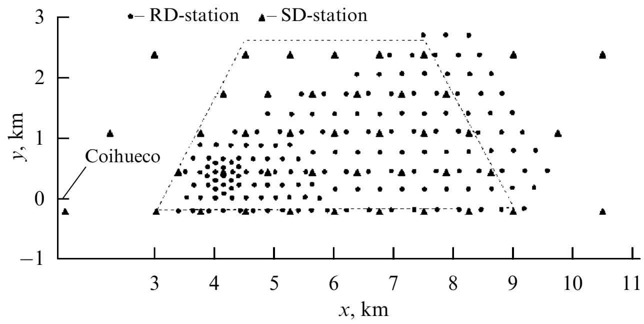

Figure 6. Plan of the AERA antenna array location. Circles show radio detector stations (RD), triangles show surface detector stations (SD). Coihuecco is the fluorescent detector (FD) located near one of the SD stations.

AERA will be a prototype of a large radio array dedicated to the following scientific tasks:

(1) careful analysis of radio emission from air showers with energies above $10^{17.2}$ eV; in particular, testing the theoretically predicted [49] identity of parameters of radio emission from low- and high-energy air showers;

(2) estimate of the capability of a large-scale radio array to determine the main characteristics of cosmic particles (energy, direction of arrival);

(3) high-precision measurements of the energy spectrum and composition of cosmic rays in the energy range $10^{17.4}-10^{18.7}$ eV, where the transition from Galactic to extragalactic cosmic rays occurs.

To achieve these goals, AERA will include about 150 antennas with multi-step location (Fig. 6). The core will consist of 24 antennas placed at the nodes of a uniform triangle net with a step of 175 m. This array will be surrounded by 60 antennas, also arranged into a uniform triangle net but with a step of 250 m. The external region will have 72 antennas separated by 375 m intervals. Each of the autonomous detector stations will be tuned for observations in the frequency range from 30 to 80 MHz and will be autonomously triggered by radio pulses from air showers.

The deployment of the 1000 km radio array in the course of the Pierre Auger Observatory upgrade will undoubtedly lead to a big advance in the UHECR detection technique.

In 2011, at the 32nd International Cosmic Ray Conference, the first stage of the AERA prototype was reported to be greatly modified and close to completion [50]. The number of detector stations at the first stage was 21. They were separated by 150 m from each other. Each station has logoperiodic dipole antennas with E – W and N – S orientations with the working frequency range 24–84 MHz. Each antenna is equipped with low-noise amplifiers with the amplification coefficient 20 dB. More details about the antennas to be used in AERA are provided in [51]. A multi-range radio transmitter ('beacon') placed near the fluorescent detector will provide radio signals for time calibration of AERA. The use of such radio markers will allow time delay correction at each station, which will significantly increase the time resolution of the setup [52].

The first stage of the AERA prototype started stably operating in March 2011. The first coincident hybrid radio event (an SD radio event; SD from 'surface detector') was recorded in April 2011. The coincidence coefficient was about 0.3. These observations discovered the N – S asymmetry, as expected in the theory of geomagnetic radio emission.

The first superhybrid event, i.e., the simultaneous registration of a shower by all three detectors (radio, surface, and fluorescent), was recorded on 30 April 2011.

The first results obtained by the AERA-24 prototype are discussed in [53]. By 27 February 2013, 356 events have been detected, and some of them were processed jointly with data obtained by the fluorescent detectors and surface detectors (muon counters). Of the 356 events, 229 were registered by the radio detector due to triggering from the surface detectors; 127 events were autonomously registered by the radio detector antennas, with 29 of them recorded from triggering by more than three antennas.

The mean angular deviation between the directions of the shower determined by AERA and the surface detectors is about 4°. According to [53], this misalignment can be made smaller in the future by improving the direction determination accuracy and time calibration. The mean energy determined by the surface detectors was about 1 EeV, with the energy of some events being below 0.1EeV and one event showing the energy 4.3 EeV and the tilt angle 58.4°.

The AERA data were analyzed by different means and compared with modern modeling of radio emission from air showers. The AERA events with high amplitude at several antennas were selected. The parameters of these events as derived from the surface and radio detector data were modeled using codes CoREAS [54], ZHAires [55], EVA [56], and SELFAST [57].

No contradiction with the general picture of radio emission generation was found. The dominant process is the deflection of shower electrons and positrons in Earth's magnetic field [3, 58]. The radio emission due to the Askar'yan effect, i.e., due to an excess of negative charges, makes only a minor (but non-negligible) contribution compared to the geomagnetic effect. Both processes depend on the refractive index of air, which changes the coherence conditions for radio emission. This, in particular, explains the side distribution of the radio signal amplitude, which first increases with the distance up to 100 m from the shower axis, and then decreases, as was predicted more than 40 years ago.

In addition, the radio signal amplitude from the AERA detector was confirmed to be independent of the primary particle energy [59]. To determine the type of a cosmic particle, three parameters of the radio signal sensitive to shower development were used: the slope of the cross distribution, the shape of the radio front, and the spectral slope. The last parameter is more advantageous, because determining the spectral slope requires only one station, and the length of the shower can be estimated, for example, from the surface detector data.

Electric field strength measurements using these data were reported in [60, 61]. Here, a component that cannot be explained by the geomagnetic emission mechanism was measured. The authors of [60, 61] believe that this component can be due to emission from excessive charge in the shower. In this experiment, Earth's magnetic field induction was assumed to be 24 μT, the field inclination angle was taken to be 36.6°, and the declination angle was 2.7°. Only showers with zenith angles $\leqslant 55°$ were analyzed.

2.6 Ultra-high-frequency emission from air showers

In recent years, several experimental papers have reported that EAS propagation is accompanied by emission in the gigahertz frequency range with enough power to be observed. These claims may seem to be wrong, because such high frequencies correspond to wavelengths of about 3–10 cm, which are much smaller than any geometrical sizes of showers. The last fact, in turn, implies that the coherent addition of waves is virtually impossible and the radio signal should be very weak.

However, several groups have conducted experimental tests of these effects in accelerators, which gave positive results. Moreover, there are several reports on the direct registration of microwave emission from air showers. Theoretical efforts are currently aimed at finding possible radiation mechanisms that could provide detectable radio power. The possibility of ultra-high-energy (UHE) emission from air showers was previously studied in [62] (see also [63]).

We consider the arguments used by the authors of [62] for their estimations. First, the UHE emission is assumed to be generated by thermalized electrons that were thrown from air molecules with insufficient energy for subsequent ionization. Essentially, this is bremsstrahlung radiation of electrons colliding with air molecules. The microwave molecular bremsstrahlung radiation (MBR) propagates in all directions from the shower axis; therefore, detectors can reconstruct the two-dimensional trajectory of the shower in the sky. In addition, times of arrival of radio pulses can be used to determine the complete air shower reconstruction.

Further justification of this standpoint is as follows. It is known that the minimal flux density of bremsstrahlung radiation of a plasma is given by the classical expression

$$\eta_\omega(u) = \frac{e^2}{16\pi^3 \varepsilon_0 c^3}\, u^2 \nu_{\rm en}(u)\, \zeta(\nu_{\rm en}, \omega)\,,$$

where ω is the radiation frequency, u is the mean velocity of electrons, $\nu_{\rm en}(u)$ is the collision frequency of electrons with neutral molecules, $\varepsilon_0 = 8.85 \times 10^{-12}$ F m^{-1} is the dielectric constant, and $\zeta(\nu_{\rm en}, \omega)$ is the suppression factor due to the interference of fields in frequent consecutive collisions. For an isotropic and stationary velocity distribution,

$$\zeta(\nu_{\rm en}, \omega) = \frac{1}{1 + (\nu_{\rm en}(u)/\omega)^2}\,.$$

At a height of 5 km, the collision frequency is $\nu_{\rm en}(u) \approx 3$ THz for an electron energy of about 2 eV, which corresponds to the maximal value for elastic collisions. For room temperature electrons, $\nu_{\rm en}(u) \approx 40$ GHz. The respective compression factors for these typical collision frequencies are $\zeta = 5 \times 10^{-5}$ and $\zeta \approx 0.4$.

To justify the possibility of detection of UHF emission from a shower, several tests were performed on accelerators to measure the MBR in laboratory conditions. In these experiments, solid evidence was obtained that the properties of noncoherent MBR differ from the standard picture.

We consider the method of these measurements and the obtained results in more detail.

2.6.1 AWA accelerator experiment. In June 2003 at the Argonne National Laboratory operated by the University of Chicago, an experiment was carried out at the superconducting linear accelerator, in which an electron beam with a

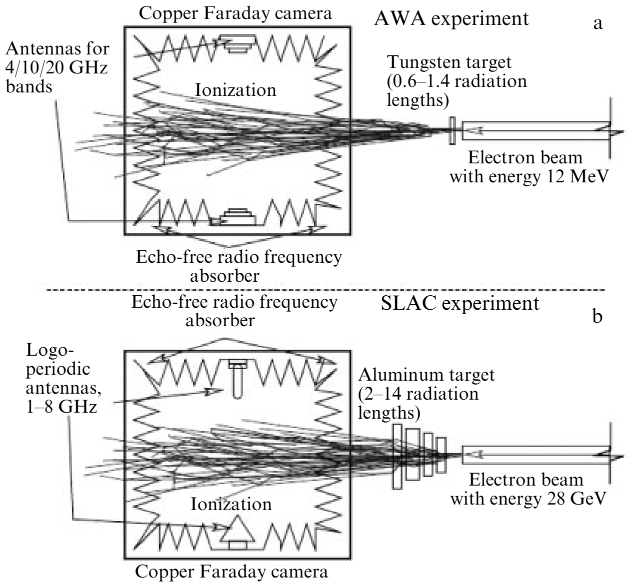

Figure 7. Schematics of the (a) AWA and (b) SLAC experiments.

charge ≈ 7 nC in one pulse and an energy of 12 MeV was used. The beam contained 4×10^{10} electrons with a total energy of 5×10^{17} eV. The longitudinal size of the bunch (individual pulse) was 1.2 cm. The electrons encountered tungsten plates 2 or 5 mm thick (the radiation length in tungsten is 3.5 mm) to produce gamma-ray photons with an energy of 5–10 MeV, as well as electrons with a somewhat lower energy.

As a rule, 40%–90% of the total energy of the beam is converted into photons directed toward a chamber filled with air under atmospheric pressure. The energy of electrons, 12 MeV, was chosen to be significantly lower than the critical energy of electrons in air (~ 80 MeV) so as not to produce a shower in the chamber. The transformation of the electron energy into gamma rays allows avoiding a large excessive negative charge due to the electron beam passing through a Faraday chamber. The photons come into the copper chamber filled with air ~ 1 m^3 in volume, which prevented radio noises from the external electromagnetic emission to arise and helped the transitional radiation due to electrons coming out from the chamber walls to be absorbed. A small fraction of electrons could pass through the tungsten target; therefore, special precautions were taken to decrease radio emission that could be due to these electrons inside the chamber. To measure the radio emission, special antenna receivers with the frequency bands C (3.4–4.2 GHz), Ku (10.7–11.8 GHz), and Ka (20.2–21.2 GHz) were placed inside the chamber. Figure 7a schematically presents the general view and location of units of the AWA (Argonne Wakefield Accelerator). A similar scheme of an experiment at SLAC (Stanford Linear Accelerator Center) is shown in Fig. 7b.

The photons in the AWA experiment typically spent an energy of about 1 PeV to ionize air in the chamber. Because the radiation length of electrons in air is about 300 m at sea level, the total expenditure amounts to

$$W_{\text{chamber}} \sim \frac{1}{300}\left(1-\frac{1}{\mathrm{e}}\right)(5\times10^{17})\ \text{eV} \approx 10^{15}\ \text{eV}\,.$$

The mean energy per ionization (with account for elastic collisions and excitation losses) is about 30 eV. This implies that about 3×10^{13} electrons are produced in the chamber by one pulse. Clearly, the electron density in this case is much larger than in an atmospheric shower with an energy of about 1 PeV. The highest plasma density is in the central cylindrical area about 25 cm in radius, and the mean density in the chamber is about 10^8 cm^{-3}.

The molecular bremsstrahlung radiation mechanism predicts that the observed radio emission is incoherent, with the intensity linearly proportional to the current in the pulse. The first observations showed that the radio emission is partially coherent, with the coherent component intensity proportional to the square of the beam current. Therefore, a method of analysis was developed based on the fact that the coherent component can be subtracted from the total emission. To separate the two different emission components, the electron beam was converted into photons using radiators of different thicknesses (2 and 5 mm). The authors of [62] argue that this could change the relative contribution of the two components. However, later measurements did not reveal any difference.

The results of radio emission measurements in the AWA experiment in the 20 GHz frequency band with a 5 mm radiator are presented in [62]. The result of the subtraction of noncoherent emission is also shown. Each time the beam entered the chamber, a clear increase in the level of the signal over noise was observed; however, a significant signal was also detected when the beam was blocked by a lead obstacle immediately before the setup. Attempts to eliminate the unwanted signal failed, and further studies were conducted at SLAC.

2.6.2 SLAC experiments. In 2004, an experiment similar to the AWA one was carried out at SLAC. The scheme of the SLAC experiment was essentially the same as that of the AWA experiment, but additional precautionary measures were taken to reduce radio interference. The SLAC experiment used the same method to calibrate the HiRes fluorescent detector [64]. At SLAC, a well-controlled beam of electrons with an energy of 28 GeV was generated, which was collided with a target consisting of 90% aluminum oxide (Al_2O_3) and 10% silicone dioxide (SiO_2). To measure the number of particles in the shower, the radiator length was chosen in the range 0–14 radiation lengths. In this experiment, an electronic bunch with an energy of 28.5 GeV was used to create a shower directly, without intermediate conversion to photons. The typical bunch, containing about 2×10^7 electrons, produced a shower with a total energy of around 6×10^{17} eV.

The measurements of 1.5–6 GHz radio emission by an antenna polarized along the shower axis were reported in [62]. The measurements in terms of the mean square of the field strength were started from the moment the beam entered the Faraday chamber. The time of flight of electrons across the chamber is 3.3 ns. A strong radio pulse detected during the first 10 ns corresponds to the time of the bunch entering the chamber. This pulse turns out to be strongly polarized, with the polarization plane passing through the shower axis and the Poynting vector, i.e., the characteristic directions of transitional and Cherenkov radiation. This emission was expected, and therefore advance measures were undertaken to extinguish it almost immediately by a microwave absorber covering the internal walls of the Faraday chamber. The noise level at this stage exceeds the digitalization noise, and the sensitivity was decreased by one order of magnitude to enable detection of the powerful pulse at the beginning of the oscillogram.

An antenna polarized normally to the beam axis was also used in this experiment. Such a polarized antenna is insensitive to the relativistic emission from the shower. In this case, the powerful initial pulse must be strongly suppressed; however, it turned out that the leading edge of the oscillogram suggests an energy loss (20 dB) from the wave with another polarization. The exponentially decaying 'tail' of the radio emission extended to 60 ps or more, and here the level of interference was determined by thermal noise and not by radio interference due to the electronic hardware.

The authors of [62] believe that the radio emission observed in the SLAC experiment is partially coherent, as is suggested by data showing that the total energy of the emission energy 15–30 ns after the main pulse depends quadratically on the number of electrons in the bunch. Apparently, the coherent radio emission is three orders of magnitude higher than the expected noncoherent emission level. This suggests [62] that a subgroup of $10^3 - 10^{3.5}$ electrons radiates quasi-coherently. Taking into account that the showers in SLAC produce 3×10^{13} ionization electrons in the Faraday chamber, the fraction of the correlated emission is only $\sim 10^{-10}$, and this level of partial coherence is very far from the total spatial coherence in Cherenkov and transitional radiation. The Debye radius in the plasma at the temperature $T_{\rm e} \approx 10^{4.5}$ K in this experiment is about 2 mm; therefore, at the initial stage of the shower, there are 10^7 free electrons inside the Debye sphere. Thus, the weak correlation ($\sim 0.01\%$) inside the Debye sphere seems to be quite sufficient to observe the partial coherence effect. However, this analysis ignores the rapid change in the Debye sphere radius due to the rapid cooling of electrons. At the external medium temperature $T_{\rm e} = 10^3$ K, the Debye radius is $\lambda_{\rm D} \approx 0.3$ mm, and the Debye sphere volume contains 10^5 electrons, which corresponds to a correlation coefficient as small as 1%. In this connection, the authors of [62] note that any simple model predictions require the electron cooling dynamics to be taken into account.

An analysis of the similarity of the emission characteristics showed that the partially coherent emission observed in the SLAC experiment can be linearly scaled to the shower energy (as should be expected in the absence of coherence). Then the detection threshold at a distance of 10 km in the AMBER experiment (see Section 2.6.3) is about 8×10^{18} eV. If the scaling is quadratic in energy, the threshold is lower, 1.6×10^{18} eV. For showers with an energy near the GZK cutoff (5×10^{19} eV), the threshold distance is 20 km for linear scaling and 200 km for quadratic scaling. In the above estimates, the curvature of Earth's surface and atmospheric extinction were ignored.

The authors of [62] conclude that observations of MBR will enable all-day observations under suitable weather conditions. The EAS detection using MBR is as promising as the optical fluorescence detection method related to excitations of nitrogen molecules by fast particles. However, observations of MBR from air showers can be carried out 24 hours a day; in addition, the extinction in the microwave ranges 3.7–4.2 GHz and 10.7–12.7 GHz by atmospheric aerosols or clouds is virtually absent. Even a heavy rain reduces the radio intensity by less than 1 dB for observations of showers tilted to the horizon by 30°.

2.6.3 AMBER air shower experiment. The significant increase in the minimal value of the microwave emission from air showers compared with the expected values stimulated the development of a prototype of a device that could be used to detect high-energy cosmic particles. The prototype includes the computer and data acquisition system RaBID (Radio Bremsstrahlung Impulse Detector). The detector, including the RaBID prototype, which is referred to below as AMBER (Air shower Microwave Bremsstrahlung Experimental Radiometer), was constructed on the roof of the main building of the University of Hawaii (Honolulu) and started operating in 2005 [62].

The AMBER detector includes a two-band (C and Ku) antenna array with double polarization, located at a distance of 1.8 m from the center of a parabolic 'dish'. The array has a diamond-like shape, such that feed elements are separated by $\approx 5.2°$. The signals from each feed element come out via four channels. They are then amplified and converted to lower frequencies in a low-noise block downconverter (LNB) and are directed to the RaBID module via a coaxial cable.

The data taking started in the middle of 2005 and continued for eight months. In a significant patch of data obtained under good weather conditions, radio pulses from air showers were searched for. A shortcoming of the AMBER experiment was the absence of a surface particle detector for air shower identification. This required modifying the experiment, and the AMBER radiometer was later combined with other detectors.

2.6.4 Study of microwave emission in model experiment MAYBE (Microwave Air Yield Beam Experiment). The results of measurements of microwave radiation from air plasma produced by an electron beam at the Van de Graaf electron accelerator of the Argonne National Laboratory are presented in [65]. The energy of electrons in this beam was below 3 MeV. The authors assume that coherent Cherenkov radiation (i.e., the main background in previous experiment [62]) is now absent, which facilitates data analysis. In other words, the relative velocity of electrons $\beta = v/c$ turns out to be too low at such energies and does not satisfy the Cherenkov resonance condition $1 - \beta n \cos\theta = 0$. Radio emission was studied in a wide frequency range from 3 to 12 GHz. The duration of the electron pulse could vary from 5 ns to 1 ms. The flux of electrons and the rate of bunch generation were adjusted such that each bunch contained $10^{10} - 10^{13}$ electrons. The beam transverse size was less than ≈ 5 mm, and the thickness of the duralumin output window at the end of the ray tube was 0.002 inches. In the output window of the ray tube, a receiver coil was placed to measure the pulse current.

The ray came into a copper echo-free Faraday chamber with a volume of 1 m^3 filled with air. The internal surface of the chamber was covered with pyramidal absorbers that provided 30 dB suppression for the normal wave incidence at frequencies above 1 GHz. The electron beam entered the chamber through a hole 3 cm in diameter. The transitional radiation caused by the duralumin output window and the input window of the chamber could have been a possible source of noise, which was taken into account.

Three different radio receivers for microwave emission in a wide frequency range were placed in the chamber. The first receiver, operating in the C band (3.4–4.2 GHz), and the second receiver, tuned to the Ku band (12.2–12.7 GHz), were calibrated in advance. A third receiver was equipped with a long-periodic antenna with the frequency range 0.85–26.5 GHz. All the antennas were placed at the same distance (0.5 m) from the electron beam in the plane perpendicular to its direction. To control the external radiation, additional radio detectors with the C- and Ku-band and a low-frequency radio receiver (0.7–2.4 GHz) were installed outside the chamber near the beam exit. Signals from all antennas were directed to the control center via a 14 m coaxial cable.

One of the goals of this experiment was to find the dependence of the radio signal power on the electron beam power, i.e., on the number of electrons in the beam. For this, the current in the beam varied from ≈ 5 μA to 30 μA (this corresponds to the charge variation from 0.5 to 3 μC per pulse). The results for both the C band and logoperiodic antennas placed in the chamber were averaged over a group of 100 tracks for two polarization modes. The preliminary results pointed to the linear direction of the radio power on the beam energy and a difference in polarizations of $\approx 30\%$ for the C band and $\approx 60\%$ for low-frequency bands. This difference, according to [65], could be due to the presence of either other processes with other polarization degrees or near-field effects (the distance from the antennas to the beam is comparable to the emission region size).

To understand the origin of the detected radio emission, another test was performed in which the entrance port was covered with thin aluminum foil to block possible outside radiation. No significant decrease in the beam energy due to the additional layer occurred and no significant changes in the results were obtained. This lends more credence to the origin of the detected radio signal inside the chamber.

This conclusion differs fundamentally from the previous results that the radio power depends quadratically on the number of electrons. The obtained result in fact means that there is no coherence in this experiment.

2.6.5 First results of the CROME experiment. The CROME (Cosmic-Ray Observation via Microwave Emission) experiment was carried out to detect the UHF signal due to molecular bremsstrahlung in air showers [66]. Essentially, the CROME experiment continues earlier studies (for example, [62]) at a higher level. The sensitivity increase was first of all due to additional use of the KASCADE-Grande particle detector for identification of events. The 12 scintillator detectors at the core of KASCADE-Grande provided the trigger for radio detectors several hundred times per day. The region inside the detector allowing air shower reconstruction, i.e., the determination of the energy, axis direction, and, possibly, other parameters, had an area of 2×10^5 m^2.

Four antennas were used for radio detection. One of them was a dish 2.3 m in diameter for the 1–1.8 GHz band, two antennas were dishes 3.4 m in diameter for the 3.4–4.2 GHz band, and the fourth antenna was a dish 0.9 m in diameter for the 10.7–11.7 GHz band. Basically, these were narrow-beam antennas; for example, the 3.4–4.2 GHz dish had a beam of 1.6°. A low-noise amplifier and downconverter were placed in the focus.

To measure the signal envelop, the detector response time was set to 4 ns. All channels recorded information in a 10 μs time interval before and after the trigger from KASCADE-Grande. Special attention was given to the synchronization time of CROME and KASCADE-Grande, because the duration of a radio pulse from vertical showers is expected to be less than 20 ns.

KASCADE-Grande measures air showers with energies in the range $10^{15.5} - 10^{18}$ eV, including the energy 3.4×10^{17} eV at which accelerator-based experiments [62] were carried out. The mean event rate was one shower with an energy above 10^{17} eV per day [67].

The antennas have no astronomical platform and are kept immobile. Therefore, a flying radio source was manufactured to measure antenna sensitivity and beaming. A radio emitter was installed on a remote helicopter equipped with a GPS block. A two-element Yagi antenna with a one-side main lobe (corresponding to the amplification ≈ 4.1 dB) and high forward–backward attenuation to avoid reflection from the helicopter (-10 dB) was used as an emitter. The maximal power of the emitter was 6 mW in the frequency range 2970–3950 MHz. Six working modes with different modulation characteristics can be triggered by an external or internal source with a frequency of 3 Hz. In this way, the preliminary results on the intermediate zone (between the near and far emission zones) in the CROME detector were obtained.

The CROME experiment started data taking in September 2010. The initial configuration of the C band was extended from one antenna with four receivers to two antennas with 18 receivers. The second antenna was installed in April 2011. In addition to the installation of new receivers and electronics, several important additions in the measurement process were made, in particular, a bandpass filter was installed to suppress signals from airplane radio locators.

In 170 days, 79 showers with energies above 5×10^{16} eV were recorded and analyzed. Each of them was detected by at least one radio receiver in the C band. One of the showers had an energy of 7.9×10^{17} eV, a zenith angle of 10.5°, and a distance between the axis and antenna equal to 159 m. The authors of [66] state that the experiment was successful and should be continued.

2.6.6 Observations of polarized microwave emission in the CROME experiment. Papers [68, 69] (which, in fact, are a continuation of [67]) report the first direct measurement of the main characteristics of microwave emission from EAS. The synchronization of signals from microwave antennas in the CROME experiment was provided by KASCADE-Grande.

All events that can be reconstructed with KASCADE-Grande were analyzed. Among these, showers were selected that intersect the field of view of at least one CROME detector (about 5.5 showers with energies above 3×10^{16} eV per day), for which a cone of half-width 2° was allowed. The assumed time of arrival of the UHF signal from each shower was calculated based on geometrical reconstruction of the shower, taking the dependence of the refractive index on the height into account. The typical uncertainty of the time of arrival of the signal was about 50 ns. The radio noises field strength in the calculated time window relative to the mean noise level was measured every 20 μs.

Thirty-five showers with UHF signals with an amplitude above 8 dB (higher than the mean noise level) and energy above 3×10^{16} eV were selected. Two of them produced radio signals above the threshold in two microwave detectors during the expected time. The number of random radio pulses with amplitudes above 8 dB was estimated to be 7.1 ± 1.6.

The mean duration of the microwave signals was 10 ns. The shower geometry and the field of view of the corresponding receivers suggested that most of the signals were produced at heights close to the shower maximum location (typically, 4 km above the ground).

The most important implication of these experiments is as follows. The spatial and angular distributions of the microwave signals are close to the characteristic parameters of Cherenkov radiation. The obtained information is inconsistent with the hypothesis that the signals are nonpolarized at the 5σ level. A comparison with the results of CoREAS modeling showed that the obtained data are in good qualitative accord with the widening of the frequency range of known radio emission processes from several MHz to the GHz range due to time squeezing of the signal. The authors of [68] concluded that coherent emission processes dominate near the shower maximum.

From May 2011 until January 2012, 12 events recorded in the CROME experiment coincided with the time of arrival of air showers as measured from KASCADE-Grande data [69]. The duration of radio pulses was less than several nanoseconds. Typically, the radio signal from a shower was detected in only one channel. The authors of [69] argue that this excludes most radio interference outside the setup. All 12 events have common properties:

— the signal duration is less than 10 ns;

— the registration energy threshold is $10^{16.5}$ eV;

— the angle between the reconstructed shower axis and the optical axis of the antennas is very small for all showers;

— the distance between the shower axis and the antenna is 80–150 m;

— there are events with arbitrary polarization angles relative to the east–west direction. No preferential polarization direction was found.

The obtained data allowed the authors of [69] to conclude that possible radio emission mechanisms include:

(1) coherent emission due to a time-variable charge excess in the shower;

(2) noncoherent emission of separate charged particles in the shower;

(3) coherent emission caused by the transverse current of electrons and positrons in Earth's magnetic field;

(4) molecular bremsstrahlung emission;

(5) radio waves from external sources reflected from the shower.

2.6.7 Study of microwave emission in the MIDAS experiment. The initial stage of studies in the MIDAS (Microwave Detection of Air Showers) experiment is discussed in paper [70], related to searches for radiation mechanisms at ultrahigh frequencies. To detect UHF pulses from air showers, a parabolic reflector 4.5 m in diameter equipped with a 53-pixel low-noise C-detector (3.4–4.2 GHz) has been installed at the University of Chicago. The field of view of the setup is about $20° - 10°$; the mean noise temperature is 60 K. Each signal from a pixel passes through a bandpass filter cutting most of the anthropogenic noise and is then digitized. The sensitivity of the MIDAS detector was estimated using Monte Carlo simulations with all antenna characteristics taken into account. The electromagnetic energy density was parameterized as [63]

$$I_{\mathrm{f}} = I_{\mathrm{f,\,ref}}\,\frac{\rho}{\rho_0}\left(\frac{d}{R}\right)^2\left(\frac{N}{N_{\mathrm{ref}}}\right)^{\alpha},$$

where $I_{\mathrm{f,\,ref}}$ is the flux density at the distance $d = 0.5$ m from the shower with the energy $E_{\mathrm{ref}} = 3.36 \times 10^{17}$ eV, R is the distance between the detector and the air shower segment, ρ/ρ_0 is the relative density of the atmosphere at the height of the shower segment (above the sea level), N is the number of particles in the shower, and N_{ref} is the mean number of particles at the shower maximum for a proton with the initial energy E_{ref}.

The values N and N_{ref} are given in [71]. The parameter α characterizes the phenomenological coherence of the microwave emission from air showers. This parameter has not so far been determined and can take values from $\alpha = 1$ (noncoherent emission) to $\alpha = 2$ (fully coherent emission). For the assumed spectral energy density of fully coherent radio emission $I^0_{\mathrm{f,\,ref}} = 1.85 \times 10^{-15}$ W m^{-2} Hz^{-1} at the shower maximum (i.e., for $\alpha = 2$), laboratory measurements [63] show that the MIDAS detector should be able to discover several very clear events per month (see [72] for a more detailed discussion of the detection of UHF emission by this method).

The MIDAS detector operated for several months in 2011 with different anthropogenic noise levels. To eliminate spurious noise events, events triggered at a rate of less than 0.7 per day were selected. The data sample contained 1.1×10^6 events collected during 61 days of 'real-time' observations. Only ≈ 1600 events were classified as possible noise events, which suggests that real radio signals dominate over anthropogenic noise.

Despite careful searches, no candidates associated with air showers have been found. Only upper bounds on UHF fluxes and the degree of coherence of the microwave signals from air showers were obtained. Notably, the authors of [70] fully rule out the quadratic dependence of the signal amplitude on energy reported earlier in [62].

The conclusion in [70] is that the absence of evidence of the quadratic dependence of the signal amplitude on the shower energy suggests a higher energy threshold for microwave emission (or the need for a larger antenna area) than previously thought. It was also noted that the established upper bounds relate to any isotropic microwave emission mechanism that is able to produce a detectable radio flux at large distances, as in the case of fluorescent detection of air showers.

2.6.8 Study of UHF emission from air showers by the Pierre Auger Observatory. Presently, the Pierre Auger Observatory is known to be the biggest detector of UHECRs. Most events are registered by surface detectors installed across an area of 3×10^3 km^2. Additionally, the observatory is equipped with fluorescent detectors that register optical emission from excited nitrogen atoms during shower propagation in Earth's atmosphere. The simultaneous registration by the two types of detectors is extremely important in order to obtain as complete characteristics of cosmic particles as possible. However, the fluorescent detectors can operate only on moonless and cloudless nights, and therefore the efficiency of its work is about 10%. This fact stimulated the installation of additional detectors at the Pierre Auger Observatory, in particular, radiometers in the megahertz range.

In recent years, several detections of UHF emission from air showers have been reported, which stimulated the program of cosmic ray studies by the radio method [73, 74]. Three different experiments will be carried out at the Pierre Auger Observatory aimed at simultaneous registration of radio emission from showers detected by surface and/or fluorescent detectors.

Two of these experiments, AMBER (see Section 2.6.3) and EASIER (Extensive Air Shower Identification using Electron Radiometer), are already running and work in coincidence with the surface Auger detector. The MIDAS detector (see Section 2.6.7), which operated in Chicago for several months, was later moved to the Malargue region (part of the Pierre Auger Observatory [73]). AMBER and MIDAS are part of a future complex detector for remote observations of the longitudinal development of air showers.

AMBER should operate jointly with a surface detector, while MIDAS will be triggered by a fluorescent detector. The EASIER experiment should add to the surface detector measurements. The EASIER units are mounted into water tanks of the Auger installation as auxiliary radiometers integrated into the electronics and data acquisition systems of the tanks. All experiments work in the C-band between 3.4 and 4.2 GHz, reserved for satellite TV broadcasting.

The AMBER radio telescope consists of a parabolic mirror 2.5 m in diameter that reflects a sky area of $7^\circ \times 7^\circ$ into a chamber consisting of 16 pixels. Four central pixels include double-polarized feed horns for the C and Ku bands (10.9–14.5 GHz), and 12 external pixels (i.e., surrounding the inner ones) are single-polarized feed horns for the C band.

To calibrate AMBER, the feeders were immersed into a bath with liquid nitrogen. The antenna contribution to the noise temperature was measured by a calibrated low-noise unit. The combined noise temperature of the system in the C band varies from 45 K for external pixels to 65 K for internal ones. AMBER is placed near a fluorescent telescope for studies of strongly tilted air showers with high energy. The AMBER radio telescope started operations in 2011. Since then, several scans of the Sun and Crab nebula have been performed to calibrate the system.

The EASIER installation is an alternative project of a radio telescope, complementary to Auger and MIDAS. Each tank of the surface Auger detector is equipped with a radio receiver with a wide field of view (about 60°). The antenna receivers of EASIER have a small effective area of about 3×10^{-3} m^2. However, their small area is compensated by the closeness to the shower (about 1 km, in contrast to 5 or 10 km in the case of telescopes) and the shortening of the time of arrival of signals from the shower seen at a small angle to its axis (this relativistic effect can enhance the signal by an order of magnitude). The tanks are equipped with low-noise blocks mounted at the top of a 3 m mast and directed toward the zenith. To widen the working frequencies, the megahertz antennas are constructed from thick active dipoles (as in the CODALEMA detector), and additional bandpass filters narrow the working frequency band to 30–70 MHz.

In the first stage, the EASIER project consisted of seven tanks (a central tank surrounded by other tanks at hexagon vertexes) installed in April 2011. This single measurement hexagon obtained the first confirmation of UHF emission from air showers. To improve the statistics, 54 additional tanks were installed in April 2012. This setup is expected to detect about one event per month.

MIDAS was designed as a prototype of the fluorescent radiometer (radio-FD), i.e., as a radio telescope capable of observing the transverse profile of a shower and can be triggered by gigahertz emission from EASs. The first version of the MIDAS detector, which was installed at the University of Chicago, consisted of a 4.5 m parabolic antenna and 53-channel cameras.

It is expected that MIDAS will resume operation at the Pierre Auger Observatory with a 5 m parabolic dish placed near the fluorescent detector at Los Leones.

FDWave (Fluorescence Detector Wave system) is a project involving a microwave radio telescope that will have many advantages compared with other infrastructures at the Pierre Auger Observatory. The integration of the microwave detectors with the Auger particle detector will be performed by deploying 264 UHF antennas at the fluorescent detector at Los Leones instead of light sensitive pixels.

For this, the optics of the fluorescent detector were carefully studied and then used as UHF antennas. Spherical mirrors (with the curvature radius ≈ 3.4 m) of the Los Leones station, made of aluminum, easily reflect electromagnetic waves. The spherical focal surface has the curvature radius ≈ 1.7 m. The detectors are placed in holes in the aluminum chamber body. The chamber geometry sets a lower detection frequency of 9 GHz. This minimal frequency is very close to the Ku-band.

Generally, the amplification of the telescope is ≈ 44 dBi and the effective area of the dish is about 1.35 m^2. A telescope with such parameters should be able to confirm microwave emission with a quadratic dependence on the amplitude from air showers with energies above 3 EeV.

2.6.9 Experimental study of microwave emission due to a 95 keV electron beam passing through air. The accuracy of measurements of UHF emission from high-energy particle beams is limited by spurious emission due to the electron beam interaction with the installation parts, leading, for example, to Cherenkov or transition radiation when the beam passes through parts of the construction or through the air inside it.

The authors of [75] studied microwave emission caused by a low-energy electron beam (95 keV). At this energy, Cherenkov radiation can occur only in a medium with the refractive index $n \gtrsim 2$. The low emission intensity was the main shortcoming of the experiment, but this defect was compensated by the multiple storage of the signal. To obtain a high enough signal-to-noise ratio, at least 10^4 pulses must be averaged. The sensitivity of the experiment was about 10^{-16} W.

Observations were done in the Ku band (10.95–11.7 GHz) using the experimental setup shown schematically in Fig. 8. The electrostatic gun accelerated electrons to a kinetic energy of 95 keV in a 150 μs pulse. Electrons came out of the gun into the air through a diamond window 20 μm thick. The number of electrons in the pulse was controlled by changing the current using a loopback outside the electron gun. The chamber the electron beam passed through was covered with an absorber from inside to avoid the appearance of echo. The radio signal was received by a horn with an amplification of 20 dB. A low-noise block (LNB) and generator of 10 GHz electric oscillations were incorporated into the antenna. The generator was used to calibrate the whole receive path. To construct the emission beam, the horn could move such that in any position, the direction of the main lobe of the beam passed through the center of the output window of the electron gun.

The aim of the study was to determine the dependence of the microwave emission intensity on the number of electrons in the pulse, i.e., in fact, on the current strength. A strictly linear dependence means that the emission due to stopping of electrons in collisions with neutral atoms is noncoherent. A quadratic dependence means coherent emission.

To verify that the UHF emission is indeed due to electron–atom collisions, air was removed from a cylindrical vessel

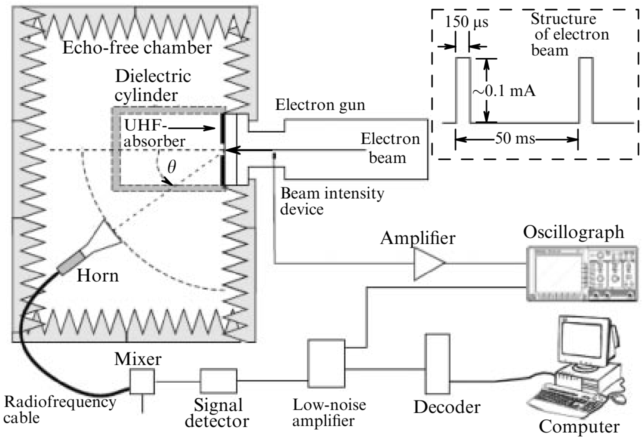

Figure 8. Schematic of the experimental setup. In the top right corner is shown the time structure of the electron beam. The beam intensity device controls the number of particles in the pulse. Air can be pumped off from the cylindrical vessel. The horn moves along a circle such that the main beam lobe passes through the diamond window of an electron gun.

(shown in Fig. 8 as a dielectric cylinder). Then the signal from the antenna disappeared. The same effect was induced by installing a thick wall behind the electron gun output.

The results of the experiment showed that the emission intensity depends linearly on the electric current in the beam, i.e., the emission is noncoherent. The use of antennas with different polarizations established that the emission is nonpolarized and is directed along the velocity and the beam axis.

Numerical Monte Carlo simulations of high-energy electromagnetic showers showed that the fraction of energy emitted (in the considered frequency range) is 0.9×10^{-13} times the shower energy. The main lobe of the emission beam, which is directed along the velocity vector of electrons, becomes very narrow at high energies. For example, for a shower energy of 1 GeV, most of the emission is contained within an angle of 10° relative to the trajectory. According to the same calculations, a shower with an energy of 5×10^{18} eV radiates $\varepsilon_{\rm MW} = 7 \times 10^{-14}$ J, and if the radio emission is detected by a 10 m antenna, the signal-to-noise ratio equal to 10 is achieved for the noise temperature $T \leqslant 1$ K. In real systems, the noise temperature is about two orders of magnitude as high, and this can be the main reason why all attempts to detect UHF emission from EASs have failed so far.

2.7 Tunka-Rex experiment

Studies of air showers in the Tunka valley were started as early as 1993, and already by 1995, using the unique optical hybrid Quasar-370 photodetectors, the first interesting results on the cosmic ray spectrum were obtained.

The Tunka-133 array, put into operation in 2009, presently consists of 175 detectors placed across an area of 3 km^2. This is the world's largest air shower array dedicated to the study of the spectrum and composition of cosmic rays with energies in the range $10^{16} - 10^{18}$ eV.

The studies carried out at the Tunka-133 array have been so successful that the decision was taken in 2012 to upgrade it into a much larger Tunka–HiSCORE installation (HiSCORE — Hundred Square km Cosmic Origin Explorer). This will be a very sensitive experiment (with a low energy threshold) with a high angular resolution of the primary particle direction, which will enable separating gamma quanta from charged cosmic-ray particles. The first stage of the installation (2014) includes 25 detectors in a 1 km^2 area. By 2016, when the experiment should start fully operating, the number of detectors will be increased to 100 across an area of more than 10 km^2. Later, the total area of the experiment is to be increased to 100 km^2.

The upgrade and operation of the Tunka-133 and Tunka–HiSCORE experiments have been conducted with the participation of the Skobeltsyn Institute of Nuclear Physics of Lomonosov Moscow State University (MSU), the Institute of Applied Physics of Irkutsk State University, the Institute for Nuclear Research (RAS), the Pushkov Institute of Terrestrial Magnetism, the Ionosphere, and Radio Wave Propagation of RAS, and the Sternberg Astronomical Institute of MSU, as well as the Karlsruhe Institute of Technology, the Research Center of Particle Physics (DESY) (Germany), the Avogadro Institute of General Physics of the University of Turin, the National Institute of Nuclear Physics (INFN) (Italy), and the University of Kansas (USA).

The electronic system of data acquisition of Tunka-133 records signals simultaneously from 25 Tunka-Rex antennas deployed by the Karlsruhe group. The Tunka-Rex array studies different characteristics of radio emission from air showers. These results will later be used to construct a record giant installation for cosmic ray studies.

Tunka-Rex with 20 antennas started operating in the fall of 2012, and radio pulses definitely associated with air showers were registered in a relatively short time [76].

The main goal of the Tunka-Rex experiment is the accurate determination of the air shower energy and its maximum depth $X_{\max}$. To achieve this goal, the Tunka-Rex array was deployed in the area where the Tunka-133 photomultipliers that measure the Cherenkov emission from air showers are located. The two detectors run simultaneously, which allows their mutual calibration. In other words, it is possible to test the accuracy of energy measurements by the radio method and the estimation of $X_{\max}$ by Tunka-Rex and to compare them with the Cherenkov detector data.

Each of the 20 antennas is placed in the center of a cluster consisting of six photomultipliers at hexagon corners. The antennas are connected by cables with a local system of digital recording at the center. The Tunka-Rex array is triggered by photomultipliers and records signal from air showers in the frequency range 30–80 MHz, outside of which radio interference is suppressed by an analog bandpass filter. This increases the signal-to-noise ratio and guarantees that the Kotelnikov theorem is not violated (the discretization frequency is ≈ 200 MHz).

Each cluster contains two mutually perpendicular antennas sensitive to two linearly independent electric field components. When the direction of the shower is known independently, such antennas enable the reconstruction of all its components. The antennas are spaced 200 m apart and represent a short aperiodic loaded loop antenna (SALLA) about 120 cm in diameter [77]. The active load of about 500 Ω increases the working passband. In the vertical plane, the antenna beam represents a lobe about 150° in width at the 3 dB level. Such an antenna has a negative amplification of about 10 dB, but the noise temperature of the system (≈ 500 K) is almost 10 times as small as the Galactic noises at 60 MHz, and the additional negative amplification of the antenna decreases the signal-to-noise ratio.

Unlike antennas used in most experiments measuring radio emission from EASs, the Tunka-Rex antennas are not oriented along the north–south or east–west directions but are turned by 45°. Because the radio signal from air showers is preferentially east–west polarized, it should be recorded in both radio channels in most cases. The change in the commonly used orientation of antennas is therefore a compromise between the efficiency and the quality of reconstruction of the radio signal near the threshold amplitude.

From October 2012 until May 2013, on dark moonless nights, only a small part of events was registered, which coincided with those registered by the Cherenkov detector and had an amplitude much exceeding the RMS level of radio interferences. These statistics are due to the strong criteria used to select radio pulses from air showers.

Generally, over the effective time of operation (392 hrs), 49 simultaneous events with zenith angles $\theta \leqslant 50°$ and 82 events with $\theta \geqslant 50°$ were selected. According to some experiments [78–82], the amplitude parameter of the side distribution is related to the primary energy. In addition, it is expected that the tilt of the cross distribution of amplitudes is sensitive to the shower maximum location [19, 83]. The optical detectors can provide a sufficiently reliable estimate of the energy and $X_{\max}$ only for showers with a small tilt; therefore, such events were used for mutual calibration of radio and Cherenkov detectors.

To test the expected sensitivity of the Tunka-Rex measurements to shower parameters, in particular, to the shower energy, the cross amplitude distribution of signals from the 49 events with $\theta \leqslant 50°$ was constructed. The distance from each antenna to the shower axis was determined by the Cherenkov detector data, and then the maximum modulus of the electric field strength was found as a function of this distance.

A careful analysis [76] suggested that the radio emission is related to the geomagnetic field. In the future, the methods for reconstructing shower parameters will be improved to allow a comparison with model calculations and the results of other experiments.

3. Physical models of radio emission from air showers

Despite the great possibilities of modern high-speed electronics and computers, it is quite difficult to measure the electromagnetic field from an EAS because of many effects accompanying its propagation in the air. This is partially due to the probabilistic character of the interaction of high-energy particles of the shower with atomic nuclei, which ultimately determines the properties of the radio emission source itself. But the huge number of particles in the shower allows statistical analysis methods to be successfully applied.

Generally, it is possible to describe the principal quantum mechanical processes in an air shower and to determine the data required to calculate a radio emission whose intensity is known to be highest near the shower maximum. However, even near the shower maximum, the electrodynamic description is as complicated as the quantum mechanical one at different stages of shower development. The reason is the great variety of radio emission mechanisms. Briefly, the following points can be noted.

(1) A high-energy electron or positron can emit Cherenkov radiation in some media. The intensity and energy spectrum of this collective process depend on the coherent emission conditions, which are in turn related to the shower geometry.

(2) An electron can generate geosynchrotron emission in Earth's magnetic field.

(3) Near the ground, there is an electric potential gradient of about 100 V m^{-1}, which can vary by an order of magnitude depending on weather conditions, and then the so-called geoelectric emission mechanism can be dominant.

(4) The energy of electrons in the shower decreases due to ionization and excitation of air molecules. The change in the electron energy can lead to bremsstrahlung radiation, which should also be taken into account as a collective plasma process (see [5] for more details about these radiation mechanisms).

In principle, it is possible to write a system of equations for the radiation field of each particle (an electron or a positron) taking all radiation mechanisms into account, and then to find the total emission from the shower. However, it is practically impossible to tackle this problem. Therefore, simplified models are often used, in which one dominating radio emission mechanism is considered and idealized shower geometry is assumed. Clearly, in the last case, the result depends on both the quality of the numerical code and the experience of the researcher. Inadequate models can easily lead to wrong results.

Two main approaches, microscopic and macroscopic, are used. In the microscopic treatment, individual radiation fields of each electron are summed. This approach is realized in the REAS [84, 85] and ZHAireS [55] computer codes. In the alternative macroscopic approach, the current density in the shower is modeled. This current is used in the Maxwell equations to describe the radiation field. This approach is realized in the MGMR [86, 87] and EVA [88] codes.

Some time ago, the microscopic and macroscopic descriptions yielded different results. Nevertheless, the authors of [89] note that after some corrections, consistency was reached (see Section 3.3 below).

3.1 Radio emission of the transverse current of an air shower in Earth's magnetic field

The radio emission from an air shower can be related to an excess of electrons due to annihilation of positrons when the shower propagates. It was found in the original papers [1, 2] that the Cherenkov radiation from these electrons can be sufficient to be detected by the simplest radio antennas. Soon after that, a theoretical study of radio emission from charged particles of the air shower was carried out [3]. A comparative analysis showed that the intensity of the geomagnetic radio emission can be significantly higher than that of the Cherenkov radiation. Subsequent experiments confirmed this conclusion.

Presently, the radio detection method of air showers is very topical and is considered complementary to traditional methods. Fifty years after the publication of paper [3], the need to obtain new results by this method is quite obvious.

Paper [90] is one of the first papers to revisit the transverse current model and delineate the main characteristics of later calculations. In [90], the cascade shower is considered not as two rings with opposite signs, as was originally assumed in [3], but as a convex disk (i.e., part of a spherical layer), which is closer to reality. Because the coherence of emission directly

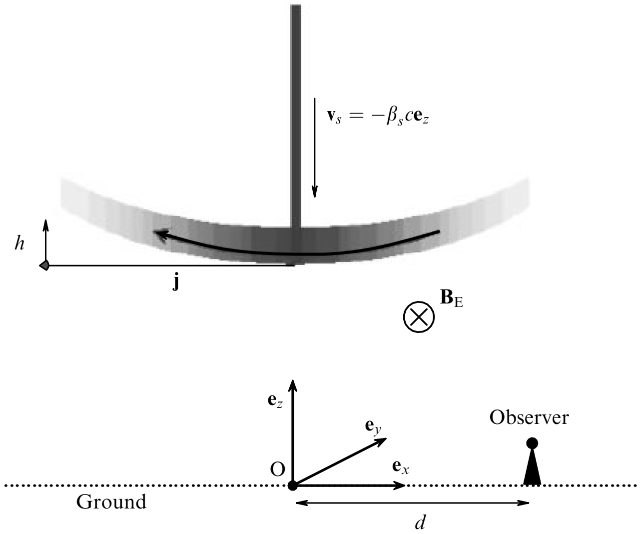

Figure 9. Main geometric relations used in [90]. The cascade disk is shown as a shaded segment. The depth h is counted from the disk front moving vertically with velocity $\mathbf{v}_s = -\boldsymbol{\beta}_s c$, $\boldsymbol{\beta}_s = \mathbf{v}_s/c$ is the relative velocity. The observer is located at distance d from the coordinate origin centered on the ground.

depends on the geometry of the shower, the model in [90] takes the transverse and cross distribution of charges in the disk into account, but ignores the disk curvature.

Figure 9 shows a disk moving vertically toward the coordinate origin at point O. Near the center, the disk is a few meters thick and moves in Earth's magnetic field with the characteristic velocity $\boldsymbol{\beta}_s = \mathbf{v}_s/c$. The Lorentz force acts on charged particles and causes their acceleration in the direction of the x axis perpendicular to the magnetic field and the shower axis. In Earth's atmosphere, electrons and positrons frequently collide with air molecules, which have relatively low transverse velocities and are distributed chaotically. The Lorentz force and collisions lead, in particular, to the drift of charged particles in the direction normal to the shower axis, i.e., to steady motion along the x axis.

We can draw an analogy with what happens to electrons in a conductor. If a potential difference is applied to the ends of a conductor, the electric field starts acting on charged particles. But this action is compensated by collisions with conductor's atoms (equivalent to the friction force) and, as a result, the constant drift velocity determines the value of the electric current. Electromagnetic emission from the shower caused by the electron drift is exactly due to such a constant transverse current moving with high velocity toward the ground. Because the number of charged particles in the shower changes relatively slowly, the form of the electromagnetic pulse is mainly determined by the drift current change in time and by time delay effects.

The radiation field as a function of time is calculated in the standard way. The density of charged particles as a function of time and coordinates is expressed as

$$\rho_e(x, y, z, t) = \int N_e f_t(t)\, \rho_{\mathrm{NKG}}(x, y)\, \rho_p(h)\, \delta(z + \beta_s ct + h)\, \mathrm{d}h\,,$$

where N_e is the maximum number of particles in the shower, ρ_{NKG} is the spatial charge distribution function, and $\rho_p(h)$ is the distribution function of particles across the disk thickness [91, 92]. Both distributions are normalized to unity, $\int \rho_{\mathrm{NKG}}(x, y)\, \mathrm{d}x\, \mathrm{d}y = 1$ and $\int \rho_p(h)\, \mathrm{d}h = 1$. The total number of particles at a time t is given by the product $N_e f_t(t)$, where $f_t(t)$ is some function normalized to unity at the maximum. The time is counted such that the moment $t = 0$ corresponds to the location of the shower at the coordinate origin $z = 0$, and the time is negative before that. The longitudinal development of the shower is parameterized via a parameter s, the so-called age of the shower, which is a function of depth [93, 94]. The presence of the δ-function means that the volume density is nonzero only at $h = -(z + \beta_s ct)$, which is convenient for subsequent transformations, because this does not require the charge density description.

To determine the current volume density $\mathbf{j}(\mathbf{r}, t) = e\mathbf{v}(\mathbf{r}, t)\, \rho(\mathbf{r}, t)$, the velocity of charges has to be specified. The velocity of charges has two components: one, $\mathbf{v}_s = c\boldsymbol{\beta}_s$, is along the vertical, and the other, the transverse component $\mathbf{v}_d$, is due to the drift of particles in Earth's magnetic field. The component $\mathbf{v}_d$ is thought to be responsible for radio emission [90]. In other words, if there is no geomagnetic field, there is no transverse velocity component, only the steady motion of the electrically neutral system of charges (here, the negative excess of electrons is ignored), which cannot radiate.

With the current density found, the vector potential can be represented in the form of retarded Liénard–Wiechert potentials. Two field sources are considered: a static dipole formed by charges that lost their energy and are at rest, and a dipole moving with the velocity $\mathbf{v}_s = c\boldsymbol{\beta}_s$. The first source produces a Coulomb field and is ignored in what follows. As in a disk moving in the magnetic field, charge separation occurs; the second source represents a dipole with changing current. The characteristic time of the current change is the time of shower development. The motion of the dipole at almost the speed of light is then accompanied by emission of a nanosecond radio pulse [95].

3.2 Model of radio emission from a collection of currents from individual electrons in an air shower

The characteristic features of the model of radio emission due to the collection of currents formed by separate electrons in EASs are presented in [96–98]. In this model, the radiation field from the air shower is found as a sum of fields created by electron–positron pairs moving along a curved trajectory in Earth's magnetic field (the so-called microscopic approach). In [98], an analytic solution of the problem within the known approximations of the shower geometry is presented and the basics of the microscopic approach are expounded.

When describing the emission field of an electron (positron) in an air shower, the authors of [98] use formulas from monograph [99], in particular, for the electric field strength $\mathbf{E}(\mathbf{r}, \omega)$ and the specific emission energy I per unit frequency and solid angle:

$$\mathbf{E}(\mathbf{r}, \omega) = \frac{\omega e}{r} \frac{2\rho}{\sqrt{3\pi}\, c^2} \left(\frac{1}{\gamma^2} + \theta^2\right) \exp\left[\mathrm{i}\left(\frac{\omega r}{c} - \frac{\pi}{2}\right)\right] \times \left(-\mathbf{e}_\parallel \mathrm{i} K_{2/3}(\xi) \pm \mathbf{e}_\perp \theta\, K_{1/3}(\xi)\right), \tag{3.1}$$

$$\frac{\partial^2 I}{\partial\omega\, \partial\Omega} = \frac{4e^2}{3\pi c^2} \left(\frac{\omega\rho}{c}\right)^2 \left(\frac{1}{\gamma^2} + \theta^2\right)^2 \times \left(K_{2/3}^2(\xi) + \frac{\theta^2}{\gamma^2 + \theta^2}\, K_{1/3}^2(\xi)\right), \tag{3.2}$$

$$\xi = \frac{\omega\rho}{3c} \left(\frac{1}{\gamma^2} + \theta^2\right)^{3/2},$$

where ρ is the radius of the trajectory, γ is the electron Lorentz factor, θ is the angle between the direction to the observer and the velocity vector of the particle, $c = 3 \times 10^{10}$ cm s^{-1} is the speed of light in the vacuum, $e = 4.8 \times 10^{-10}$ (CGSE) is the electron charge, and $K_\nu(\xi)$ are the modified Bessel functions. The radius of the trajectory ρ of a relativistic particle with mass m moving with velocity v at an angle α to the magnetic field lines B is $\rho = v\gamma mc/(eB\sin\alpha)$.

Fields (3.1) are then added coherently, and it is assumed that for each electron there is a positron with the same energy and the initial direction of motion with a common initial point. To calculate the radiation field, the known geometrical approximations of the air shower are used: the shower age as a function of its depth, the transverse charged particle distribution (the Nishimura–Kamata–Greisen distribution), and the longitudinal development length of the shower. The distribution of particles over the time of arrival [100] is used to approximate the curvature and thickness of the shower front as a function of the radial distance to the axis. Because the radiation intensity depends on the particle trajectory curvature radius, which in turn depends on the particle energy, the particle energy distribution in the shower has to be known. This is described by the power law

$$p(\gamma) = \left(\frac{\gamma}{\gamma_1}\right)^u \left\{1 - \exp\left[-\left(\frac{\gamma}{\gamma_1}\right)^{w-u}\right]\right\},$$

where $u = 1$, $w = -2$, and $\gamma_1 = 74.2$, with the peak of the distribution corresponding to the Lorentz factor $\gamma_0 = 60$.

To add the fields, the shower trajectory is split into 16 450 m segments (radiation length at a height of 4 km). The results of many calculations of the emission field depending on the geometrical approximations used and the angle to the shower axis are presented in [98]. These include plots of the time dependence of the electric field strength in a radio pulse in the frequency range 42.5–77.5 MHz from a shower with the energy $W = 10^{17}$ eV at the ground level along the shower axis. If the maximum field strength is related to the frequency range, it is possible to approximately estimate the field strength in frequently used units: $E \approx 42$ μV MHz^{-1} m^{-1}, which is about four times as large as the experimental values [101].

In [102], the authors of [98] presented the results of Monte Carlo calculations of the field strength produced by the geomagnetic mechanism as a function of time. In [102], instead of expression (3.1) for the field from an individual charge, the classical formula for the field strength produced by an arbitrarily moving point-like charge is used with the proper time delay taken into account:

$$\mathbf{E}(\mathbf{r}, t) = e\,\frac{\mathbf{n} - \boldsymbol{\beta}}{\gamma^2(1 - \boldsymbol{\beta}\mathbf{n})^3 R^2} + \frac{e}{c}\,\frac{\mathbf{n} \times \left[(\mathbf{n} - \boldsymbol{\beta}) \times \dot{\boldsymbol{\beta}}\right]}{(1 - \boldsymbol{\beta}\mathbf{n})^3 R}, \qquad (3.3)$$

where e is the particle charge, $\boldsymbol{\beta}(\tau) = \mathbf{v}(\tau)/c$ is the relative velocity, $R(\tau)$ is the distance between the particle and the observer, $\tau = t - R(\tau)/c$ is the delayed time t, and $\mathbf{n}$ is the unit vector along $R(\tau)$. The same approximations and parameterizations were used to describe the shower geometry in [98]. The authors note in [102] that the results of Monte Carlo simulations are consistent with the theoretical spectrum and radial dependence found analytically in [98].

Notes on the microscopic model. The authors of [98] do not comment on some ambiguous points.

(1) The main working formulas (3.1) and (3.2) in [98], taken from Jackson's *Classical Electrodynamics* [99], express the field strength and energy of emission per unit frequency and unit solid angle. These expressions were derived by ignoring bremsstrahlung radiation along the trajectory segment. A charged particle is known to radiate in a finite segment even if it moves steadily and rectilinearly. This is due to the infinite acceleration of the particle at the beginning and end of the trajectory. It is easy to verify that expressions (3.1) and (3.2) tend to zero as the magnetic field vanishes.

This last points puts in question the use of formulas like (3.1) and (3.2) to calculate the radiation field. The attempt to simultaneously take different radiation mechanisms into account (see [103]) shows that for an individual electron of the shower, the bremsstrahlung radiation is as effective as the geomagnetic radiation.

Using a new method of calculations [102], the same authors found the radiation field in accordance with (3.3), which resulted in one-polar single pulses of the field strength as a function of time. Most of the dependences presented in plots in [102] have a one-polar shape, which is typical for the near-field zone, i.e., for the region where the field is essentially Coulomb. This situation apparently occurs in reality. The emission source size (the entire shower being several kilometers long) is comparable to the distance to the observer. In this respect, of interest could be the opinion of the authors of [102] about the possibility of detecting such radio pulses, because it is well known that classical radio antennas are aimed at detection in the far emission zone.

(2) To simplify the calculation of the electric field strength from air showers, the shower trajectory is split in [98] into 16 segments, each of which is 450 m in length (one avalanche unit), which is the mean free path of an electron–positron pair with the energy corresponding to the Lorentz factor $\gamma = 60$ at the height of 4 km.

Along this path, a particle collides many times with neutral air molecules, and its direction of motion can substantially deviate from the initial one. This means, in fact, that the coherence condition is violated and the total energy emitted along the length of 450 m greatly differs from the calculated value. The mean root square deviation angle along the length Δt (in radiation units, rad. u.) is [104]

$$\theta_{\mathrm{ms}} = 0.7\,\frac{W_{\mathrm{s}}}{W}\,\sqrt{\Delta t},$$

where $W_{\mathrm{s}} = 21$ MeV and W is the particle energy, which is assumed to be constant along the path. The formula for the field strength shows that the cone emission angle is about $1/\gamma$. For example, let the particle energy be 15 MeV ($\gamma = 30$). Substituting this data in the expression for the root mean square deviation, we obtain $\Delta t \approx 0.18$ avalanche units, or 83 m at the height of 4 km. In fact, this implies that after passing this distance, the emission beam deviates from that in the previous interval $\Delta t \approx 0.18$. Coherent addition of fields in this case is senseless, and the total energy emitted in a 45 m segment can significantly deviate from the one calculated in accordance with formulas (3.1)–(3.3). This fact should be taken into account when using the results in [98, 102].

3.3 Radiation field of a shower electron–positron pair in Earth's magnetic field

Before constructing the model of emission, the behavior of individual particles in real air showers should be clarified. The finite particle trajectory, collisions with neutral air molecules, and magnetic field effects should be taken into account. This is important for both microscopic and macroscopic models.

For this, the results of studies of different emission components (Cherenkov, bremsstrahlung, geomagnetic) based on analytic solutions of the equations for individual particles or pairs of particles in EASs are presented in [103]. It is important that the solution of the Maxwell equations take all three radiation mechanisms into account; restricting to only one mechanism may lead to gross errors. Because it is difficult to account for all factors analytically, several assumptions are made in [103], which we discuss in Sections 3.3.1 and 3.3.2.

3.3.1 Radiation field caused by an isolated electron. In this calculation, only ionization losses are taken into account. For relativistic particles, ionization losses weakly depend on energy and can be expressed as $-\mathrm{d}W/\mathrm{d}S = D_1$, where $\mathrm{d}S = c\,\mathrm{d}t$ is the path element, or in terms of the current value of the Lorentz factor $\gamma(t)$:

$$\gamma(t) = -Dt + \gamma_0\,, \tag{3.4}$$

where $D = D_1/(mc)$, and γ_0 is the value of $\gamma(t)$ at $t = 0$ corresponding to the initial energy.

The friction force $\mathbf{F}_{\mathrm{fr}}$, which is directed opposite to the velocity vector, is related to the ionization energy losses, i.e.,

$$-\frac{\mathrm{d}W}{\mathrm{d}S} = \frac{\mathrm{d}W}{\mathrm{d}t}\,\frac{\mathrm{d}t}{\mathrm{d}S} = \frac{N(t)}{v(t)}\,,$$

where $N(t)$ is the power and $F_{\mathrm{fr}}(t) = N(t)/v$. Therefore,

$$\mathbf{F}_{\mathrm{fr}} = -\frac{\mathrm{d}W}{\mathrm{d}S}\,\frac{\mathbf{v}}{v} = -D_1\,\frac{\mathbf{v}}{v}\,,$$

where $\mathbf{v}/v$ is the unit vector tangent to the trajectory. Finally, we obtain the equation of motion

$$\frac{\mathrm{d}\mathbf{p}}{\mathrm{d}t} = q[\mathbf{v}\times\mathbf{B}] - D_1\,\frac{\mathbf{v}}{v}\,, \qquad \mathbf{p} = m\gamma\mathbf{v}\,. \tag{3.5}$$

System of equations (3.5) has a simple analytic solution if we set $B_z = 0$ and $B_y = 0$, i.e., if we consider a shower perpendicular to the geomagnetic field lines. Then (3.5) reduces to the ordinary differential equation

$$\gamma^2\ddot{v}_z - D\gamma\dot{v}_z + \alpha^2 v_z = 0\,,$$

where $\alpha = q_{\mathrm{e}}B/m$, q_{e} is the charge of the electron, $m = 0.9\times10^{-30}$ kg is its mass, and $\gamma(t)$ is given by formula (3.4). The equation for the component v_x looks similar. The volume density of the current $\mathbf{j}(r',t)$ of a point-like charge is expressed in [103] using a δ-function:

$$\mathbf{j}(r',t) = q_{\mathrm{e}}\big(\mathbf{e}_x v_x(t) + \mathbf{e}_y v_y + \mathbf{e}_z v_z(t)\big)$$
$$\times\,\delta\big(x' - x_{\mathrm{p}}(t)\big)\,\delta\big(z' - z_{\mathrm{p}}(t)\big)\,\delta\big(y' - y_{\mathrm{p}}(t)\big)\,,$$

where $\mathbf{e}_x$, $\mathbf{e}_y$, and $\mathbf{e}_z$ are unit vectors along axes x, y, and z, and $q_{\mathrm{e}} = -1.6\times10^{-19}$ C. The vector potential induced by this current far from the source, after the corresponding transformations, takes the form

$$\mathbf{A}_{\mathrm{e}}(\mathbf{r},\omega) = \frac{\mu_0\exp(\mathrm{i}knr)q_{\mathrm{e}}}{4\pi r v_0\cos\psi}\int_{z_0}^{z_1}\big[\mathbf{e}_x v_{x\mathrm{e}}(z') + \mathbf{e}_y v_{y\mathrm{e}} + \mathbf{e}_z v_{z\mathrm{e}}(z')\big]$$
$$\times\exp\big(\mathrm{i}\omega u(z')\big)\exp\big[-\mathrm{i}kn\big(x_{\mathrm{e}}(z')\cos\theta - z'\sin\theta\big)\big]\,\mathrm{d}z'\,,$$

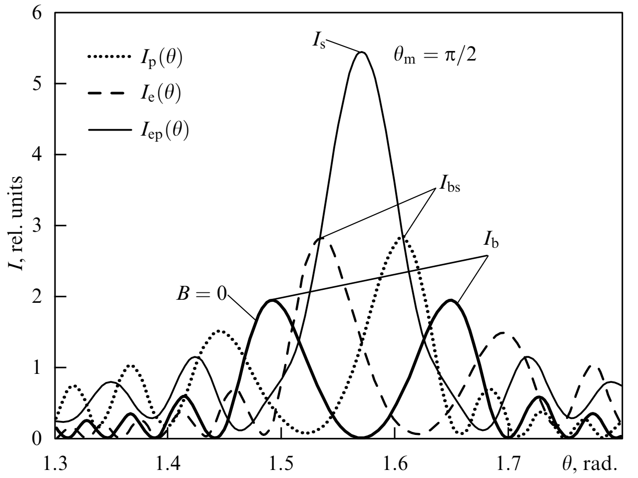

Figure 10. Intensity of radio emission in the xz plane. The dotted and dashed curves respectively show the intensity of positron and electron emission; the thin solid curve is the total emission.

where the value z_1 corresponds to the 'stopping' of the particle.

The three field components $\mathbf{B} = \operatorname{rot}\mathbf{A}$ and the energy of emission can then be found. The radiation field from the positron can be found in a similar way.

3.3.2 Resulting field from an electron–positron pair. Conclusions. To study the field $\mathbf{B}_{\mathrm{ep}}$ of an electron–positron pair, the corresponding field components from the electron and positron are added:

$$\mathbf{B}_{\mathrm{ep}} = (\mathbf{B}_{\mathrm{e}x} + \mathbf{B}_{\mathrm{p}x}) + (\mathbf{B}_{\mathrm{e}y} + \mathbf{B}_{\mathrm{p}y}) + (\mathbf{B}_{\mathrm{e}z} + \mathbf{B}_{\mathrm{p}z})\,.$$

Figure 10 shows the intensity of emission from an electron, $I_{\mathrm{e}}(\theta,k)$, and a positron $I_{\mathrm{p}}(\theta,k)$, as functions of the observation angle θ in the xz plane. The dotted and dashed curves correspond to the positron and the electron, and the solid curve shows the total intensity $I_{\mathrm{ep}}(\theta,k)$. The calculations were performed for the height $z_0 = 5$ km ($n = 1.00017$) and the initial energy corresponding to $\gamma_0 = 200$. The motion stops at $z_1 = 4248$ km. The following parameters were adopted: the geomagnetic field $B = 0.25\times10^{-4}$ T, the wavenumber $k = 1$ ($\nu\approx 50$ MHz), $D = 7.78\times10^7$ s^{-1}, and $q_{\mathrm{e}} = -q_{\mathrm{p}} = -1.6\times10^{-19}$ C.

The emission beam of one particle without a geomagnetic field is shown in Fig. 10 by the thick solid curve. This is 'purely' bremsstrahlung radiation caused by longitudinal acceleration. The intensity maxima, $I_{\mathrm{b}} = 1.94$ (relative units), are symmetric with respect to the point $\theta = \pi/2$. The curves I_{e} (dashed) and I_{p} (dotted) show the spatial distribution of the emission for the characteristic geomagnetic field $B = 0.25\times10^{-4}$ T. The corresponding maximum values are $I_{\mathrm{bs}} = 2.82$. The emission from the electron–positron pair I_{ep} for the field $B = 0.25\times10^{-4}$ T has the maximum value $I_{\mathrm{s}} = 5.41$.

The solutions obtained in [103] led to the following conclusions.

(1) It can be directly verified that the bremsstrahlung intensity from one particle with the charge $2q$ at $B = 0$ increases fourfold, as expected for the coherent addition of fields. Therefore, the field strength (in relative units) due to purely bremsstrahlung emission from one particle is $E_{\mathrm{b}1} = \sqrt{I_{\mathrm{b}}} = \sqrt{1.94} = 1.393$.

(2) For a typical geomagnetic field $B = 0.25 \times 10^{-4}$ T, the total intensity of radiation from a pair of particles, which reaches the maximum $I_s = 5.41$ at $\theta = \pi/2$, is determined entirely by the synchrotron radiation mechanism, because at $\theta = \pi/2$ the field strength from a pair of oppositely charged particles is equal to zero for the bremsstrahlung radiation mechanism (see Fig. 10). In relative units, the field strength E_s from such a pair in the geomagnetic field is proportional to $\sqrt{I_s} = \sqrt{5.41}$, i.e., one particle creates the field strength $E_{s1} = \sqrt{5.41}/2 = 1.163$.

(3) By comparing the fields of 'purely' bremsstrahlung and 'purely' synchrotron radiation, we find that $E_{s1} < E_{b1}$. In other words, under the given conditions, the bremsstrahlung mechanism is more effective than the synchrotron one, and the contribution from the bremsstrahlung radiation should be taken into account in the radio emission model.

(4) The contribution from these two radiation mechanisms should be estimated taking the total number of particles in the shower into account: the contribution from the bremsstrahlung mechanism is determined only by the excessive electrons. According to the modern calculations and measurements, the excess is $\sim 0.2N$. In experiments, the radio pulse amplitude is measured, which is proportional to the field strength. Therefore, it is interesting to estimate the relative contributions from the bremsstrahlung and synchrotron mechanisms to the total field strength of the shower. For the field strength $B = 0.25 \times 10^{-4}$ T, the intensity amplitude (for an electron or a positron), which is $I_{bs} = 2.82$ (see Fig. 10), is the sum of the bremsstrahlung and synchrotron radiation, i.e., $E_{sb1} = \sqrt{2.82} = 1.68$ (in the same units for one particle). Of course, $1.163 + 1.68 \neq 2.82$, because these values correspond to different points on the angle axis θ.

Let the number of particles in the shower be N. The field strength produced by all excessive electrons is then $E_{bs} = 0.2E_{sb1}N$, and that produced by all electron–positron pairs (which emit only synchrotron radiation) is $E_s = 0.4E_{s1}N$. It is easy to see that $E_{bs}/E_s = 0.72$, showing that the contribution from the bremsstrahlung radiation is non-negligible. Moreover, for a magnetic field two times as small, $B = 0.125 \times 10^{-4}$ T, the 'purely' synchrotron field strength decreases by two times. Therefore, if the angle between the geomagnetic field and the shower axis is less than 30°, the radio pulse amplitude is determined by the bremsstrahlung radiation from excessive electrons, and the synchrotron radiation is insignificant. Of course, the obtained estimate of the radiation contributions is very crude and is valid only in the case of full coherence. Nevertheless, it shows that different radiation mechanisms must not be neglected.

(5) A formal increase in the refractive index from $n = 0.00017$ (at the height of 5 km) to $n = 0.01$, keeping other parameters constant, has virtually no effect on the shape of the emission diagram shown in Fig. 10. This qualitatively shows that the Cherenkov component is too small in this consideration, which suggests that the Cherenkov mechanism is effective only in dense media; for example, it is of fundamental importance in the radio astronomical method [7, 9, 105].

3.4 Radar detection of air showers

The idea of the radar method of air shower detection is as follows. A nonbeamed system of radio antennas generates continuous (or pulsed) radio emission with a power of the order of 10^5 W. When an air shower is in the region where the field strength of the stationary transmitter is still high, the ionized part behind the shower reflects (re-radiates) electromagnetic waves that can be registered by one or several radio receivers. The amplitude of the received signal and its relative time delay at different antennas can be used to estimate the air shower characteristics. So far, such experiments have been rare, but theoretical studies using various models were being performed repeatedly.

Apparently, the first attempts to justify the possibility of the radar detection method were done by Blackett and Lovell [106]. They noticed a report on an anomalous scattering of radio waves in the E-layer at the height $\approx 90-100$ km and even lower by an order of magnitude. Contrary to the common wisdom that this could be a natural phenomenon (e.g., due to solar activity, aurora borealis, thunderstorms), they assumed that the scattering of radio waves emitted by radars is due to an ionized cloud produced by a high-energy cosmic particle passing through Earth's atmosphere.

To obtain quantitative estimates, the authors of [106] adopted a model in which a high-energy EAS produces a long narrow cylinder of ionized gas crossing the terrestrial atmosphere. The maximum intensity of the reflected signal is proportional to the length of the ionized trace, which forms the first Fresnel zone for radio emission with a wavelength λ: $L = \sqrt{\lambda R}$.

The simplest estimates of the electron number density in an ionized cylinder [106] suggested that the primary particle energy $E = 2 \times 10^{16}$ eV would be sufficient to produce a detectable reflected signal. However, this estimate is now thought to be too optimistic.

Attempts to construct a model that would properly describe processes occurring during the irradiation of EASs by electromagnetic pulses are being continued. For example, in [107], it is also assumed that the ionized column (track) formed after the cascade disk passage can reflect radio waves, as in the case of the burning of small meteoroids in Earth's atmosphere. Here, the densest plasma that can reflect radio waves is near the shower axis, where the number density of relativistic particles is maximal.

Plasma is characterized by the plasma frequency, i.e., the frequency of oscillations of electrons relative to ions in a homogeneous plasma without a magnetic field. Two possible states of the ionized column are discussed in [107], which are determined by the linear charge density in the column with the critical value $\alpha \approx 10^{14}$ m^{-1}.

(1) The first state corresponds to a high density in the column, which can be treated as a metal conductor. In this state, the plasma frequency exceeds the radar one, i.e., the waves from the transmitter cannot penetrate into the track (conductor) and are reflected. Depending on the wavelength, there can be two reflection regimes:

(a) the Rayleigh regime, where the radius of the conductor is much smaller than the wavelength λ, $r_c \ll \lambda$. This regime, according to [107], corresponds better to the air shower properties;

(b) the optical regime, which is realized when $r_c \gg \lambda$. (We do not consider this case here.)

(2) The second state corresponds to a low electron density in the column. In this state, the plasma frequency is below the radar one, and hence electromagnetic waves from the transmitter can penetrate into the plasma column. Here too, depending on the radar wavelength, two reflection regimes are possible:

(a) the Rayleigh regime, where the mean radius of the column is much smaller than the wavelength, $r_m \ll \lambda$. In this regime, the emission penetrates into the plasma and coherent Thomson scattering occurs. The coherence is possible because of the condition $r_m \ll \lambda$, and the scattering cross section is given by the classical Thomson formula

$$\sigma_T = \frac{8\pi}{3}\left(\frac{e^2}{m_e c^2}\right)^2 = 6.65 \times 10^{-29}\ \mathrm{m}^2 .$$

If the emission is polarized along the shower axis, the length of the first Fresnel zone (the distance along the column where the waves are added coherently) is $L_F = \sqrt{\lambda R/2}$, where R is the distance from the shower axis to the observer. Then the total cross section of the entire plasma column is $\sigma_b = N_e^2 \sigma_T$, where $N_e^2 = \alpha L_F$;

(b) the optical regime, which is realized when $r_m \gg \lambda$. If the radar frequency ν exceeds the plasma one, $\nu > \nu_p$, and $r_m > \lambda/4$, the coherence condition is violated. In this case, the correct estimate of the scattering emission intensity should take the phases of scattered waves into account.

The charge density near the shower axis is determined by the parameterization of the transverse particle distribution (the parameters are the shower age and the Moliére radius; see, e.g., [104, 108, 109]):

$$\xi_e(r) = K_N\left(\frac{r}{r_M s_M}\right)^{s-2}\left(1 + \frac{r}{r_M s_M}\right)^{s-4.5}, \qquad (3.6)$$

where

$$K_N = \frac{N_e}{2\pi r_M^2 s_M^2}\,\frac{\Gamma(4.5-s)}{\Gamma(s)\,\Gamma(4.5-2s)},$$

Γ is the gamma function, $s_M = 0.78 - 0.21$ s, and $r_M = 70(\rho_0/\rho)$ is the Moliére radius. Given the mean energy $W_{ion} \approx 30$ eV needed to excite and ionize neutral air molecules [110, 111], the total charge density, i.e., the number of electrons kicked off from neutral atoms in a given atmospheric volume by relativistic particles of the shower, can be estimated.

Such estimates [107] of the maximum of showers with energies $10^{18} - 10^{21}$ eV yield a linear electron–positron pair number density of $\sim 10^{12} - 10^{15}$ pairs per m, with most of the pairs, according to the parameterization in (3.6), contained within several meters of the shower axis.

In the models considered, it is important to estimate the rate of the plasma column destruction, which is determined by the following main processes:

(1) diffusion of electrons through the ambient air;

(2) recombination of electrons with ions;

(3) adhesion of electrons to neutral molecules.

The characteristic time constant in the first process is assumed to be $\tau_{EAS} \sim 60$ s. The recombination time is about several minutes. As is well known, the third process is the fastest one. In the normal atmosphere, the 'adhesion' time is of the order of 10^{-8} s (see, e.g., [111]). According to [107], the characteristic lifetime of an ionization electron at a height of 5 km is about 10–20 μs.

Furthermore, the energy reflected back to the transmitter from a plasma column (which is almost immobile, unlike the cascade disk) has been calculated [107]. This reflection assumes an almost isotropic scattering of the incident wave and the dependence of the reflected signal power on the distance r in the form $P_{rec} \sim 1/r^4$. It was assumed in [107] that the transmitter and receiver are identical. The reflected signal amplitude depends on the so-called radar cross section (RCS) — the ratio of the reflected signal power to the power incident on the reflector. In other words, the RCS is equivalent to the area of an ideally scattering surface. At radar frequencies below the plasma one, the ionized core of the shower is similar to a metal cylinder whose length is equal to the length of the first Fresnel zone. According to [107], the RCS for air showers attains a maximum $\sim 10^4$ m^2 at a frequency ~ 10 MHz for the incident angle of 90°. When the radar frequency is too high or the ionized electron density is too low, the amplitude of the reflected signal is determined by Thomson scattering on free electrons.

Variants of the radar system that could have characteristics comparable to those of the HiRes fluorescent detector are also discussed in [107]. The author argues that the autonomous radar system for EAS detection should include several stations, both emitting and receiving, with each station being sensitive to pulses produced by other stations. To optimize the SNR, the experiment should be carried out at the lowest frequency that can maximize the SNR with atmospheric interference in the day time. From these considerations, a frequency above 30 MHz was proposed [107]. In the high and ultra-high frequency regimes, the effective noise temperature of the system for a remote observer (far from industrial interference sources) is $T_{sys} = 2.9 \times 10^6\,(f/3\ \mathrm{MHz})^{-2.9}$ [K], which yields $T_{sys} = 3600$ K at 30 MHz.

To detect EASs with energies above 10^{19} eV within a region with a characteristic size of 20 km, in the subcritical case (i.e., where the radar frequency is above the plasma one), the RCS value should be at least ~ 2 m^2. The Fresnel length for such a shower is about 250 m at a height of 10 km, which in mass units corresponds to about 10 g cm^{-2}. The standard radar system at ultra-short waves (USWs) has a peak power of 60 kW and generates 10 μs pulses at a rate of 10–50 kHz. The brightness temperature of the sky at a frequency of 30 MHz corresponds to the system temperature $T_{sys} = 3600$ K.

Because the signal detection rate should be as high as possible, wide-beam antennas have to be used. A vertical monopole or disco-cone system [112] is appropriate, providing observations within the azimuthal angles of 2π and a declination from $\approx 5°$ to $\approx 50°$ with a full amplification of ≈ 3 dB relative to an isotropic antenna. Under these assumptions, the SNR expressed in decibel-milliwatt (dBm, decibel related to 1 mW) is 6.4, which provides a resolution of 34 m at a working frequency of 30 MHz using 10% frequency modulation (in this case, therefore, the so-called modulation depth is 3 MHz).

The frequency method of distance measurement is based on using the frequency modulation of continuously emitted signals. In this method, a frequency is emitted within a chosen time interval and is changed linearly from some value $f1$ to $f2$. The reflected signal comes back linearly modulated at the time preceding the detection time by a time delay. Hence, the frequency of the reflected signal detected by the receiver is linearly dependent on time. The time delay is determined by the sharp change in the frequency of the signal difference (between the transmitter and the receiver).

One of the results of calculations shows that the expected detection rate of air showers with the respective energy above 10^{18} eV and 10^{20} eV with the threshold SNR = 6.0 is about 10^4 and 500. Here, the transmitter power should be at least 60 kW for the frequency band of 100 kHz, the mean frequency 30 MHz, the pulse duration 10 μs, and the modulation depth 3 MHz.

3.4.1 The role of relativistic effects. An extensive air shower is an entirely relativistic phenomenon. The mean Lorentz factor for electrons in the shower is close to $\gamma = 60$, but γ is much larger near the axis. This fact was assumed in [107], but because only the immobile near-axis region 200–300 m in length with the highest electron number density was of interest, relativistic effects were ignored.

Quite a different model was presented in [113, 114], where the concept of the reflecting region as an immobile metallic cylinder (the shower core) was revised. The authors of [113, 114] found that the lifetime of thermalized electrons at sea level is ~ 10 ns, and increases to 200 ns at the height of 10 km, which is several orders of magnitude smaller than in [107]. Therefore, it is assumed in [113, 114] that the shower should be considered not as a thin long cylinder but as a relatively thin disk. The proposed model takes into account that the maximum density of ionization electrons corresponds to the shower front and then exponentially decays and virtually vanishes at a distance of 60 m behind the front. Under these conditions, according to [113, 114], the 'trace' left behind the front is quite similar to a relativistically moving disk ~ 200 m in diameter and ~ 60 m thick. In addition, the authors argue that the correct model should take the Doppler effect into account. For this, the longitudinal density distribution in such a disk is represented as a function of the argument $x + Vt$:

$$N(x+Vt) = N_0 \exp\left[-\mu\left(\frac{x}{V}+t\right)\right] \Theta(x+Vt)\,, \tag{3.7}$$

where μ is a constant characterizing the rate of plasma destruction (i.e., $\partial N/\partial t = -\mu N$), $\Theta(x+Vt)$ is the Heaviside step function, and the positive direction of the x axis is directed against the shower front motion. Relation (3.7) assumes that the time t is negative and only at $x = 0$ is the time $t = 0$. In addition, dependence (3.7) means that the electron density in an EAS is independent of x and y, i.e., is constant over the entire cascade disk surface.

To find the reflected wave amplitude, the Maxwell equations relating the fields $\mathbf{E}$ and $\mathbf{B}$ and the volume current density $\mathbf{j}$ were used together with an equation expressing Newton's second law, $\partial j_z/\partial t = Ne^2 E_z/m - (\nu_{\text{eff}} + \mu) j_z$, where ν_{eff} is the number of electron collisions with neutral molecules per unit time and N is the electron number density.

Treating the shower ionization front as a highly conducting plasma moving with a velocity close to the speed of light, the authors of [113, 114] assume that the reflection from the front should change the frequency due to the Doppler effect. The reflected wave frequency is

$$\omega_{\text{r}} = \omega_0 \gamma^2 (1 + 2\beta n \cos\theta_0 + \beta^2 n^2)\,, \tag{3.8}$$

where θ_0 is the incidence angle. This corresponds to the reflection angle $\sin\theta_{\text{r}} = \omega_0/\omega_{\text{r}}$.

After simplifying the Maxwell equations using the change of variables $x, t \to \xi, \tau$, $\xi = x + Vt$, $\tau = t$, numerical solutions were obtained using the Runge–Kutta method. As a result, the dependence of the reflection coefficient $R(\mu)$ on the parameter μ was found. It is important that at $\mu^{-1} \sim 1$ ns, $R(\mu)$ stops growing. For example, for a shower with the energy $W_0 = 10^{19}$ eV (the near-axis electron number density $N_0 = 2.4 \times 10^5$ cm^{-3}), the reflection coefficient is about 10^{-4}.

The received power was also estimated for the radar frequency of 10 MHz. It was shown that the method can be used for the radar detection of EASs. The power of the signal reflected from the EAS plasma disk was found to increase as the radar frequency decreases; for example, when decreasing the radar frequency from 10 to 1 MHz, the power must increase by four orders of magnitude. Moreover, the reflected wave frequency here should decrease from ~ 30 GHz to ~ 3 GHz, at which the noise level is significantly lower. In the long run, this will allow EAS radar detection in the middle wave and even in the long wave band.

Using the previous calculations, the same authors theoretically analyzed the radar sounding of air showers at the 1 MHz frequency [114]. It was shown that taking relativistic effects during reflection into account is more significant than the wave scattering from an immobile track, and the reflected signal power and its level against the background noise indeed strongly increase in comparison with sounding at the 10 MHz frequency.

3.4.2 Thomson scattering model. The contribution from each individual electron was calculated in [115]. For this, an expression for the reflected power well known in the radar detection of metallic objects was used:

$$P_{\text{R}} = \frac{P_{\text{T}} G_{\text{T}} G_{\text{R}} \lambda^2 \sigma}{64\pi^3 R_{\text{T}}^2 R_{\text{R}}^2}\,.$$

Here, P_{R} is the power at the receiver, P_{T} is the power of the transmitter, G_{T} and G_{R} are the amplification of the transmitter and receiver, λ is the scattered wavelength, R_{T} is the distance between the transmitter and the target, R_{R} is the distance between the target and the receiver, and σ is the RCS value as a function of the scattering angle and the characteristic target size. The ionization track is then divided into segments $\mathrm{d}s = \lambda/10$ in length. The field formed by one segment is found from the expression

$$\mathrm{d}P_{\text{R}} = \frac{k P_{\text{T}} G_{\text{T}} G_{\text{R}} \lambda^2 \sigma_{\text{e}}}{64\pi^3 R_{\text{T}}^2 R_{\text{R}}^2} \sin^2\gamma \exp\left(-\frac{t}{\tau}\right) q\,\mathrm{d}s\,, \tag{3.9}$$

where λ is the incident wavelength, q is the linear density of ionization electrons calculated as the total number of electrons in a shower layer 1 m length, τ is the lifetime of a free electron, k is the reduction coefficient due to multiple scatterings, and σ_{e} is the Thomson electron cross section; the parameter γ takes the polarization of the transmitter and the receiver into account.

For example, for a typical energy of the shower $W_0 = 10^{19}$ eV, the maximum received power is about -100 dBm. Here, the transmitter power is assumed to be 20 kW, the radar frequency is 54.1 MHz, the distance between the transmitter and receiver is 50 km, and the shower lies in the plane perpendicular to the transmitter–receiver line. The zenith angle of the shower is 30°. The transmitter and receiver antennas have the respective amplifications 14 and 6 dB relative to the isotropic antennas. The power of this signal is insignificantly higher than that of the galactic radio noises, $N_{\text{g}} = k_{\text{B}} T_{\text{sky}} B_{\text{n}}$, where k_{B} is the Boltzmann constant, T_{sky} is the sky brightness temperature at 54.1 MHz, and B_{n} is the radio receiver band. In addition, the authors of [115] assert that the observer can register the frequency change due to the Doppler effect. In this example, the frequency changes within the range 55–100 MHz as the shower propagates. The radio power from a shower with an energy of 10^{20} eV is -80 dBm, i.e., is 100 times as high.

3.4.3 Bistatic radar ranging. An ordinary radar consists of a transmitter and a receiver shared in a common antenna. Such a radar is characterized by its maximum ranging distance and the effective area [see (3.9)]. A bistatic radar consists of separately locating transmitting and receiving sites. In this case, a powerful transmitter does not interfere with the receiver and enables continuous running. Some radar schemes use broadcasting TV stations as transmitters.

In [116, 117], preparations for an experiment on radar detection of EASs are described. In the planned experiment, a bistatic radar will work in coincidence with a ground cosmic ray detector in the state of Utah. This is a very favorable site from the standpoint of anthropogenic interference. In addition, the Telescope Array, which is the largest UHECR detector in the Northern Hemisphere, is located there. Two TV radio transmitters at the carrying frequency of 54.1 MHz and power of 2 and 20 kW are assumed.

The receiver of the bistatic radar consists of several bipolar logoperiodic antennas placed near the fluorescent detectors. It is also planned to use the radar system in combination with a high-energy electron beam to imitate EASs. This will allow both testing and calibrating the receiver for known air plasma parameters and measuring the duration of the radar echo with a 40 MeV electron gun, i.e., directly measuring the lifetime of ionization electrons in the air.

Another standpoint regarding a possible bistatic radar for EAS detection is presented in [118, 119], where the possibility of detecting air showers by bistatic radar systems is studied. Of special interest is the CROME detector (see Section 2.6), which is already equipped with antennas to receive a radar signal. The CROME antennas consist of several UHF receivers in the frequency bands 1.2–1.7 GHz (L band), 3.4–4.2 GHz (extended C band), and 10.7–11.7 GHz (low Ku band). The authors of [118, 119] expect a large frequency shift of the radar signal (the maximum shift of about γ^2), and therefore the emission frequency band must be within the 1–100 MHz range, because the CROME antennas are tuned to GHz frequencies.

This necessity leads to the following conclusion. According to estimates in [118, 119], for showers with an energy of 10^{20} eV, the maximum size of the plasma region with overcritical density is only several meters. Therefore, in such a plasma, the respective decay lengths of radio waves with the frequencies $\nu_{\mathrm{p}} = 100$ MHz and $\nu_{\mathrm{p}} = 1$ MHz are 300 m and 3000 km. These wavelengths are far in excess of the characteristic size of the region occupied by overcritical plasma, and radio waves can easily penetrate into the whole disk volume of the air shower. Therefore, with the above arguments, the Thomson scattering theory must be used to calculate the radio wave reflection in this case. A precise calculation of the received signal power requires adding the contributions from individual electrons. The final result depends on the individual phase factors of scattering electrons.

Using simple arguments, the authors then come to the conclusion that there must be an up-shift in frequency due to the Doppler effect, even though the ionization electrons on which scattering occurs are almost immobile (more precisely, they have only thermal velocities).

The authors conclude that the typical ratio of the received to emitted power lies in the range $10^{-10} - 10^{-13}$, which makes bi-radar EAS detection feasible. The C band (≈ 3 GHz) is especially favorable for this purpose due to a very low noise level (< 10 K) in this frequency band. The CROME antennas supplemented with an MHz transmitter should form a bi-radar system capable of detecting air showers.

3.4.4 Model of coherent scattering of electromagnetic waves by ionization electrons of extensive air showers. The model of coherent scattering of electromagnetic waves by ionization electrons of EASs [120] assumes the presence of a powerful isotropic source of monochromatic radiation operating in the continuous or pulse regime. Relativistic particles of an EAS contained within a narrow cascade disk ionize nitrogen and oxygen atoms in the terrestrial atmosphere. Electrons that are expelled from neutral atoms and cannot ionize molecules are thermalized to the ambient medium temperature on a time scale of the order of 10^{-10} s, and during the time τ_{e} they remain free and collide chaotically with molecules until they 'adhere' to oxygen molecules.

In the field of an external source of electromagnetic radiation with a frequency $\omega_0 \gg 1/\tau_{\mathrm{e}}$, electrons undergo an systematic oscillatory motion in addition to the chaotic motion. Because the collision rate of a thermal electron with neutral molecules is about 10^{11} s^{-1} at a height of several kilometers, an electron experiences many encounters over one oscillation period, and therefore its motion is similar to drift in the electric field of an incident wave. Such a behavior is similar in many respects to the motion of free electrons in a conductor with alternating current (for example, in an antenna). Therefore, ionization electrons composing the trace of the air shower re-radiate the incident external electromagnetic waves. The length of such a 'tail' is about 30 m, and the mean number density of electrons for a shower with the energy $W_0 = 10^{19}$ eV is 2.4×10^5 m^{-3}, whence it follows that the attenuation coefficient for radio waves is so small that the plasma formed by the ionization electrons is virtually transparent at frequencies of 50–100 MHz, and effects due to absorption of the incident waves can be neglected.

To estimate the emission intensity from thermal electrons in the disk, relativistic effects are also taken into account. This is because the cascade disk propagation velocity is close to the speed of light in the vacuum. The physical processes here are very similar to those in Cherenkov radiation. In the Cherenkov radiation mechanism, a charge moving with a speed exceeding the speed of light in the medium excites neutral immobile atoms, which are in fact the source of radiation. This radiation cannot 'overtake' the charged particle, which leads to the formation of a Cherenkov radiation cone. Similarly, the air shower front propagating with a speed exceeding the speed of light in the air excites (in this case, ionizes) the ambient neutral atoms.

However, an essential feature of the radiation mechanism in this case is related to the presence of a high-frequency electromagnetic field that induces oscillations of the ionization electrons. The emission beam of such electrons is almost isotropic (for example, as in the Hertz dipole); but the radiation can add coherently in the direction of the air shower motion to produce new ionization electrons oscillating with the source frequency. The resulting field before the shower front must depend on both the external source frequency and the shower velocity. Because the latter is close to the speed of light, we should expect that the field is enhanced by the coherent addition of radio waves emitted by all ionization electrons. Because the ionization electron, like the observer, is almost at rest, there should be no Doppler effect. (See Section 3.4.5 for a more detailed discussion.)

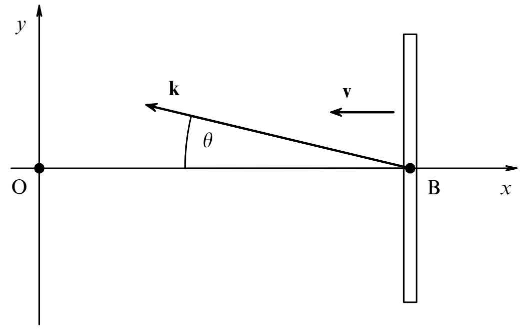

Figure 11. The propagation direction of the cascade shower and of its emission. The observer is located in the xy plane.

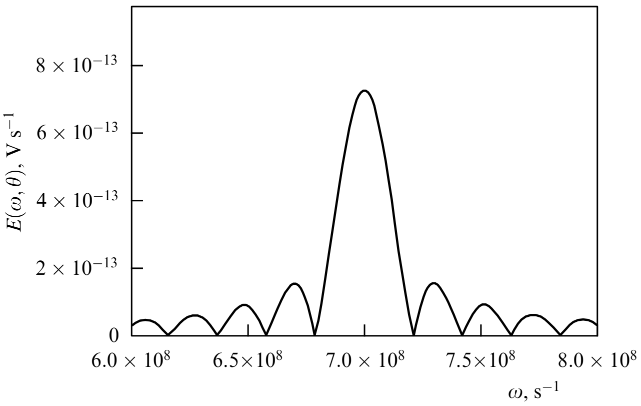

Figure 12. Emission distribution in the xy plane. The spectral width of the field strength is about 4.4 MHz. The angle $\theta = 0.01$.

The radio emission is calculated under the following assumptions.

(1) The external source of emission is so far away that its field can be treated as a plane wave in the disk region. The electric field strength $\mathbf{E}(t) = \mathbf{e}_z E_0 \cos(\omega_0 t - kx) E \mathbf{e}_z$ of the source is assumed to be normal to the shower axis.

(2) The cascade disk diameter is $b \approx 150$ m and its thickness is negligible compared to the transmitter wavelength. The charged particles of the shower are evenly distributed over the disk surface. The last assumption is far from reality, but for a wavelength comparable to the disk size, the character of the charge distribution does not affect the emission intensity and influences only the radio spectrum, making it wider than the one obtained with the real distribution. The observer is located in the xy plane, such that the angle between the x axis and the line of the observer is θ. In Fig. 11, the shower is at point B and the emission source is at point O.

(3) The cascade shower has the energy $W_0 = 10^{17}$ eV, which attains a maximum at the height of 4 km, where the pressure is 630 g cm^{-2} and the refractive index of air is $n = 1.00017$. The maximum number of charged particles in the air shower is then $N_0 \approx 6 \times 10^7$.

(4) Near the shower maximum, the atmosphere is homogeneous and the ionization losses of relativistic electrons are ~ 2 MeV g^{-1} cm^{-2}, which corresponds to $\mathrm{d}W/\mathrm{d}x = 0.18$ MeV m^{-1} at the height of 4 km. The mean energy per ionization is $w_1 = 30$ eV, i.e., $N_1 = 6 \times 10^3$ ionization electrons are formed per meter of path [121, 122].

(5) Near the shower maximum, the electric field amplitude is constant: $E_0 = \sqrt{30P}/R$ [V m^{-1}], where R is the distance to the source and P is its power.

To find the field of the scattered electromagnetic wave, it is necessary to take the strong braking of electrons due to collisions with neutral particles into account. An electron is subjected to the force $q\mathbf{E}(t)$ from the source and the 'friction' force $-m\nu_{\mathrm{eff}}\dot{z}$ [123], and therefore the equation of motion has the form

$$\ddot{z} + \nu_{\mathrm{eff}}\dot{z} = \frac{qE_0}{m} \cos(\omega_0 t - kx) .$$

One of the terms in the solution of this equation virtually vanishes in a time of the order of $10^{-11} - 10^{-10}$ s (thermalization time). The further motion of the electron is harmonic:

$$z(t) = \frac{q}{m\nu_{\mathrm{eff}}\omega_0} E_0 \sin(\omega t - kx) .$$

The radiation field is derived from the expression for the vector potential

$$A(\omega, \mathbf{r})\mathbf{e}_z = \frac{\mu_0 \exp(\mathrm{i}kr)}{4\pi r} \int_{V'} \mathbf{j}(\omega, \mathbf{r}') \exp(-\mathrm{i}n\mathbf{k}\mathbf{r}')\, \mathrm{d}V' \ [\mathrm{V\,s^2\,m^{-1}}],$$

where $\mathbf{j}(\omega, \mathbf{r}')$ is the Fourier transform of the volume density of the current of ionization electrons located in an arbitrary immobile volume element $\mathrm{d}V'$:

$$\mathbf{j}(\mathbf{r}', t) = \frac{qN_1N(x')}{b^2}\, \mathbf{v}_0 \cos\left[\omega_0\left(t - \frac{x'}{v}\right) + \varphi_0\right],$$

$$\mathbf{v}_0 = \frac{\mathbf{e}_z q}{m\nu_{\mathrm{eff}}}\, E_0 .$$

Figure 12 shows the dependence $|\mathbf{E}(\omega)|$ on the cyclic frequency ω for a shower with $W_0 = 10^{17}$ eV and the angle $\theta = 0.01$. The maximum field intensity, ≈ 5 μV m^{-1} MHz^{-1}, falls into the source frequency range $\omega_0 = (4-6) \times 10^8$ s^{-1}. The beam half width at half maximum is $\approx 2°$. The relatively high field strength is due to the coherent addition of fields from individual electrons. As follows from this calculation, the coherence of emission was not introduced by hand: it is a natural result of the solution. Such an addition of fields was due to practically identical velocities of the cascade disk and electromagnetic waves. Clearly, for the immobile source (ionization electrons) and observer, there is no Doppler effect.

The above estimates show that the field strength 4 km away from the cascade shower is about the same as that due to proper emission mechanisms. For example, in [101], the measurements of the fields from showers with energies of 10^{17} eV are presented, which are almost coincident with the above estimates. From this standpoint, the considered method offers no advantages. However, for showers with higher energies, $10^{19} - 10^{20}$ eV, the field strength increases by 2–3 orders of magnitude, which gives hope that this method of EAS detection can be used in the future.

3.4.5 Notes about the models. The models of re-radiation of radio emission by EASs in some cases invoke fundamentally different explanations of processes, leading to qualitatively and quantitatively different results. Clearly, this is first of all due to the lack of information about the shower parameters and processes accompanying shower propagation in the atmosphere. Here, several comments, especially related to papers [107, 113, 114, 120], are in order.

(1) One of the possible regimes of EAS radar ranging assumes a high density of ionization electrons and the validity of the condition $r_c \ll \lambda$, where r_c is the distance from the axis at which the density of electrons is such that the plasma frequency exceeds that of the incident wave. According to (3.6), we obtain that 1 m away from the axis in the shower maximum region with the energy 10^{19} eV, the surface density of the relativistic electrons (in the ideally thin cascade disk) is $\rho_s = 5.5 \times 10^7$ m^{-2}. At the height of 4 km, the avalanche unit is 450 m. It is known that ionization energy losses by relativistic electrons are about 2 MeV g^{-1} cm^{-2}, or 0.16 MeV m^{-1} at the height of 4 km. It hence follows that along a 1 m path, each electron produces $\sim 5.3 \times 10^3$ ionization electrons, and all relativistic electrons of the cascade disk with the density $\rho_s = 5.5 \times 10^7$ m^{-2} create the volume density of ionization electrons $n_e = 1.4 \times 10^{11}$ m^{-3} $= 1.4 \times 10^5$ cm^{-3} (for the disk thickness ~ 2 m). The plasma frequency for this density is $\nu_p = (4\pi e^2 n_e/m)^{1/2}/(2\pi) = 3.5 \times 10^6$ Hz, which is far below the radar frequency 30 MHz, and hence the ionization column is almost transparent. In other words, it cannot be considered a metallic conductor. Moreover, with such a high collision rate of electrons with neutral particles ($\sim 10^{11}$ s^{-1}), it is hard to consider plasma oscillations. The 'friction' effect is so high that such a motion can hardly be treated as oscillatory.

(2) It is well known (see, e.g., [111]) that the lifetime (i.e., the time before 'adhesion') of a free thermalized electron in the normal atmosphere and at normal temperature is $\tau_e \approx 10^{-8}$ s and not 10 μs, as adopted in estimates [107]. Taking into account that all electrons stick to oxygen molecules in triple collisions, it is possible to calculate, for example, that this time increases fourfold at a height of about 6 km. This means that at heights of 6–10 km, the length of the track is shorter than 20–30 m, which is much lower than the first Fresnel zone length L_F for frequencies ~ 30 MHz (in [107], the Fresnel zone length is ~ 200 m).

(3) The collision frequency of an electron with neutral atoms at a height of about 6 km is $\sqrt{2}\pi N_a \bar{v} d^2 \approx 1.4 \times 3.14 \times 1.5 \times 10^{25} \times 10^5 \times 10^{-20} \approx 10^{11}$ s^{-1}. This means that in one period of oscillation at the radar frequency $\nu = 30$ MHz, an ionized electron collides with neutral molecules $\sim 3 \times 10^3$ times, and therefore the acceleration of the electron in the field of the incident wave is about several orders of magnitude smaller than that derived in [107].

(4) The number density of ionization electrons 1 m away from the axis of a shower with the energy $W_0 = 10^{19}$ eV, as calculated with the Nishimura–Kamata–Greisen distribution, is about 1.4×10^5 cm^{-2} (see item 1 above). The authors of [113, 114] consider showers with a density of $10^6 - 10^8$ cm^{-3}, which corresponds to the extremely high energy $10^{20} - 10^{22}$ eV and thus restricts the generality of the results. There is one more important note. The number density of electrons rapidly decreases toward the cascade disk periphery [see (3.6)], and therefore is not a function of only the coordinate x, as assumed in [113, 114]. For example, 100 m away from the axis of the shower considered, the electron number density is as small as 1 cm^{-3}. Thus, reducing the variables in the Maxwell equations to two independent variables, τ and ξ, may be misleading because it results in overestimating the total number of particles.

(5) It is definitely stated in [113, 114] that in the adopted emission model, the ionization electrons are almost immobile and are responsible for the reflection of the incident electromagnetic wave. Because the source and the observer are at rest, no Doppler frequency shift occurs, which is not commented on in [113, 114]. That the shower front propagates with a speed close to the speed of light only suggests that near the front, the waves emitted by each ionization electron can be added, but with their frequency unchanged. This addition is coherent if the front velocity is close to that of the propagation of the emission scattered by the ionization electrons in the incident wave field.

(6) The properties of the trace of ionization electrons that remains after the passage of the cascade disk are more similar to those of an ionized gas than plasma. A plasma is known to satisfy the three conditions

$$1)\ \lambda_D \ll L\,, \quad 2)\ N_D \gg 1\,, \quad 3)\ \omega_p \tau_\nu > 1\,,$$

where, according to the discussed papers, $\omega_p = (4\pi N e^2/m)^{1/2} \approx 2.6 \times 10^7$ s^{-1} is the plasma frequency, $N = 2.4 \times 10^5$ cm^{-3} is the electron number density at the axis of the shower with the energy $W_0 = 10^{19}$ eV, $e = 4.8 \times 10^{-10}$ (CGSE) is the electron charge, $m = 0.9 \times 10^{-27}$ g is the electron mass, $\lambda_D = k_B T/(8\pi e^2 N) \approx 0.2$ cm is the Debye radius, $k_B = 1.4 \times 10^{-16}$ erg K^{-1} is the Boltzmann constant, $N_D \approx 10^4$ is the number of particles in the Debye sphere, and $\tau_\nu = 1/\nu_{\text{eff}} \approx 2 \times 10^{-11}$ s is the effective collision time. The first two conditions are well satisfied, while the value $\omega_p \tau_\nu \approx 5 \times 10^{-3}$ is much less than unity.

(7) The cited papers ignore the fact that if $\nu_{\text{eff}} \gg \omega$, then the absorption coefficient is $\mu = 2\omega\chi/c \approx 4\pi e^2 N/(mc\nu_{\text{eff}}) \approx 2.5 \times 10^{-7}$ cm^{-1} [123]. The track length in an EAS is shorter than 30 m, and, consequently, with such a weak absorption, the EAS is virtually transparent to electromagnetic waves. In other words, the conductivity is very small even close to the axis (~ 700 CGSE), and the reflection from the track, as from a conducting object, is hardly justified. In this case, it is more appropriate to consider the ionized gas and Thomson scattering.

(8) The radio signal power at the receiver, Eqn (3.9), is calculated for Thomson scattering, which is valid only for free electrons in the vacuum and does not take collisions with neutral molecules into account. In [115], the radar frequency is 50 MHz and the oscillation period $T_0 = 2 \times 10^{-8}$ s is much larger than the time between collisions with neutral particles, $\tau_\nu = 1/\nu_{\text{eff}} \approx 2 \times 10^{-11}$ s, which means that in one oscillation period in the electromagnetic wave field, an ionization electron experiences 10^3 collisions. With these estimates, the received power is reduced by several orders of magnitude. This fact is not discussed in [115].

3.5 Model of radio emission from air showers in the ultra-high frequency range

The first attempts to observe UHF radio emission from EASs were reported in [124]. To check the effect of coherence on the radio pulse amplitude, a receiving antenna 15 m in diameter was placed near the radio detector with a working frequency of 44 MHz to observe the radio signal at a frequency of 150 MHz ($\lambda = 2$ m). During six weeks of observations, the high-frequency detector did not find any event, while five high-amplitude signals were detected at 44 MHz. The authors of [124] concluded that the cascade disk thickness is comparable to the wavelength ($\lambda = 2$ m) or possibly even exceeds it, which breaks the emission coherence, and the signal amplitude strongly decreases.

This quite natural conclusion seems to be the only reason for the absence of UHF radio emission from an EAS.

However, in the last decade, radio signals in the gigahertz range have been reported. The existing models explain this fact by the presence of parts in the cascade disk with sizes much smaller than the wavelength but with a much higher number density of charged particles (for example, near the axis). In such regions with enhanced particle number density, the Cherenkov and geomagnetic radiation mechanisms can operate [72]. This assumption does not seem to be compelling and ignores the fact that the coherence problem cannot always be considered separately from the emission from the entire system.

Other models consider bremsstrahlung radiation of ionization electrons generated in collisions of charged particles with neutral molecules in the atmosphere. This radiation is noncoherent and is therefore rather weak. However, by assuming nonthermal equilibrium in such an ionized gas, some models predict quite intensive radio emission [62]. These studies are mainly motivated by the results of laboratory tests (see, e.g., [62, 65, 125]). The laboratory results cannot be treated unambiguously, however.

As it turned out later, the model of noncoherent radio emission is possible [126] due to some *feature of emission in a finite track*, which is described below in detail.

Noncoherent emission of a relativistic electron (positron). The meaning of the term 'noncoherent emission of a relativistic electron (positron)' is somewhat unusual. The coherence concept is known to necessarily relate to a system of charges occupying a finite volume of space, which is not the case with the electron. However, the trajectory of an electron occupies an extended region, and the way the emission from different parts of the trajectory is added determines the amplitude of the radio pulse in the detector. A relativistic electron moves in Earth's atmosphere along a curved trajectory. By colliding with neutral molecules, the electron deviates chaotically from rectilinear motion. Most of the collisions deflect the electron trajectory insignificantly. But the deflections grow with time, and after passing some distance $\ell_{c,i}$ (depending on the wavelength), the deflection becomes such that at the next segment of the trajectory, $\ell_{c,i+1}$, the emission beam deviates from the initial direction (i.e., at the segment $\ell_{c,i}$) so much that they do not intersect at the location of the receiver. Clearly, the addition of signals induced by all the electrons of the shower at different segments $\ell_{c,i}$ is not coherent.

It is known that the RMS deviation $\mathrm{d}\langle\varphi^2\rangle$ from the initial direction of motion of an electron with the energy W, after passing the path length $\mathrm{d}t$ expressed in avalanche units, is determined as [104] $\mathrm{d}\langle\varphi^2\rangle = 0.5(W_s^2/W^2)\,\mathrm{d}t$, where $W_s = 21$ MeV. All ultrarelativistic charged particles in the shower, when passing through the atmosphere, lose energy for ionization, and the loss is independent of their energy (down to the energy corresponding to $\gamma \sim 3-5$). During these losses, the particle emits Cherenkov and geomagnetic radiation. In addition, the instant of the electron–positron pair creation (in the collision of a γ quantum with a nucleus) and its subsequent stop due to the ionization losses is accompanied by broadband bremsstrahlung radiation.

Very energetic electrons (positrons) with energies above some critical value (> 80 MeV) have similar losses, but their energy is transformed (via a high-energy γ quantum) into the energy of other charged particles with higher probability. Therefore, the relativistic electron (positron) emits radio emission via three processes: (1) creation and stop (bremsstrahlung); (2) Cherenkov radiation; (3) emission in the geomagnetic field (geomagnetic mechanism).

In [126], a feature of the radio emission from a relativistic electron in a finite path with a constant energy W is considered. Along the entire length L_i, the electron velocity is constant, but is zero at the beginning and end of the path. Elementary calculations [126] yield the energy (per Hz) per 1 m^2 over the whole time of motion along the path L_i:

$$\left|\mathbf{\Pi}_i(\omega,\mathbf{r},\theta)\right| = \frac{c}{\mu_0}\left[\frac{\mu_0\exp(\mathrm{i}\mathbf{kr})}{2\pi r}\right.$$
$$\left.\times\, q\,\frac{\sin\left[L_i k(1-\beta n\cos\theta)/2\right]}{1-\beta n\cos\theta}\sin\theta\right]^2\ [\mathrm{J\ m^{-2}\ Hz^{-1}}]\,. \quad (3.10)$$

The feature of the finite track emission is as follows. The modulus of Poynting vector (3.10) integrated over the sphere surrounding the source (over all angles $\mathrm{d}\Omega \sim \sin\theta\,\mathrm{d}\theta$) is very weakly dependent on the product kL_i, if $kL_i > 20-50$. For example, if kL_i changes from 50 to 10^4, i.e., 200-fold, the modulus $|\mathbf{\Pi}_i(\omega,\mathbf{r})|$ changes only threefold. Consequently, for any given wavelength λ corresponding to the observation frequency $\nu = c/\lambda$, there is the smallest segment where the emission is most effective.

The physical justification of this phenomenon is quite transparent. The emission at short wavelengths (compared to the entire path length) is produced by the ends of the segment, where the particle velocity abruptly changes and hence the acceleration tends to infinity. Therefore, independently of the length of the segment, the boundary regions near the ends mostly contribute to the bremsstrahlung radiation. On the contrary, the total energy of the Cherenkov radiation is proportional to the path length: the longer the path is, the larger the contribution of the Cherenkov radiation to the total emission. We note that in the vacuum with $n = 1$, the Cherenkov radiation is absent, and the bremsstrahlung radiation does not change. It is easy to verify that the total energy for the number of segments $N > 20$ is almost independent of the refractive index n.

In [126], the segments $\ell_{c,i}$ are found by taking the changing energy of the electron into account, which allows summing emission from all electrons of the shower using the energy distribution. Naturally, this summation is noncoherent, and the total intensity would be very small if the relativistic effects were absent. For relativistic particles, the forward emission is much more intensive than the isotropic one. In the case of an air shower, the emission from any relativistic electron, produced at any stage of the shower, propagates practically together with the shower front. This enhances the radiation density near the cascade disk, and the power of the signal increases due to the shortening of the pulse duration. Figure 13 shows the distribution of the radiation field from the shower with the energy $W_0 = 10^{18}$ eV at 10 GHz.

Omitting further details of the calculations, we note the conclusion in [126] that at a frequency of 10 GHz, an antenna with an effective area of 10 m^2 will be able to reliably detect radio pulses from air showers with energies $W_0 > 10^{19}$ eV.

4. Parameterization and modeling of radio emission from air showers

In Sections 2 and 3, radio emission from air showers was considered from the standpoint of a reliable detection of the

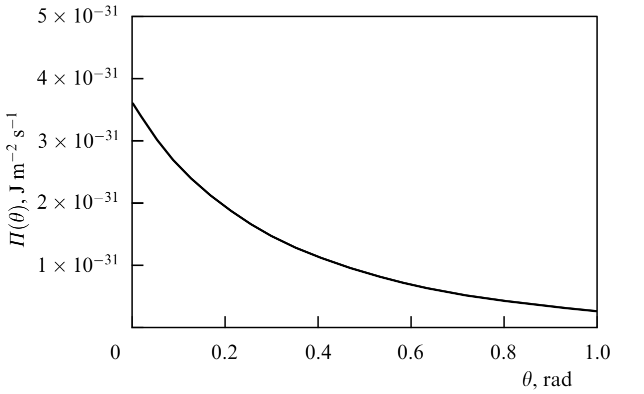

Figure 13. Radiation field from an EAS with the energy $W_0 = 10^{18}$ eV at a frequency $\approx$ 10 GHz.

actual incidence of a high-energy particle impact with the atmosphere. We discussed the technological potential of radio detectors, previously unknown radio emission mechanisms, and radio frequency bands where the signal intensity would be higher than electromagnetic backgrounds of different origins. In other words, we were primarily interested in the generation and detection of radio emission from air showers. However, in recent years, great progress in electronics and mathematical methods of data analysis has enabled using radio antenna arrays for determining the EAS parameters, including the primary particle energy or its type. Here, many results have been obtained, and a detailed discussion of all of them is far beyond the scope of this review. Below, we focus on the main achievements in this field.

Mathematical models of radio emission from air showers are currently at the development stage. The main limitations here are due to technical capabilities of modern computers.

The ultimate goal of any theory is to solve the inverse problem: to recover the EAS parameters (the incidence direction of the primary cosmic particle, its energy W_0, and the maximum shower location $X_{\max}$) from the radio data. The radio emission from EASs can be most accurately calculated by Monte Carlo simulations, in which the total emission from the shower is found as a sum of fields from each charged particle (the microscopic approach). In these models, the charged particle moves along the trajectory represented by a number of rectilinear segments on which the particle velocity is constant. But the direction of the segment, its length, and the velocity value bear a probabilistic character due to multiple Coulomb collisions or inelastic interactions of charged particles that lead to the creation of new particles. In this method, the time of modeling of the shower (i.e., the computer time) is known to increase proportionally to the primary particle energy. It turns out that to model the showers initiated by primary particles with energies above 5×10^{16} eV, the real time required to solve the full problem is beyond present computing capabilities.

Hence, the acute need appeared to develop a rapid and reliable method to model radio emission from EASs with energies $W_0 > 5 \times 10^{16}$ eV. Such a method is possible in principle because for working wavelengths 5–10 m, a single Fresnel zone contains many particles that emit coherently. Consequently, the emission from the entire zone and not from each individual particle can be taken into account. In this case, the main radiation mechanisms are related to the excess of electrons in the shower (the Askar'yan effect) and the presence of Earth's magnetic field (the geomagnetic mechanism). This is the macroscopic approach to modeling radio emission.

In both microscopic and macroscopic methods, the radiation field calculation is ultimately reduced to the integration of the spectral electric field strength $\mathbf{E}(\mathbf{r}, \omega) = c \operatorname{rot} \mathbf{A}(\mathbf{r}, \omega) \times \mathbf{n}$, where

$$\mathbf{A}(\mathbf{r}, \omega) = \frac{\mu_0}{4\pi} \int_{V'} \frac{\mathbf{j}(\mathbf{r}', \omega)}{|\mathbf{r} - \mathbf{r}'|} \exp\left(-\mathrm{i}k|\mathbf{r} - \mathbf{r}'|\right) \mathrm{d}V'$$

is the vector potential [127]. (Details of this method are described in [128–132].)

A radio detector consisting of a large antenna array measures the radio pulse amplitude in each antenna, its duration, and its shape. A mathematical model is required to determine these shower characteristics from radio data. The model can be tested using the data from surface particle detectors of EASs, which are currently believed to provide reliable data on cosmic particle properties in a wide energy range.

As mentioned above, a realistic model of radio emission can be constructed only for showers with an energy below 5×10^{16} eV. On the other hand, radio pulses from such showers are only slightly above the noise level. Nevertheless, there is a parameter region where such a test is possible. By comparing experimental radio data and surface detector particle data with calculations, it is possible to produce an algorithm to deduce shower parameters from radio data. However, this inverse problem does not always have a unique solution, for example, due to insufficient experimental radio data or ignorance of some effects in theoretical calculations that may be important under certain conditions.

Presently, these methods are actively being developed, for example, in the LOPES experiment with KASKADE-Grande, in the AERA experiment at the Pierre Auger Observatory, and in the CODALEMA experiment, which were mentioned in Section 2 and 3. In Sections 4.1–4.3, we discuss the results of these experiments, in particular, of the LOPES collaboration (see, e.g., [133–135]).

The spatial distribution of radio emission is one of the important characteristics of an EAS. It can be measured by a large antenna array. This distribution is closely related to important shower parameters, including the primary particle energy and the depth of the shower maximum, which in turn determines the primary particle type.

4.1 Spatial distribution function of emission

A parameterization of the field strength according to radio data was first proposed by Allan [81]. This parameterization relates the primary particle energy E_{p} to the electric field strength $E_\nu(R)$ at a distance R from the shower center as

$$E_\nu = 20 \, \frac{E_{\mathrm{p}}}{10^{17}\ \mathrm{eV}} \sin\alpha \cos\theta \exp\left(-\frac{R}{R_0(\nu, \theta)}\right) \times \left(\frac{\nu}{55\ \mathrm{MHz}}\right)^{-1} \left[\frac{\mu\mathrm{V}}{\mathrm{m\ MHz}}\right], \qquad (4.1)$$

where α is the geomagnetic angle (the angle between the shower axis and the direction of Earth's magnetic field) and θ is the zenith angle. The scale parameter is $R_0 \approx 110$ m for the frequency 55 MHz and zenith angles $\theta < 35°$. With increasing the zenith angle, R_0 increases. In fact, to estimate the primary particle energy, only the shower axis direction and the field strength at the distance R have to be known. Clearly, it is impossible to determine the zenith angle by one antenna. But if the radio detector includes a large antenna array, the zenith angle can be determined from the relative time delay of the radio signal without using data from a surface detector.

Expression (4.1) for the spatial distribution function (SDF) of the field strength $E_v(R)$ corresponds only approximately to the real distribution. For example, if $\alpha = 0$, then $E_v(R) = 0$, which is valid only for the geomagnetic radio emission mechanism. However, it is now well recognized that emission due to excess electrons (the Askar'yan effect) contributes only 10–15% to the total emission. For small angles α, when the shower axis is almost parallel to Earth's magnetic field, the SDF of radio emission has a deep minimum near the shower center (the crossing point of the shower axis with the ground). In this case, the radio emission is due to excess electrons in the shower. At some critical angle α, the geomagnetic mechanism starts dominating. The emission field strength is proportional to the geomagnetic field component $B \sin \alpha$. The field strength is maximal for showers propagating from north to south in the Northern Hemisphere.

We now discuss the most interesting results of the LOPES experiment.

Essentially, LOPES is a digital radio interferometer operating in the megahertz frequency range (43–74 MHz). It is located near the Karlsruhe Institute of Technology (Germany) on the territory of the KASKADE-Grande surface particle detector, where the magnetic declination is approximately 64.8°. In [134, 135], an inclination method is presented that uses the SDF of radio emission to reconstruct important characteristics of the primary cosmic rays. The authors present the results of modeling air showers and of a direct application of the inclination method to the LOPES experimental data.

The inclination method allows reconstructing the energy and depth of the air shower maximum from features of the spatial distribution of radio signals. First, the distance from the air shower axis is determined at which inferring the primary particle energy is sensitive to the slightest fluctuations. The presence of such a distance was predicted earlier from radio emission modeling by the REAS2 code [134]. The presence of such a distance was confirmed in [135] based on simulations with the CoREAS code [54], and it is especially clearly seen when the Askar'yan effect is taken into account. It is also shown that this fact can be used to estimate the primary particle energy. In addition, the slope of the distribution function is related to the distance to the observer. In other words, the inclination method allows determining the shower maximum depth $X_{\max}$ and hence the primary particle type. This information can be inferred directly from the SDF slope: air showers initiated by iron nuclei start earlier and develop faster in the atmosphere than showers initiated by protons. The radio source in the first case is located, as a rule, further from the ground-based observer; consequently, the cross distribution of the radio emission is flatter. Recently, this sensitivity to the SDF slope was proved experimentally by the LOPES measurements [82].

CoREAS modeling [54] includes a realistic treatment of the atmospheric refraction and is more complicated than the REAS modeling. The agreement between the CoREAS model and the measured SDF slope [136, 137] makes this model preferential among other computer models.

As noted in [135], there is still some contradiction between the CoREAS prediction and the measured radio pulse amplitudes. But this does not affect the analysis of the SDF slope (i.e., the ratio of the radio pulse amplitudes at different distances). The discrepancy mentioned above can be important only for the analysis of the absolute values of amplitudes, i.e., for estimating the energy that can be affected by calibration constants for linear correlation between the primary particle energy and the radio pulse amplitude.

Taking the results in [138] into account, the authors of [135] improved the inclination method. First, the inclination method was used in modeling radio emission by the CoREAS code to obtain important calibration parameters. Next, the inclination method was directly applied to results of the LOPES experiment, which enabled estimating the total energy of the primary particle and the shower maximum depth.

The signals selected for the analysis by the inclination method were detected by the LOPES-30 and LOPES-pol [139] experiments. The first installation consists of 30 calibration dipole antennas with an east–west orientation, and the second one includes 15 east–west antennas and 15 north–south antennas. The analysis was done only for data taken by the east–west antennas with richer statistics [22]. The effective frequency band in the LOPES experiment was 43–74 MHz. The selected showers had energies in the range $10^{17} - 10^{18}$ eV and zenith angles below 40°.

4.2 Modeling of the spatial distribution function of radio emission by the CoREAS code

The spatial distribution function describes the measured (or modeled) electric field as a function of the distance between the observer and the shower axis. A possible superposition of the geomagnetic and Cherenkov radio emission from air showers makes the SDF strongly asymmetric [136]. This is due to polarization features of the radiation mechanisms. The geomagnetic mechanism produces linear polarization, while the Cherenkov radiation is radially polarized. In other words, for observers located at arbitrary points on the ground near the shower axis, the electric field vector due to the geomagnetic mechanism has almost the same direction. For the same observers, the electric field vector of the Cherenkov emission necessarily passes through the shower axis (the so-called radial polarization). Therefore, the electric fields are added at some points and are subtracted at other points. This means that, ideally, it is necessary to construct a two-dimensional SDF, with the azimuthal angle used in addition to the distance to the shower axis. The LOPES experiment involves a limited number of antennas, and therefore a simplified method of SDF construction was used by averaging data taken by each antenna.

In their early papers, the authors of [135] used an exponential to approximate data and model the LOPES experiment [18, 137]. However, there are indications that it is preferential to use the one-dimensional Gaussian distribution

$$E(d) = E_{\mathrm{G}} \exp \frac{(d-b)^2}{2c^2}, \tag{4.2}$$

where E_{G} [μV m^{-1} MHz^{-1}], b [m], and c [m] are free model parameters to fit the SDF measured in the LOPES experi-

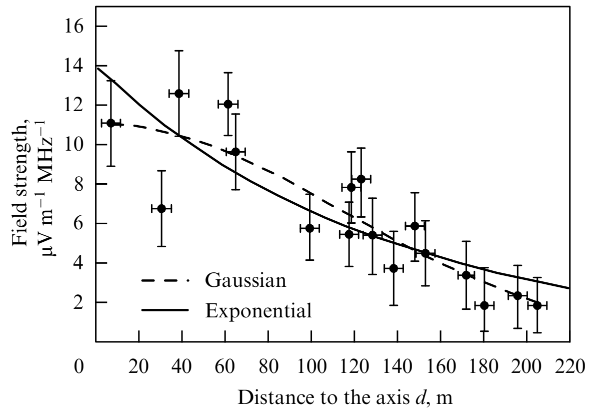

Figure 14. Approximation of the LOPES experimental data (filled circles) by a Gaussian (dashed curve) and an exponential (solid curve). The absolute values of amplitudes measured by LOPES and obtained from the CoREAS modeling are shown in different scales.

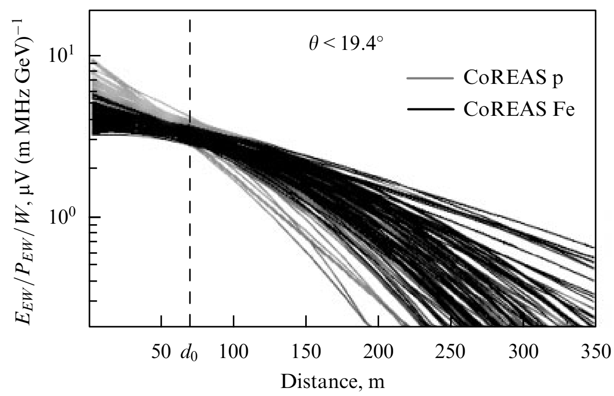

Figure 15. Normalized SDF obtained with the CoREAS code using a one-parametric Gaussian approximation for events with zenith angles $< 19.4°$. Light gray and solid curves respectively correspond to showers initiated by protons and iron nuclei. The dashed vertical line marks the distance d_0 at which the RMS deviation of the SDF is minimal.

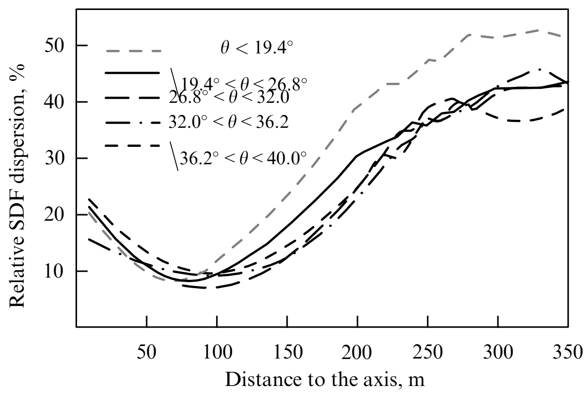

Figure 16. Relative RMS deviations from the SDF mean values as functions of the distance to the shower axis. The CoREAS modeling for different zenith angles.

ment. The LOPES events can be fitted by a one-dimensional exponential or a Gaussian function; however, the use of the Gaussian has two advantages. First, some events are much better described by the Gaussian. Second, which is more important, the inclination method is based on the CoREAS modeling, and the events approximated by the Gaussian function are in a much better agreement with the experimental data. This fact is illustrated in Fig. 14.

4.3 Method of inclination

To improve the inclination method, the SDFs modeled by CoREAS were compared with observations. Showers with different energies and zenith angles were analyzed. The field strength amplitude at the antenna location was normalized to the shower energy and the magnetic field component $B \sin\alpha$. The normalized spatial distribution functions for events with zenith angles $< 19.4°$ are shown in Fig. 15 [135]. It is seen that the spread of an SDF, approximated by a one-dimensional Gaussian, sharply changes with the distance to the shower axis.

Figure 16 shows the root mean square (RMS) deviation from the mean value for several groups of zenith angles [135]. The relative spread of the SDF changes from 10% at distances $d_0 = 70-100$ m to 50% at distances above 300 m. In both [135] and early models [134, 138], the existence of the specific distance d_0 was predicted at which the radio signal amplitudes are independent of the shower depth $X_{\max}$ and have a minimal spread of the normalized SDF.

4.3.1 Reconstruction of the primary energy of the shower (modeling). Normalized amplitudes of radio signals at the characteristic distance d_0 change insignificantly from shower to shower and provide direct information on its energy [134, 138]. This specific property can be established by modeling events with the CoREAS code. To do this, it is first necessary to choose the east–west component of the electric field vector from the CoREAS modeling for LOPES events. Then this amplitude should be normalized in accordance with the geomagnetic angle α, and the 'true' values of the shower energy determined by Monte Carlo simulations should be plotted as a function of the normalized amplitude $E_{d_0,\alpha}$. This plot is shown in Fig. 17 for events with zenith angles $\theta < 19.4°$. Analytically, this dependence can be written as

$$W = kE_{d_0,\alpha}\,, \tag{4.3}$$

where $E_{d_0,\alpha}$ is the field strength amplitude at the distance d_0 from the shower axis normalized to the geomagnetic angle α.

Clearly, parameterization (4.3) enables reconstructing the primary energy of the shower from the radio detector data. Figure 17 shows that the calculated energy deviates from a linear dependence. As mentioned above, this is due to the RMS deviation of SDFs at the distance d_0 from the axis (see Figs 15 and 16), which is about 9%. In addition, there is a 10% dispersion in the measured amplitudes. These uncertainties could be decreased if the asymmetry due to Cherenkov radiation were taken into account.

Figure 17 also suggests the presence of a systematic shift in the energy depending on the particle type. The amplitudes of radio pulses from proton showers are somewhat higher than those from iron showers. This can be understood because the field strength amplitude depends only on the electromagnetic shower component, and the shower initiated by an iron nucleus transfers more energy to the nonelectromagnetic component than the proton shower does [140]. Besides, the maximum of a proton shower lies closer to the ground, and the field strength is accordingly higher.

Table 3. Inclination parameter k calculated with the CoREAS code and measured by the LOPES array at the characteristic distance d_0 for showers with different zenith angles.

Zenith angle $\Delta\theta$, grad	Number of showers	Distance d_0, m (CoREAS modeling)	CoREAS modeling		LOPES data	
			$\sqrt{\mathrm{RMS}^2 + 20\,\%}$, %	Parameter k, GeV m MHz μV^{-1}	RMS, %	Parameter k, GeV m MHz μV^{-1}
0 – 19.4	53	70	21.8	0.299	18.8	0.134
19.4 – 26.8	48	80	21.6	0.328	23.1	0.151
26.8 – 32.0	45	90	21.4	0.358	24.6	0.141
32.0 – 36.2	36	100	22.1	0.382	20.3	0.142
36.2 – 40.0	23	100	22.4	0.398	25.6	0.137

4.3.2 Reconstruction of the primary energy of the shower (from LOPES data). Figure 18 shows the results of reconstructing the primary energy in real events registered by the LOPES detector. The field strength at the distance $d_0 = 70$ m from the axis is plotted along the abscissa for each shower. The field strength is determined from a Gaussian SDF. Along the ordinate, the primary energy of the shower inferred from KASKADE-Grande data is plotted. In total, 53 events with zenith angles $\theta < 19.4°$ are shown. The solid line corresponds to dependence (4.3). Table 3 lists the inclination parameter k obtained from CoREAS modeling and measured by the LOPES array at the characteristic distance d_0 for a wide range of zenith angles θ.

To compare the measured amplitudes at the characteristic distance of 100 m with amplitudes predicted by CoREAS, cross-checking was done, which confirmed that the difference between amplitudes measured from the LOPES data and CoREAS modeling increases with the zenith angle. The reason for this discrepancy is still unknown. For example, it can be due to the difference in the model antenna beams and real beams in the LOPES array.

4.3.3. Reconstruction of the shower maximum depth (CoREAS modeling). Another feature of radio emission from air showers is a clear correlation of the shower maximum depth with the SDF slope. To further improve the inclination method, it is necessary to establish a quantitative relation between the shower maximum depth and some inclination parameter using the CoREAS modeling and then to apply it to real LOPES data. For the LOPES detector, the ratio of radio signal amplitudes measured at the distance d_0 and at the fiducial distance 200 m, $\varepsilon_{\mathrm{ratio}} = E_{d_0}/E_{200}$, can be chosen as such a parameter. To calibrate this dependence, the values of $X_{\max}$ obtained from Monte Carlo simulations are assumed to be 'true' depths. Calculations show a clear correlation, which can be parameterized in the form

$$\varepsilon_{\mathrm{ratio}} = B \exp\left[(A X_{\max})^C\right]. \tag{4.4}$$

The parameters A, B, and C and statistical uncertainties are found separately for each zenith angle.

Figure 19 shows the values of $\varepsilon_{\mathrm{ratio}}$ for showers with zenith angles $\theta < 19.4°$ as a function of the 'true' depths $X_{\max}$. As expected, maxima of showers initiated by the primary Fe nucleus (unfilled squares) lie systematically lower than the proton shower maxima.

Table 4 shows how the parameters A, B, and C in (4.4) change with the angle θ. This table lists dispersions $\Delta X_{\max}$ for proton and 'iron' showers for individual groups of zenith angles. In the CoREAS modeling, double statistics were used (denoted as $n \times 2$ in Table 4) and, with account for all zenith angles, the RMS dispersion lies in the range 45–65 g cm^{-2}.

It is important to note that the results presented in Table 4 and in Fig. 19 are related to the characteristic parameters of the LOPES detector, including its altitude, frequency range, shower energy range, and antenna array size. These parameters influence the amplitude ratio and are important for calibrating $\Delta X_{\max}$ curves. Apparently, for tilted showers,

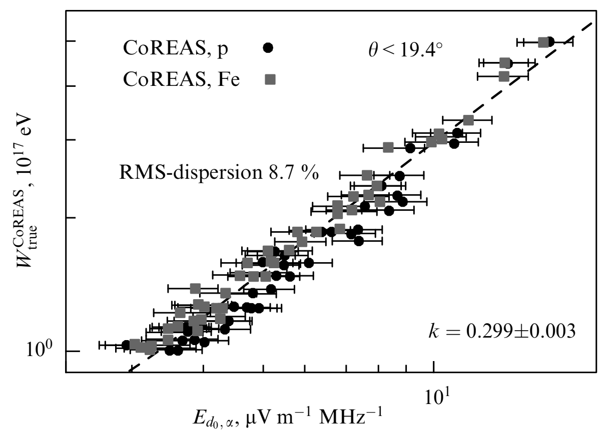

Figure 17. Linear correlation between the 'true' value of the primary energy $W_{\mathrm{true}}^{\mathrm{CoREAS}}$ calculated by the Monte Carlo method and the radio pulse amplitude at the distance d_0; k is a fitting parameter. The relative RMS dispersion of amplitudes is ≈ 8.7.

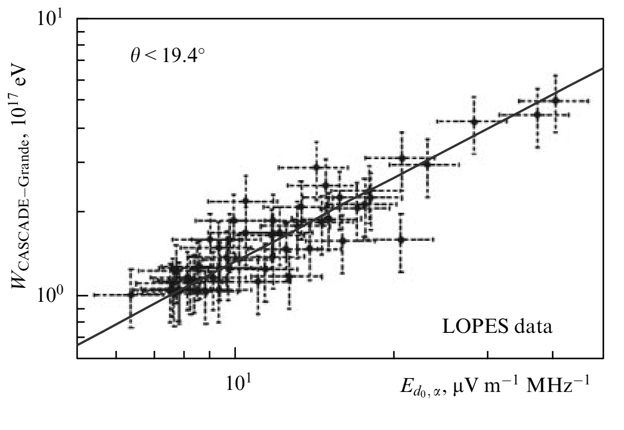

Figure 18. Reconstructed primary energy of showers with zenith angles $< 19.4°$ from the normalized field strength measured in the LOPES experiment at the distance d_0. The relative RMS deviation is 18.8%. The solid line corresponds to Eqn (4.3) with the coefficient $k = 0.134$.

Table 4. Reconstruction parameter ΔX_{max} from the CoREAS modeling and their statistic uncertainties.*

Zenith angle $\Delta\theta$, grad	Number of calculated cycles	Parameter A, cm^2 g^{-1}	Parameter B	Parameter C	ΔX_{max}, g cm^{-2}
0 – 19.4	53 × 2	0.0087 ± 0.0016	0.0577 ± 0.0022	0.841 ± 0.055	54.0
19.4 – 26.8	48 × 2	0.0060 ± 0.0034	0.0835 ± 0.0084	0.945 ± 0.016	47.9
26.8 – 32.0	45 × 2	0.0014 ± 0.0010	1.100 ± 0.092	2.542 ± 0.011	53.2
32.0 – 36.2	36 × 2	0.0053 ± 0.0018	0.225 ± 0.018	0.691 ± 0.027	65.7
36.2 – 40.0	23 × 2	0.0013 ± 0.0002	0.98 ± 0.52	2.8 ± 2.0	47.9

* The last column shows the RMS deviation from the mean value ΔX_{max} (CoREAS) for each zenith angle interval. The values presented in the table are obtained by a two-fold increase in the statistics in the modeling.

large values of $\varepsilon_{ratio} = E_{d_0}/E_{200}$ can occur only for distances much longer than 200 m. In the inclination method discussed above, it is impossible to increase the distance due to the LOPES size restrictions.

4.3.4 Reconstruction of the shower maximum depth (POLES measurements). Three-parameter function (4.4) can be used to reconstruct the parameter X_{max} from data obtained by the LOPES antenna array and the parameters A, B, and C calculated by the CoREAS code, which are listed in Table 4 for the corresponding zenith angles.

Figure 20 shows the obtained distribution of X_{max}^{LOPES} (solid histogram) with the mean value $\bar{X}_{max} = 633.2$ g cm^{-2} and the standard deviation $\Delta X_{max} = 94.6$ g cm^{-2}. For comparison, also presented are the distribution of X_{max} according to the CoREAS modeling for proton showers (dashed-dotted histogram) with the mean value $\bar{X}_{max,p}^{CoREAS} = 678.5 \pm 76.9$ g cm^{-2} and 'iron' showers (dashed histogram) with $\bar{X}_{max,Fe}^{CoREAS} = 604.2 \pm 56.4$ g cm^{-2}. These values were calculated by using formula (4.4) in the CoREAS modeling; in other words, they are derived from the corresponding SDF slope approximations.

The standard deviation $\Delta X_{max} = 94.6$ g cm^{-2} for the X_{max} distribution can be taken as an upper bound for the LOPES radio detector accuracy. However, this is not an exact calculation of the standard deviation, because in this case, for example, modeling errors of the atmosphere and hadron interactions were ignored. Much better results can be obtained from high-quality radio measurements by a larger antenna array. For example, in the LOFAR experiment [141], a method based on approximating the two-dimensional SDF of radio emission is used, and a sensitivity in measurements of X_{max} is reached (≈ 20 g cm^{-2}) that is comparable to that of the fluorescence method.

Generally, the reconstructed values of X_{max}^{LOPES} agree with theoretical expectations. The result of the previous analysis [138], in which the atmospheric refractive index was set to unity, is significantly improved. The authors of [135] argue that the systematic shift noticed earlier in [138] is due to the inconsistency of the SDF slope derived from previous models and experimental measurements.

In the foregoing, we used all the potential of the LOPES data and the accepted methods of data analysis. However, present-day and forthcoming experiments, such as ARE, Tunka-Rex, and LOFAR, will obtain higher-quality data due to a lower level of radio interference, a larger number of antennas per single event, and an increase in the transverse distances of the SDFs for each event. Naturally, the methods described above should be improved to reach higher accuracy. In particular, the SDF asymmetry due to the charge excess should be taken into account. Expression (4.4) used to approximate X_{max} should be revised, and the parameter degeneracy should be minimized. Most likely, a more complicated expression will be used instead of (4.4). Finally, it is possible that the use of the Gaussian approximation is not the best choice and a more accurate fit should be

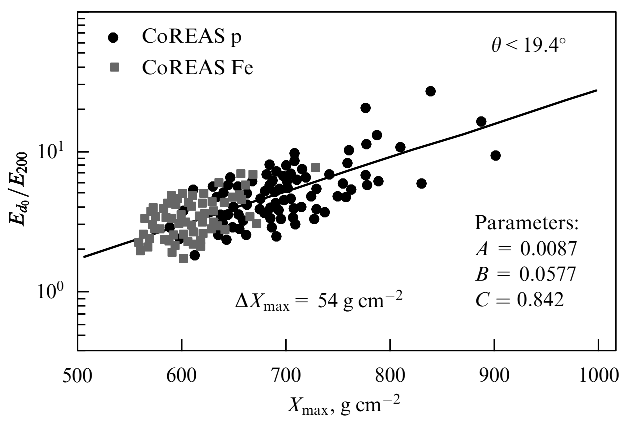

Figure 19. Relation between the 'true' shower maximum X_{max} obtained by Monte Carlo simulations and the inclination parameter $\varepsilon_{ratio} = E_{d_0}/E_{200}$ found from the CoREAS modeling. The RMS deviation is $\Delta X_{max} = 54$ g cm^{-2}.

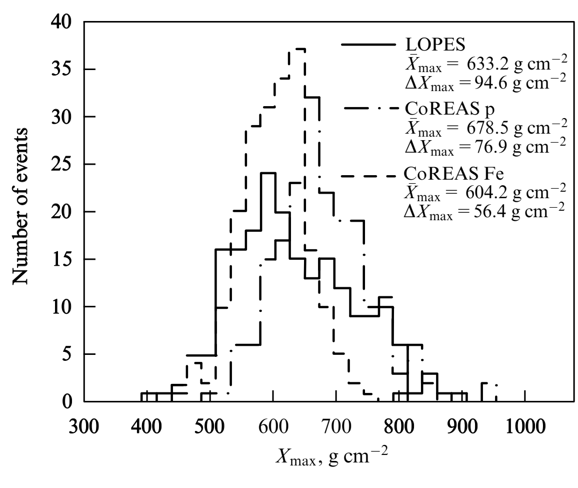

Figure 20. Distribution of the maximum depth X_{max} reconstructed by the inclination method from the LOPES detector data (solid histogram) and obtained by CoREAS modeling of the same events for protons (dashed-dotted histogram) and iron nuclei (dashed histogram).

sought. Nevertheless, despite these remarks, the inclination method for the determination of $X_{\max}$ from SDFs of radio emission appears to have good prospects for radio detection of air showers.

5. Conclusion

Presently, just as many years ago, there is hope that the radio method will be improved to be used for detecting radio emission from air showers with energies above the GZK cut-off. It is difficult to say now which detector will be able to perform these measurements and when. New areas of studies inspire optimism. A recent report on the detection of gigahertz radio emission from air showers and new applications of the radar detection method seem to be important. Radar detection is of special interest, because currently only this method provides the possibility of actively affecting an air shower. For example, an increase in the transmitter power appears to be very promising for radio detection. Other methods are restricted by only passive data analysis.

The new stage in EAS radio detection is due to the rapid development of electronics and information technologies. New results are expected from the radio astronomical method [142]. Initial attempts to use the radio astronomical method failed. There can be many reasons why no lunar cosmic ray events have been observed so far. Apparently, the radio astronomical method needs serious improvement. There are indications that the radio astronomical method in the decameter frequency range may help in solving this problem. Last, the realization of space projects of cosmic ray observations from artificial satellites around the Moon and other planets is very promising [143].

References

1. Askar'yan G A *Sov. Phys. JETP* **14** 441 (1962); *Zh. Eksp. Teor. Fiz.* **41** 616 (1961)
2. Askar'yan G A *Sov. Phys. JETP* **21** 658 (1965); *Zh. Eksp. Teor. Fiz.* **48** 988 (1965)
3. Kahn F D, Lerche I *Proc. R. Soc. Lond. A* **289** 206 (1966)
4. Jelley J V et al. *Nature* **205** 327 (1965)
5. Filonenko A D *Phys. Usp.* **45** 403 (2002); *Usp. Fiz. Nauk* **172** 439 (2002)
6. Allan H R *Acta Phys. Hung.* **29** (Suppl. 1) (1970)
7. Gusev G A, Zheleznykh I M *JETP Lett.* **38** 611 (1983); *Pis'ma Zh. Eksp. Teor. Fiz.* **38** 505 (1983)
8. Hankins T H, Ekers R D, O'Sullivan J D *Mon. Not. R. Astron. Soc.* **283** 1027 (1996)
9. Filonenko A D *Phys. Usp.* **55** 741 (2012); *Usp. Fiz. Nauk* **182** 793 (2012)
10. Rosner J L, hep-ex/9508011
11. Rosner J L, Wilkerson J F, hep-ex/9702008
12. Rosner J L, Denis Suprun A *AIP Conf. Proc.* **579** 81 (2001); astro-ph/0101089
13. Antoni T et al. *Nucl. Instrum. Meth. Phys. Res. A* **513** 490 (2003)
14. Navarra G et al. *Nucl. Instrum. Meth. Phys. Res. A* **518** 207 (2004)
15. Horneffer A et al. (LOPES Collab.), astro-ph/0409641
16. Petrovic J et al. (LOPES Collab.) *J. Phys. Conf. Ser.* **39** 471 (2006); astro-ph/0611225
17. Falcke H et al. *Nature* **435** 313 (2005)
18. Apel W D et al. *Astropart. Phys.* **32** 294 (2010)
19. Huege T, Ulrich R, Engel R *Astropart. Phys.* **30** 96 (2008)
20. Apel W D et al. (LOPES Collab.) *Astropart. Phys.* **26** 332 (2006)
21. Haungs A et al. (LOPES Collab.) *Nucl. Instrum. Meth. Phys. Res. A* **604** S1 (2009); arXiv:0811.1919
22. Horneffer A et al. (LOPES Collab.), in *Proc. of the 30th Intern. Cosmic Ray Conf. July 3 – 11, 2007, Mérida, Yucatán, Mexico* Vol. 4 (Eds R Caballero et al.) (Mexico City, Mexico: Univ. Nacional Autonoma de Mexico, 2008)
23. Nigl A et al. (LOPES Collab.) *Astron. Astrophys.* **487** 781 (2008)
24. Palmieri N et al., in *Proc. of the 32nd Intern. Cosmic Ray Conf., ICRC2011, 11 – 18 August, 2011, Beijing, China* Vol. 4, p. 60
25. Apel W D et al. (LOPES Collab.) *Phys. Rev. D* **85** 071101(R) (2012); arXiv:1203.3971
26. Apel W D et al. (LOPES Collab.) *Astropart. Phys.* **50–52** 76 (2013); arXiv:1309.5920
27. Apel W D et al. *Nucl. Instrum. Meth. Phys. Res. A* **696** 100 (2012); arXiv:1303.6808
28. Huber D et al., arXiv:1308.2512
29. Ravel O et al. *Nucl. Instrum. Meth. Phys. Res. A* **518** 213 (2004); astro-ph/0306255
30. Ardouin D et al. *Nucl. Instrum. Meth. phys. Res. A* **572** 481 (2007)
31. Lebrun D and the CODALEMA Collab., in *Proc. of the 30th Intern. Cosmic Ray Conf. July 3 – 11, 2007, Mérida, Yucatán, Mexico (Mexico City, Mexico: Univ. Nacional Autonoma de Mexico, 2008)*
32. Riviere C (for the CODALEMA Collab.), arXiv:0906.2720
33. Revenu B (for the CODALEMA Collab.), arXiv:0906.2832
34. Bellétoile A for the (CODALEMA Collab.), in *Proc. of the 32nd Intern. Cosmic Ray Conf., ICRC2011, 11 – 18 August, 2011, Beijing, China* Vol. 1, p. 231; arXiv:1109.3579
35. Rebai A and the CODALEMA Collab., arXiv:1211.3273
36. Gandhi R et al. *Astropart. Phys.* **5** 81 (1996); hep-ph/9512364
37. Gandhi R et al. *Phys. Rev. D* **58** 093009 (1998); hep-ph/9807264
38. Brusova O et al., in *Proc. of the 30th Intern. Cosmic Ray Conf., July 3 – 11, 2007, Mérida, Yucatán, Mexico* Vol. 5 (Eds R Caballero et al.) (Mexico City, Mexico: Univ. Nacional Autonoma de Mexico, 2008) p. 1585; arXiv:0708.3824
39. Ardouin D et al. *Astropart. Phys.* **34** 717 (2011); arXiv:1007.4359
40. Ardouin D et al. *Nucl. Instrum. Meth. Phys. Res. A* **604** S85 (2009)
41. Carloganu C et al., in *Proc. of the 44th Rencontres de Moriond, La Thuile, Italy 2009*
42. Lamblin J and the CODALEMA Collab., in *Proc. of the 30th Intern. Cosmic Ray Conf. July 3 – 11, 2007, Mérida, Yucatán, Mexico* Vol. 5 (Eds R Caballero et al.) (Mexico City, Mexico: Univ. Nacional Autonoma de Mexico, 2008) p. 921
43. Ardouin D et al. *Nucl. Instrum. Meth. Phys. Res. A* **604** S85 (2009); arXiv:0902.0730
44. Ardouin D et al. *Astropart. Phys.* **31** 192 (2009); arXiv:0901.4502
45. van den Berg A M for the Pierre Auger Collab., in *Proc. of the 30th Intern. Cosmic Ray Conf. July 3 – 11, 2007, Mérida, Yucatán, Mexico* Vol. 4 (Eds R Caballero et al.) (Mexico City, Mexico: Univ. Nacional Autonoma de Mexico, 2008) p. 885; arXiv:0708.1709
46. Huege T for the Pierre Auger Collab. *Nucl. Instrum. Meth. Phys. Res. A* **617** 484 (2010); arXiv:0906.4970
47. Klages H O, in *Proc. of the 30th Intern. Cosmic Ray Conf. July 3 – 11, 2007, Mérida, Yucatán, Mexico* Vol. 5 (Eds R Caballero et al.) (Mexico City, Mexico: Univ. Nacional Autonoma de Mexico, 2008) p. 849
48. Etchegoyen A, in *Proc. of the 30th Intern. Cosmic Ray Conf. July 3 – 11, 2007, Mérida, Yucatán, Mexico* Vol. 5 (Eds R Caballero et al.) (Mexico City, Mexico: Univ. Nacional Autonoma de Mexico, 2008) p. 1191
49. Huege T *Nucl. Instrum. Meth. Phys. Res. A* **604** (1 – 2) S57 (2009)
50. Abreu P et al. (Pierre Auger Collab.), arXiv:1107.4807
51. Abreu P et al. *JINST* **7** P10011 (2012); arXiv:1209.3840
52. Schröder F G, Asch T, Bähren L *Nucl. Instrum. Meth. Phys. Res. A* **615** 277 (2010)
53. Aab A et al. (The Pierre Auger Collab.), in *33rd Intern. Cosmic Ray Conf., Rio de Janeiro, Brazil, July 2013, The Astroparticle Physics Conf.*

54. Huege T, Ludwig T M, James C, in *Proc. 5th ARENA, Erlangen, Germany*; *AIP Conf. Proc.* **1535** 128 (2013)
55. Alvarez-Muniz J, Carvalho W R, Zas E (Jr.) *Astropart. Phys.* **35** 325 (2012)
56. Marin V, Revenu B *Astropart. Phys.* **35** 733 (2012)
57. Werner K, Vries K D, Scholten O *Astropart. Phys.* **37** 5 (2012)
58. Ardouin D et al. *Astropart. Phys.* **31** 192 (2009)
59. Glaser C, Weidenhaupt K, in *ARENA-2012, Acoustic and Radio EeV Neutrino Detection Activities, Erlangen, Germany*
60. Aab A et al. (The Pierre Auger Collab.), arXiv:1307.5059
61. Louedec K for the Pierre Auger Collab., arXiv:1310.4603
62. Gorham P W et al., arXiv:0705.2589
63. Gorham P W et al. *Phys. Rev. D* **78** 032007 (2008)
64. Belz J for the FLASH Collab., in *Proc. of the 29th Intern. Cosmic Ray Conf., August 3 – 10, 2005, Pune, India* Vol. 8 (Eds B Sripathi Acharya et al.) (Mumbai: Tata Institute of Fundamental Research, 2005) p. 291; astro-ph/0507379
65. Monasor M, Bohacova M, Bonifazi C, in *Proc. of the 32nd Intern. Cosmic Ray Conf., ICRC2011, 11 – 18 August, 2011, Beijing, China* Vol. 3, p. 196
66. Smida R et al., in *Proc. of the 32nd Intern. Cosmic Ray Conf., ICRC2011, 11 – 18 August, 2011, Beijing, China* Vol. 3, p. 17; arXiv:1108.0588
67. Apel W D et al. *Nucl. Instrum. Meth. Phys. Res. A* **620** 202 (2010)
68. Šmida R et al., arXiv:1306.6738
69. Šmida R et al. *EPJ Web Conf.* **53** 08010 (2013)
70. Alvarez-Muñiz J et al. *Phys. Rev. D* **86** 051104(R) (2012); arXiv:1205.5785
71. Gaisser T K, Hillas A M, in *Proc. of the 15th Intern. Cosmic Ray Conf. Plovdiv 1977* Vol. 8, p. 353
72. Alvarez-Muñiz J et al. *Phys. Rev. D* **86** 123007 (2012); arXiv:1208.0951
73. Facal P for the Pierre Auger Collab. *EPJ Web Conf.* **53** 08009 (2013)
74. Allison P S, for the Pierre Auger Collab., in *Proc. of the 32nd Intern. Cosmic Ray Conf., ICRC2011, 11 – 18 August, 2011, Beijing, China*
75. Conti E, Collazuo G, Sartori G *Phys. Rev. D* **90** 071102(R) (2014); arXiv:1408.5886
76. Schröder F G et al. (Tunka-Rex Collab.), arXiv:1308.0910
77. Hörandel J R et al. *Nucl. Instrum. Meth. Phys. Res.* **630** 171 (2011); arXiv:0911.2371
78. Schröder F G et al. *AIP Conf. Proc.* **1535** 78 (2013)
79. Glaser C, for the Pierre Auger Collab. *AIP Conf. Proc.* **1535** 68 (2013)
80. Rebai A et al., arXiv:1210.1739
81. Allan H R *Prog. Elem. Part. Cosmic Ray Phys.* **171** 10 (1971)
82. Apel W D et al. (LOPES Collab.) *Phys. Rev. D* **85** 071101(R) (2012)
83. Vries K D et al. *Astropart. Phys.* **34** 267 (2010)
84. Ludwig M, Huege T *Astropart. Phys.* **34** 438 (2011)
85. Buitink S et al. *Astropart. Phys.* **33** 296 (2010); arXiv:1002.4849
86. Scholten O, Werner K, Rusydi F *Astropart. Phys.* **29** 94 (2008)
87. Werner K, Scholten O *Astropart. Phys.* **29** 393 (2008)
88. Werner K, de Vries K D, Scholten O *Astropart. Phys.* **37** 5 (2012)
89. Huege T et al. *Nucl. Instrum. Meth. Phys. Res. A* **662** S179 (2012)
90. Scholten O, Werner K, Rusydi F *Astropart.Phys.* **29** 94 (2008); arXiv:0709.2872
91. Greisen K *Prog. Cosmic Ray Phys.* **3** 1 (1956)
92. Kamata K, Nishimura J *Prog. Theor. Phys. Suppl.* **6** 93 (1958)
93. Khristiansen G B, Kulikov G, Fomin J *Cosmic Rays of Superhigh Energies* (München: Verlag Karl Thiemig, 1980); Translated from Russian: *Kosmicheskoe Izluchenie Sverkhvysokoi Energii* (Moscow: Atomizdat, 1975)
94. Belen'kii S Z *Lavinnye Protsessy v Kosmicheskikh Luchakh* (Avalanche Processes in Cosmic Rays) (Moscow: Gostekhizdat, 1948)
95. De Vries K D et al. *Phys. Rev. Lett.* **107** 061101 (2011); arXiv:1107.0665
96. Werner K, De Vries K D, Sholten O, arxiv:1201.4471
97. Falcke H, Gorham P *Astropart. Phys.* **19** 477 (2003); astro-ph/0207226
98. Huege T, Falcke H *Astron. Astrophys.* **412** 19 (2003)
99. Jackson J D *Classical Electrodynamics* (New York: Wiley, 1962); Translated into Russian: *Klassicheskaya Elektrodinamika* (Moscow: Mir, 1965)
100. Agnetta G et al. *Astropart. Phys.* **6** 301 (1997)
101. Atrashkevich V B et al. *Sov. J. Nucl. Phys.* **28** 366 (1978); *Yad. Fiz.* **28** 712 (1978)
102. Huege T, Falcke H *Astron. Astrophys.* **430** 779 (2005)
103. Filonenko A D *JETP Lett.* **97** 178 (2013); *Pis'ma Zh. Eksp. Teor. Fiz.* **97** 203 (2013)
104. Murzin V S *Vvedenie v Fiziku Kosmicheskikh Luchei* (Introduction to the Physics of Cosmic Rays) (Moscow: Izd. MGU, 1988)
105. Kalmykov N N et al., in *31-ya Vserossiiskaya Konf. po Kosmicheskim Lucham, Moskva, 5–9 Iyulya, 2010* (Proc. of the 31st All-Russian Cosmic Ray Conf., Moscow, 5–9 July, 2010) (Moscow: Izd. MGU, 2010)
106. Blackett P M S, Lovell A C B *Proc. R. Soc. Lond. A* **177** 183 (1941)
107. Gorham P W *Astropart. Phys.* **15** 177 (2001); hep-ex/0001041
108. Hayakawa S *Cosmic Ray Physics* (New York: Wiley-Intersci., 1969); Translated into Russian: *Fizika Kosmicheskikh Luchei* (Moscow: Mir, 1973)
109. Rossi B, Greisen K *Rev. Mod. Phys.* **13** 240 (1941); Translated into Russian: *Vzaimodeistvie Kosmicheskikh Luchei s Veshchestvom* (The Interaction of Cosmic Rays with Matter) (Moscow: IL, 1948)
110. Grupen C *Particle Detectors* (Cambridge: Cambridge Univ. Press, 1996); Translated into Russian: *Detektory Elementarnykh Chastits* (Novosibirsk: Sib. Khronograf, 1999)
111. Raizer Yu P *Gas Discharge Physics* (Berlin: Springer, 1997); Translated from Russian: *Fizika Gazovogo Razryada* (Moscow: Nauka, 1992)
112. Aizenberg G Z *Antenny Ul'trakorotkikh Voln* (Ultra-short Wave Antennas) (Moscow: Svyaz'izdat, 1957)
113. Bakunov M I et al. *Astropart. Phys.* **33** 335 (2010)
114. Bakunov M I, Novokovskaya A L *Vestn. Nizhegorodskogo Univ. Im. Lobachevskogo* (5(3)) 160 (2011)
115. Takai H et al. *32th ICRC Beijing* (2011)
116. Abou Bakr Othman et al., in *Proc. of the 32nd Intern. Cosmic Ray Conf., ICRC2011, 11 – 18 August, 2011, Beijing, China*
117. Abou Bakr Othman et al., in *33rd Intern. Cosmic Ray Conf., Rio de Janeiro, Brazil, July 2013*
118. Stasielak J et al. *EPJ Web Conf.* **53** 08013 (2013); arXiv:1210.1427
119. Stasielak J et al., arXiv:1310.0743
120. Filonenko A D *JETP* **117** 641 (2013); *Zh. Eksp. Teor. Fiz.* **144** 739 (2013)
121. Engel A *Ionized Gases* (Oxford: Clarendon Press, 1955); Translated into Russian *Ionizovannye Gazy* (Moscow: Fizmatgiz, 1959)
122. Raizer Yu P *Osnovy Sovremennoi Fiziki Gazorazryadnykh Protsessov* (Basics of Modern Physics of Gas Discharge Processes) (Moscow: Nauka, 1980)
123. Ginzburg V L *The Propagation of Electromagnetic Waves in Plasmas* (Oxford: Pergamon Press, 1964); Translated from Russian: *Rasprostranenie Elektromagnitnykh Voln v Plazme* (Moscow: Fizmatgiz, 1960)
124. Jelley J V et al. *Nuovo Cimento A* **46** 649 (1966)
125. Alvarez-Muñiz J et al. *EPJ Web Conf.* **53** 08011 (2013)
126. Filonenko A D *JETP Lett.* **99** 250 (2014); *Pis'ma Zh. Eksp. Teor. Fiz.* **99** 290 (2014)
127. Landau L D, Lifshitz E M *The Classical Theory of Fields* (Oxford: Pergamon Press, 1975); Translated from Russian: *Teoriya Polya* (Moscow: Nauka, 1967) p. 460
128. Scholten O, de Vries K D, Werner K *EPJ Web of Conf.* **53** 08005 (2013); arXiv:1207.1874
129. Suprun D A, Gorham P W, Rosner J L *Astropart. Phys.* **20** 157 (2003); astro-ph/0211273

130. Vedeneev O V, Kalmykov N N, Konstantinov A A "Sravnenie eksperimental'nykh i raschetnykh prostranstvennykh raspredelenii radioizlucheniya ShAL po dannym MGU i LOPES" ("Comparison of experimental and calculated spatial distributions of radio emission from EAS from the MSU and LOPES data"), in *31-ya Vserossiiskaya Konf. po Kosmicheskim Lucham, Moskva, 5–9 Iyulya, 2010* (Proc. of the 31st All-Russian Cosmic Ray Conf., Moscow, 5–9 July, 2010) (Moscow: Izd. MGU, 2010)
131. Kalmykov N N, Konstantinov A A, Engel R *Phys. Atom. Nucl.* **73** 1191 (2010); *Yad. Fiz.* **73** 1231 (2010)
132. Kalmykov N N, Konstantinov A A *Phys. Atom. Nucl.* **74** 1019 (2011); *Yad. Fiz.* **74** 1047 (2011)
133. Nehls S "Calibrated measurements of the radio emission of cosmic ray air showers", Dissertation (Karlsruhe: Institut für Experimentelle Kernphysik, 2008)
134. Huege T, Ulrich R, Engel R *Astropart. Phys.* **30** 96 (2008); arXiv:0806.1161
135. Apel W D et al. (LOPES Collab.) *Phys. Rev. D* **90** 062001 (2014); arXiv:1408.2346
136. Huege T *Braz. J. Phys.* **44** 520 (2014)
137. Apel W D et al. (The LOPES Collab.) *Astropart. Phys.* **50–52** 76 (2013)
138. Palmieri N et al. (The LOPES Collab.) *AIP Conf. Proc.* **1535** 89 (2012)
139. Huege T et al. (The LOPES Collab.) *Nucl. Instrum. Meth. Phys. Res. A* **662** S72 (2010)
140. Matthews J *Astropart. Phys.* **22** 387 (2004)
141. Buitink S et al. (The LOFAR Collab.) *Brazilian J. Phys.*; in *33rd Intern. Cosmic Ray Conf., Rio de Janeiro, Brazil, July 2013*, p. 579
142. Dagkesamanskii R D, Zheleznykh I M *JETP Lett.* **50** 259 (1989); *Pis'ma Zh. Eksp. Teor. Fiz.* **50** 233 (1989)
143. Gusev G A et al. *Phys. Usp.* **53** 915 (2010); *Usp. Fiz. Nauk* **180** 957 (2010)